2016

Detection of Fluid Density Anomalies Using Remote Imaging Techniques

Clara Smart
University of Rhode Island, csmart@my.uri.edu

DETECTION OF FLUID DENSITY ANOMALIES USING REMOTE IMAGING TECHNIQUES

BY

CLARA J. SMART

A DISSERTATION SUBMITTED IN PARTIAL FULFILLMENT OF THE REQUIREMENTS FOR THE DEGREE OF

DOCTOR OF PHILOSOPHY

IN

OCEAN ENGINEERING

UNIVERSITY OF RHODE ISLAND

2016

DOCTOR OF PHILOSOPHY DISSERTATION

OF

CLARA J. SMART

APPROVED:

Dissertation Committee:

Major Professor Chris Roman

Stephen Licht

Steven Carey

Nasser H. Zawia
DEAN OF THE GRADUATE SCHOOL

UNIVERSITY OF RHODE ISLAND

2016

ABSTRACT

Systematic and remote imaging techniques capable of detecting fluid density anomalies will allow for effective scientific sampling, improved geologic and biologic spatial understanding and analysis of temporal changes. This work presents algorithms for detection of anomalous fluids using an ROV-mounted high resolution imaging suite, specifically the structured light laser sensor and 1350kHz multibeam sonar system.

As the ROV-mounted structured light laser sensor passes over areas of active flow the turbulent nature of the density anomaly causes the project laser line, imaged at the seafloor, to blur and distort. Detection of this phenomena was initially presented in 2013 with significant limitations including false positive results for active venting. Advancements to the detection algorithm presented in this work include intensity normalization algorithms and the implementation of a support vector machine classification algorithm. Results showing clear differentiation between areas of plain seafloor, bacteria or biology, and active venting are presented for multiple hydrothermal vent fields.

Survey altitudes and the direction of travel impact laser data gathered over active vent sites. To determine the implications of these survey parameters, data collected over a single hydrothermal vent at three altitudes with four headings per altitude are analyzed. Changing survey geometry will impact the resolution and intensity of the laser line images, therefore, normalization and processing considerations are presented to maintain signal quality. The spatial distribution of the detected density anomaly will also be discussed as it is is impacted by survey range and vehicle heading.

While surveying hypersaline brine pools the observed acoustic responses from the 1350kHz high frequency multibeam sonar system indicate sensitivity to changes in acoustic impedance and therefore the density of a fluid. Internal density stratification was detected acoustically, appearing as multiple returns within a single water column image, and confirmed using a reel-mounted CTD. Additional acoustic returns correspond to rising bubbles, the surface of the brine pool, and the seafloor. This work allows for a systematic and complete reconstruction of the internal density structure of a brine pool.

Development of sensors and algorithms capable of efficiently gathering the data

necessary to establish a comprehensive understanding of the density variations within an area will improve the geologic understanding of a vent field or brine pool and allow for associations to be made between fluid flow and associated geological and biological activity.

ACKNOWLEDGMENTS

While my decision to pursue a Ph.D. in Ocean Engineering was not always clear, my goals around working with robotics and sensors for marine research have stayed true, in some format, since middle school. Collaborating with the scientific community, as an electrical engineer, provided the inspiration which led me to the University of Rhode Island. The research opportunities and collaborations I have participated in since 2011 have been challenging, varied and rewarding. I would like to acknowledge the key people who have made those opportunities possible and encouraged my success, both personally and professionally.

My decision to join Professor Chris Roman's lab, which focused on high resolution mapping, was based on the interdisciplinary nature of the work. Thank you Chris for believing and supporting me as a graduate student and as a researcher. The lab's focus on meaningful projects for specific scientists has allowed me to complete projects ranging from mosaicing the stern of the Titanic to detecting elusive fluid flow within vent fields. I also appreciate the encouragement I've received to pursue my own research ideas and discoveries, for example, detecting the destiny structure of a brine pool using the multibeam sonar system. One key thing I have learned from Chris: Cold seeps aren't cold.

As this is a dissertation, I would like to acknowledge my committee for their strong questions, support and insights into this research. Steve Carey has served as my science adviser since the beginning, outlining important geologic questions. Stephen Licht and Jason Dahl have provided incredibly valuable traditional engineering insight and have always pushed for high quality development. And thank you to my chair John King, who's breadth of knowledge allows him to ask tough questions.

The academic village which has surrounded me during this process is vast, ranging from my lab mates to scientists scattered across the world. Hanumant Singh of Woods Hole Oceanographic Institution, who was my adviser during the 2009 Summer Student Fellowship Program, was brainstorming graduate programs with me when he suddenly stated, in an unfiltered manner, 'Chris, Chris needs you!'. I'm not exactly sure what

the 'need' was, but Hanu was right in that I have been very happy in the lab run by his former student, and for that insight I am thankful. Within this lab I have met and worked with some of my best friends and what I hope will be life-long scientific partners. Gabby paved the way and acted our big sister, finding then showing us the ropes, developing key technology and algorithms for the lab and taking the brunt of the new lab pain. Ian and I shared an office for years and I am glad I had such a strong academic to bounce ideas off of and receive technical assistance from, oh - and share cat pictures with. Dave has masted the art of graduating and not leaving, and as a result has been a constant friend, engineering mind and lab problem solver. Regina has been a key source of personal support, a house mate and like minded citizen of the world. Although our research has not had strong intersections, she has become one of my best friends throughout this process. I have enjoyed working and laughing with members of our lab who have either passed though as masters students or have just started on their graduate school journey, including Kris (K2), Ben, Scott and Will.

Perhaps the greatest opportunity I received while in grad school was sailing aboard the E/V *Nautilus* as a scientific navigator and high resolution mapping specialist. This ship is the vision of Dr. Robert Ballard, who I have had the honor of working with and learning from. Because of his vision I have been able to acquire and analyze imaging data from hundreds of sites. The Ocean Exploration Trust team has encouraged my development as a leader at sea and I am amazed by the experiences, places and over nine months at sea I have been exposed to. A special thank you to those whom have made this happen, including; Katy, Nicole, Allison, Mike, Dwight, Ethan, Justin, Megan, Pavel and all those I have worked alongside at sea.

Through my research at URI , WHOI, and work with the Nautilus I have gained mentors and friends who have ensured and encouraged my success. Thank you for helping raise the next generation of oceanographic researchers. Key collaborations, mentorship and inspiration has been provided by Chris German, Dana Yoerger, Pete Girgus, Leigh Marsh, Anna Michel and Cindy van Dover.

While my academic family has been key to the success of this dissertation, my

family and friends have helped keep me happy, healthy and productive! My mother frankly didn't really know what to do with her robot loving daughter and encouraged her to find people who were capable of developing that passion. She has been my biggest supporter and my sounding board. My siblings, Will and Mad have always provided entertainment and help, Mads reading papers, Will helping me fix my car. To my aunt Kitty and her family, you have feed me every holiday season and rescued me from the hospital, I'm lucky to have you so close. Thank you to my friends for putting up with me during this process. Ann, being welcome at you and Matt's house has been a joy. Thank you to Stedmans Bikes and the Stedmans community for keeping me mentally stable, encouraging my competitive edge and keeping me on fast bikes! And thank you Mat for being amazing teammate and while you my have been at sea during my defense, your support, kind words, and humor over the last year has been amazing. And finally, I have to give an extra snuggle to Hazel, the little tortie kitty who somehow never deleted matlab scripts or substantial text while sleeping on my keyboard.

My acknowledgments are lengthy, yet they feel incomplete. I am so thankful for the friends, family and collaborators in my life who continue to support me on this journey.

PREFACE

This dissertation, *Detection of fluid density anomalies using remote imaging techniques*, is written in manuscript format and consists of three papers prepared for submission to peer reviewed journals. Each paper will be submitted to the respective journal by December 31, 2016.

The first manuscript *Advances in detection of diffuse seafloor venting using the structured light laser sensor* will be submitted to *Geochemisty, Geophysics and Geosystems* as it builds on the work presented in *Smart, 2013* which was also published in this journal.

The second manuscript, *Implications of range on detection of diffuse venting using the structured light laser sensor* address implications of survey parameters on the detection of hydrothermal venting. As this paper is presents an extension to the algorithm in Manuscript 1, it will be submitted alongside Maunscript 1 to *Geochemisty, Geophysics and Geosystems.*

The third manuscript, *Remote detection of density anomalies within Gulf of Mexico brine pools using a high resolution multibeam sonar system* presents a straightforward acoustic approach to acquiring information about the internal nature of brine pools. Due to the strong scientific component of this paper, it will be submitted to *Deep Sea Research I.*

TABLE OF CONTENTS

Page

LIST OF TABLES

LIST OF FIGURES

Figure **Page**

Figure **Page**

MANUSCRIPT 1

Advances in Detection of Diffuse Seafloor Venting Using the Structured Light Laser Sensor

by

Clara J. Smart [1], Chris N. Roman[2], Steven N. Carey [3]

In preparation for submission to Geochemistry, Geophysics, Geosystems (G^3)

[1]Ph.D. Candidate, Department of Ocean Engineering, The University of Rhode Island, Narragansett RI 02882. Email: csmart@my.uri.com

[2]Asst. Prof of Oceanography, Graduate School of Oceanography/Department of Ocean Engineering, The University of Rhode Island, Narragansett RI 02882. Email: cnr@gso.uri.edu

[3]Prof of Oceanography, Graduate School of Oceanography/Department of Ocean Engineering, The University of Rhode Island, Narragansett RI 02882. Email: scarey@gso.uri.edu

Abstract

Systematic and remote detection of diffuse hydrothermal venting using underwater robotic vehicles is complex and key to understanding the distribution, contribution, and context of diffuse hydrothermal seafloor venting. Diffuse flow is characterized by both low temperature and low flow rates and cannot be distinguished during a remote systematic survey using current visual, acoustic, or vehicle-mounted environmental sensors. The ROV-mounted structured light laser sensor, which images a projected laser line on the seafloor has shown sensitivity to fluid density anomalies during high resolution imaging surveys with preliminary results detailed in [1]. The presented work advances algorithms for detection of hydrothermal venting through the development of normalization routines and the implementation of a support vector machine (SVM) classification algorithm. Results from multiple vent field sites are presented and discussed.

1.1 Introduction

Diffuse hydrothermal venting is found within diverse environments making automated detection routines complex and inefficient. Low temperature and low flux fluid flow may be found alongside larger point source vents and surrounded by biological activity including bacteria, mussels, clams and tubeworms or it can be isolated, emerging from fissures in the seafloor. The presented approach systematically and efficiently detects diffuse hydrothermal seafloor venting while surveying varying environments using a structured light laser sensor mounted on a remotely operated vehicle (ROV). The goal of the resulting map is to systematically establish a spatial understanding of areas of bacteria and potential hydrothermal venting while assessing the structure and extent of a vent field. This tool will improve the geological understanding of the area, allow for better informed and efficient sampling or near bottom exploration and documentation efforts.

The remainder of the introduction will summarize the geologic motivations and current detection methodology. Section 2.1.2 will discuss the structured light laser sensor, including data acquisition and processing before the algorithmic advancements are

addressed in Section 1.3. Results will be presented and discussed in Sections 3.4 and 3.5.

1.1.1 Geologic Motivation

Low temperature diffuse hydrothermal flow is most likely to be found near low lying mounds and fissures it is effusive in nature and difficult to detect. Conversely, vigorous high temperature focused flow typically emanates from chimney-like structures and creates detectable buoyant plumes. In comparison to other types of venting, the large extent of diffuse flow may make it more influential by a factor of five with respect to the chemical and thermal processes of the entire ocean [2]. For instance, entire vent fields, such as specific sites at the Galapagos Spreading Center, are comprised of low flux diffuse flow [3]. This claim, however, cannot be verified without a systematic near bottom detection method.

Currently, there are approximately 300 known sites of hydrothermal activity worldwide, of which only 100 are comprised of vigorous point source venting [4]. However, due to detection difficulty it is likely that the majority of diffuse flow sites have not yet been located.

1.1.2 Review of Existing Vent Detection Methods

As observable temperature and chemical signals associated with diffuse venting decay rapidly due to mixing and are often no longer detectable just meters above the sea floor it is difficult to detect or map. As a result, current detection methods are inefficient, inconsistent and unable to complete systematic surveys over areas on the order of square kilometers in size. In most cases, diffuse vent sites are discovered as a secondary consideration following the localization and exploration of larger point source vents [5]. Additionally, detailed low altitude ROV or AUV surveys will typically identify areas of biological activity associated with venting, rather than the venting itself [6, 7]. For these reasons, the full extent and distribution of a diffuse vent field is rarely determined, and the entire process is likely to miss vent fields consisting only of diffuse flow sources [8].

Despite the difficult nature of the problem, some specific approaches to identify active venting have been developed using both visual and acoustic methods.

Point Source Vent Detection

The most successful vent detection schemes focus on large, high flux point source vents and require an AUV or ROV, fitted with various sensors to detect anomalies in magnetics, chemistry and temperature. Commonly, an initial survey is completed 50-400m above the seafloor searching for signals indicative of buoyant plumes while collecting bathymetric and water column data. This method favors the detection of high flux, vigorous point source vent systems as it requires the presence of buoyant plumes. Following the detection of a potential plume, lower altitude surveys with higher resolution are completed to distinguish the location of the vent source [5]. It is not until more detailed site specific dives are completed that imaging, flow and temperature analysis of the source vent and the surrounding area can be completed [6].

At known vent sites three-dimensional acoustic maps of active smokers have provided volumetric and flow analysis [9]. The Cabled Observatory Vent Imaging Sonar (COVIS) [10], a multibeam sonar and rotatory system installed at the Main Endeavor Field on the Juan de Fuca Ridge, computes 3-D plume maps by detecting backscatter due to suspended particulates and strong temperature gradients. Diffuse venting within close proximity may be detected through acoustic scintillation, allowing for only a broad understanding of its presence.

Diffuse Vent Detection

Traditionally, diffuse flow is detected visually by watching video feeds for "shimmering water" [11]. The shimmer, or mirage effect, is caused by the turbulent flow of fluids with an altered index of refraction caused by differences in water temperature, salinity and chemical composition [12]. Diffuse venting fluids are often clear with few particulates, therefore distortion caused by this mirage is the only visual marker. Unfortunately, this phenomena is only visible within tens of centimeters of the seafloor and is primarily detected *in situ* by the human eye while viewing the video, making this technique time consuming, inefficient and unsystematic. This is however, the most common way to determine areas to physically sample when investigating diffuse sites.

Experiments recreating this visual anomaly produce Schlieren-like flows which highlight the density fluctuations and can be controlled in lab settings. With sufficiently defined parameters a quantitative description of a particular flow and the index of refraction can be made [13, 14]. In natural situations additional factors, such as the presence of dissolved gases (eg. CO_2 or CH_4), turbulence due to bottom mixing and fluid composition will complicate any estimates.

Acoustic approaches for identifying and tracking diffuse flow have included detecting uncorrelated acoustic backscatter caused by temperature-dependent changes in acoustic impedance using a 330kHz Mesotech sonar system. This conical beam sonar was scanned parallel to the sea floor to intercept rising near bottom diffuse flow [15]. During data collection the sonar was positioned to minimize sea floor obstructions in the sonar's view and remained stationary. Additional acoustic detection approaches compute sound speed anomalies by comparing differentials in acoustic returns [16]. The stationary nature of these approaches does not allow for systematic surveying or ROV based exploration of large vent fields.

Initial Vent Detection with a Structured Light Sensor

During a 2010 high resolution bathymetric survey using a structured light laser sensor significant diffraction of the laser line was noted as it passed over active venting. This diffraction was further explored and image processing techniques were developed to detect this anomaly as a proxy for diffuse hydrothermal vent systems. Preliminary results, illustrating the feasibility of the method, which this paper will expand upon, were presented in 2013 [1]. Limitations to initial work included false indications of active venting in the presence of biology, sensitivity to seafloor bathymetry, and general robustness.

1.2 Structured Light Laser Sensor

Initially developed for sub-centimeter bathymetric mapping [17] the structured light laser system images a projected laser sheet as it is incident with the seafloor, showing the surface topography as if it were sliced along the laser plane. The vertical position of the

resulting laser line within each image can be converted to a bathymetric profile analogous to a single ping of range data from a multibeam sonar. The system, including the calibration process, is further detailed in [18] and is a basic variant of similar approaches [19–22].

1.2.1 High Resolution Mapping Suite

The structured light laser sensor is a component of the high resolution mapping suite mounted on the ROV *Hercules* (Figure 1.1) which also includes stereo cameras and a multibeam sonar and collects data for sub-centimeter resolution surveys [23]. The pair of stereo cameras are 12-bit 1360 x 1024 pixel Prosilica GC1380 computer vision cameras, one color and one mono, each with a 30° x 40° field of view in water. The structured light laser system consists of a second 12-bit mono Prosilica camera and a verged 100mW 532nm green sheet laser manufactured by Coherent Powerline are mounted to a rigid frame with known relative geometry. All imaging components are mounted in 6000m rated pressure housings. The 4000m rated multibeam sonar system designed by BlueView Technologies operates at 1350kHz at altitudes between 2-15m above the seafloor. Resulting data includes color and black and white stereo photos, bathymetric and intensity information from the multibeam and structured light laser, which also provides a metric indicative of active venting which is the focus of this study.

This imaging suite has been extensively used for high resolution mapping of geological, archaeological and biological sites [23]. All imaging data are collected simultaneously and co-registered.

Survey Methodology

During a high resolution imaging survey the vehicle is flown with a constant heading at velocities between 15 - 25cm/s and at a constant altitude between 2 - 4m above the seafloor. The laser line is imaged at approximately 20Hz, creating a survey resolution often better than one laser line per centimeter along track and 2-4 laser points (pixels) per centimeter across track. The range resolution is approximately 0.5cm per camera pixel. Strobe lit stereo images are acquired every 3 seconds, interlaced with the laser

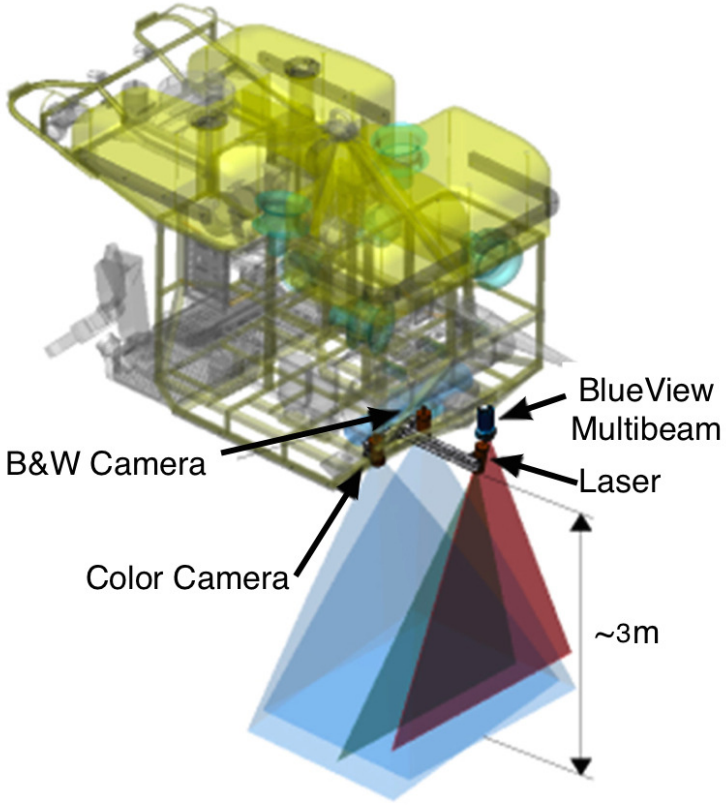

Figure 1.1: A computer rendering of ROV *Hercules* showing the standard imaging suite which includes a stereo camera pair, structured light laser and 1350kHz multibeam sonar. The sensor suite is mounted at the back of the vehicle away from operation lights. Strobes for stereo imaging are located forward of the cameras.

frames, while the multibeam operates continuously at 5-15Hz. A high resolution survey 30 x 30m in size can be completed in about 45min.

To improve the signal to noise ratio of the structured light laser and stereo images the sensors are mounted at the back of the vehicle, away from the ROV *Hercules's* forward operational lights. This 4000m depth rated ROV is closed loop controlled and capable of executing prescribed tracklines at a constant velocity and altitude or depth. The navigation sensor suite includes a 600kHz RDI Doppler Velocity Log (DVL), IXSEA OCTANS fiber-optic gyroscope and a Paroscientific depth sensor [24]. These data are collected using the DVLNAV software package [25].

1.2.2 Interaction with Density Anomalies

As the structured light laser sensor passes over active hydrothermal fluids the associated fluid anomaly causes the laser line to diffract and appear blurred instead of crisp within the captured mono image, Figure 1.2. The increased temperature, salinity and changing chemical composition of venting fluids alters the index of refraction causing diffraction. However, this relationship is only well understood for temperatures up to 30°C and salinity values up to 40PSU [12] and less well defined through interpolation of lab tests up to 500°C [26]. The turbulent nature of actively venting fluids creates an inhomogeneous medium with an index of refraction that varies both spatially and temporally. The result of turbulence as explained by [27] causes continuous angular deviation of the light rays increasing the scattering region (θ_s). The net result of scattering within this anomalous region is illustrated by the resulting blurred laser line and typically produces variations of 3-8 pixels in the width of the laser line.

To quantify this laser line spread, which serves as a proxy for active venting, the unitless intensity weighted second moment about the peak intensity value of the laser line, v^*, can be computed by

$$\sum_{i=v^*-\frac{w}{2}}^{v^*+\frac{w}{2}} r_i(v_i - v^*)^2, \tag{1.1}$$

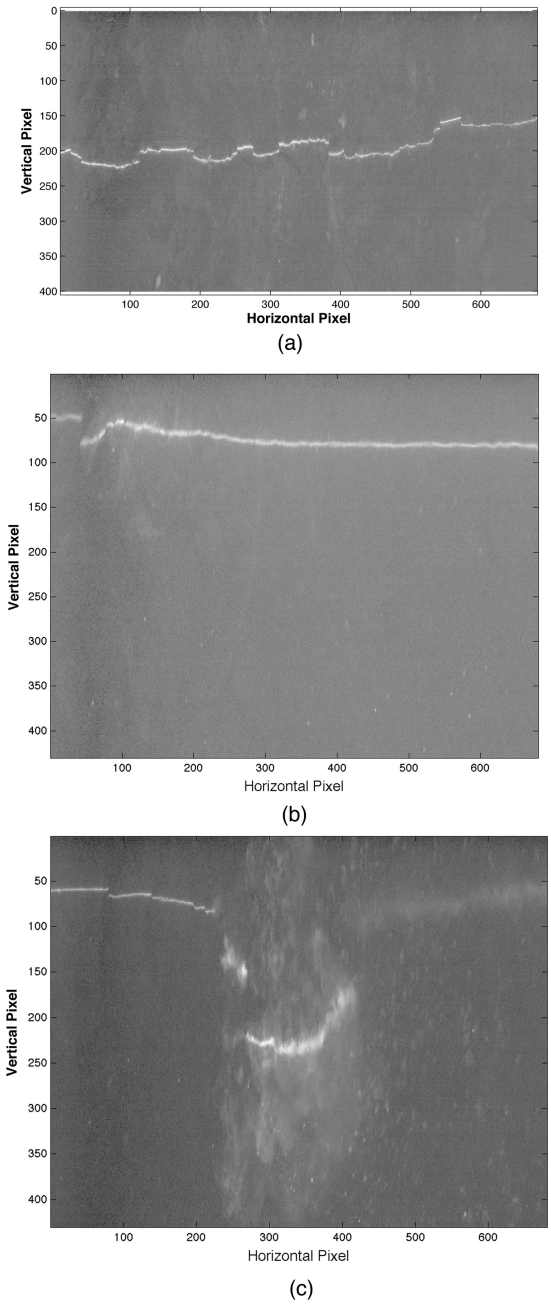

Figure 1.2: Examples of laser line captures, viewed on a log scale (a) A typical crisp laser line imaged over plain seafloor. (b) Slight blur appears to the left of the image as a density anomaly is imaged. (c) When passing over a high flux point source vent the laser line spreads due to refraction caused by the associated turbulence and optical anomaly.

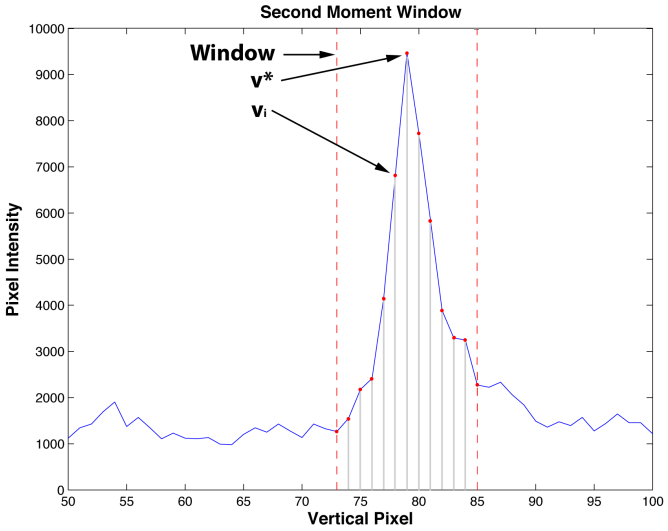

Figure 1.3: Cross section of the laser line annotated to define the variables considered for computation of the intensity weighted second moment about the centroid of the line, Equation 1.1.

where v_i and r_i are the comparison pixel location and intensity respectively and w is the size of the window about the laser line peak v^*. Figure 1.3 shows a cross section of the laser line identifying these parameters.

1.2.3 Acquisition and Processing

The image acquisition process (Section 1.2.1) and the subsequent detection and processing of the laser line is largely identical for both the presented vent detection methods and structured light bathymetric mapping [18]. The steps of the laser extraction batch processing algorithm which produces a complete set of profiles by determining the laser line peak v^*, which is used in Equation 1.1, are outlined below. Raw images are standard 12bit black and white photos of the laser line incident with the seafloor (Figure 1.4a).

1. A binary mask is created by thresholding the 12bit image of the laser line using Otsu's Method, which maximizes the variance between the 'foreground', in this case the laser line, and the 'background' the seafloor [28] (Figure 1.4b).

2. Each column within the image is then processed and viewed as an independent 1D

signal containing the cross-section of the laser line. Any cluster of pixels having intensity values greater than the previously determined threshold is a possible laser line cross-section.

3. If an image column contains multiple clusters of contiguous pixels above the threshold the candidate cluster locations and sizes are compared to neighboring columns and median laser line widths. The cluster with the most similar properties is selected as the laser line location within the column. Some image columns may contain no reasonable points above the threshold due to occlusions.

4. For each column, the pixel of maximum intensity within the selected cluster is chosen as the center of the line and denoted v^*. These pixels create the complete laser line profile across the image, analogous to a single ping of multibeam data (Figure 1.4c).

5. With v^* identified Equation 1.1 can be implemented to determine the laser line spread.

1.2.4 Creating Maps

Combining the extracted laser lines with the corresponding vehicle navigation allows for the assembly of high resolution bathymetric, intensity and vent detection maps. No additional acquisition steps are required while conducting the laser survey to create all three maps in post processing. The bathymetric data is derived from the location of v^*, as described above, with each laser line analogous to a ping of multibeam data. This range information is also applied to the normalization approaches addressed in the next section. Laser intensity (backscatter) maps rely on the intensity value of v^* which can be normalized. Assigning a weighted second moment value to each extracted point along the laser line shows a basic spatial distribution of laser spreading associated with active venting .

The structured light laser data can also be co-registered with stereo imagery, 2D mosaics and multibeam bathymetry. The precision of the co-registration is influenced

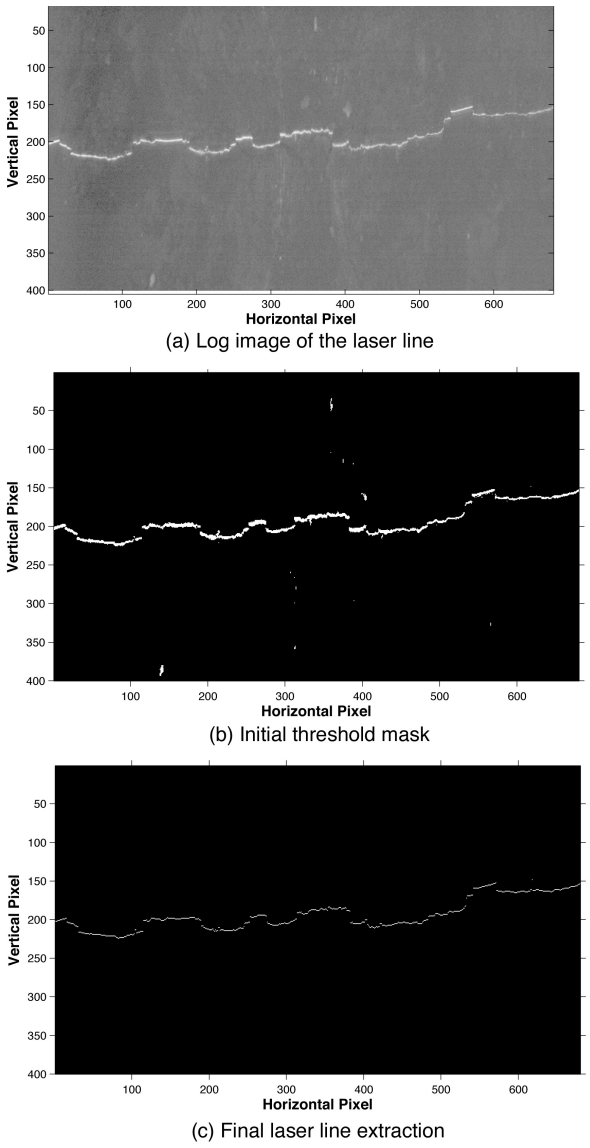

(a) Log image of the laser line

(b) Initial threshold mask

(c) Final laser line extraction

Figure 1.4: The laser extraction via image segmentation processes. (a) A raw image of the laser line over the sea floor (Shown in logarithmic scale for clarity). (b) Thresholded image highlighting the selected pixels. (c) The location of the laser line peak v^* within each image column.

by the accuracy of the laser calibration routine which is an active area of research.

1.3 Advancements to Laser Vent Detection

As mentioned in Section 3.1 the ability to detect active venting through identification of turbulent density anomalies was established in Smart 2013, [1]. This preliminary work relied on the intensity weighted second moment as defined in Section 1.2.3 by Equation 2.1. While the structured light laser sensor showed sensitivity to anomalous fluid density, false positives, high second moment values associated with increased laser line intensity or width as well as bathymetric biases were also observed. The notable errors occurred as the laser passed over reflective seafloor features including bacteria, shells, tubeworms and man made objects. For instance, Figure 1.5 shows a mosaic and the corresponding vent detection map of a cold seep site near Kick'em Jenny Volcano, Grenada. Following an extensive search for actively venting fluids using the HD camera system no diffuse flow was found rising above the bacterial mats. However, areas of thick white bacteria are highlighted as having high vent potential. Furthermore, while imaging the laser line on a slope the changing distance between the camera and seafloor causes the laser line to appear brighter and wider closer to the camera, and dimmer when farther away due to attenuation.

To correct for these shortfalls of the previous detection method, three types of normalization are implemented (Section 1.3.1) and a machine learning approach will be taken to differentiate seafloor characteristics (Section 1.3.2).

1.3.1 Normalization

Intensity values dominate the the weighted second moment computation, therefore normalization of laser line intensity values prior to this computation is important for accurately detecting venting fluid.

Exposure Compensation

During the acquisition process the camera exposure settings are manually adjusted such that the laser line appears crisp and bright while the background is predominantly

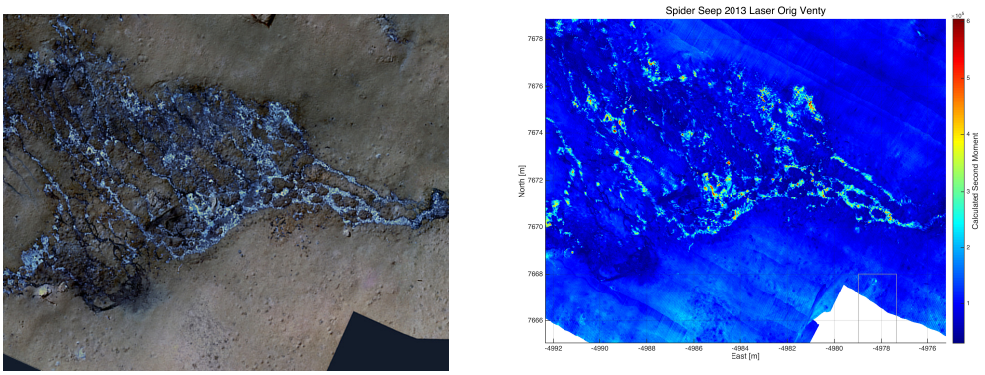

(a) (b)

Figure 1.5: An subset of the extensive spider like seep site discovered on the flanks of the Kick'em Jenny Volcano, Grenada. a) The color photomosaic of the area showing the biological structure. b) During exploration with the ROV no active venting was observed, yet areas of venting are suggested by the previous vent detection method. These false positives occurred in the presence of bright or thick bacteria which returned high second moment values due to increased laser line caused by high intensity and internal refraction.

black. While these settings counter vehicle lighting, survey parameters and environmental characteristics they prevents direct comparison between data from multiple surveys. An example of laser lines collected at two different survey sites are shown on the same intensity scales in Figure 1.6 with their corresponding intensity histograms. The left image is from a 2011 survey while the right, which is significantly brighter, was collected in 2014 illustrate the need for exposure compensation.

Adjusting the intensity range for each survey to an established baseline will allow for comparison between surveys. Without additional lighting the collected images are dark except for the illuminated laser line, the signal of interest, resulting in a very high signal to noise ratio which is bolstered by the cameras 12bit dynamic range. As areas of dark seafloor do not contain data relevant to laser processing normalization reducing the image intensity such that the non-laser line components are as close to black as possible will not impact then laser line threshold and extraction processes. The laser line makes up less than 1% of the image, therefore, the mean intensity of an image is a good representation of the background intensity. Subtracting this average value from the collected intensity data establishes an intensity baseline for all collected images. The need for this adjustment is apparent in the pixel intensity histograms of Figure 1.6. As

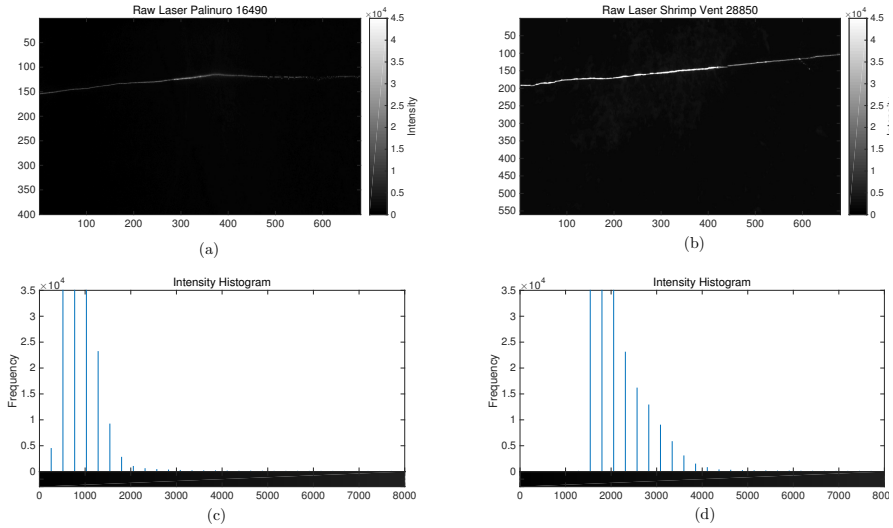

Figure 1.6: The exposure settings for the laser line captures are set manually and not typically constant between any two surveys. Captures from two surveys are shown on the same intensity scale with their respective image intensity histograms. The left image was collected in 2011 and is darker than the right image collected in 2014.

lighting conditions can change over the course of a survey the average image intensity is computed for 30-50 temporally spaced laser line captures. The mean of these average intensity values determines the exposure normalization value for the entire survey. Prior to laser line extraction the intensity values of all survey images are shifted by this baseline. This allows for surveys to be analyzed by the same classification routine regardless of site, acquisition date and exposure settings.

Accounting for Range

Local bathymetry varies within a survey and affects the distance between the camera and seafloor impacting the brigthness of the laser line. While range differences between a camera and imaged laser line on the order of a meter would be considered trivial in air, attenuation of water has a significant impact [27]. Figure 1.7(a) shows a laser line imaged across a plain seafloor slope with a 1m change in elevation. The left side of the laser is approximately 2m from the camera while the right side is nearly 3m away. The corresponding intensity values and intensity weighted second moment values are shown on the same horizontal scale and illustrate a noticeably brighter and wider laser line when the seafloor is closer to the camera. This difference can falsely indicate a change in

seafloor characteristics and increase the second moment calculation enough to indicate active venting.

Using triangulation and an accurate laser calibration it is possible to transform the v^* laser line coordinate into the vehicle reference frame and determine the distance between the laser line location on the seafloor and the camera. Taking an approach similar to that used in LiDAR surveys the intensity value of each laser line point, I_{actual}, is multiplied by the ratio between the recorded range, R_{actual}, and ideal range, $R_{expected}$, to determine a normalized intensity value, I_{norm} [29].

$$I_{norm} = I_{actual} * \frac{R_{actual}}{R_{expected}} \tag{1.2}$$

Range normalized intensity and second moment values shown in Figure 1.7(b), are no longer range dependent and are more uniform over plain seafloor. Resulting changes in laser line intensity should be indicative of changes in seafloor characteristics and not bathymetry.

Non-uniformity of the Laser Line

Non-uniformity in the brightness along the laser line will also impact laser line characteristics. For example, due to the line generating optical element, the left side of the laser tends to have higher intensity values than the right. Such variations are typical of all laser lines.

The correction approach resembles algorithms for removing lighting artifacts from any images taken with external light sources. Following exposure and range normalization the along track mean intensity of all extracted laser lines is computed. Distinct variations in reflectivity are averaged away as most surveys consist of thousands of images, leaving only the consistent illumination pattern. Dividing each normalized extracted laser line by the resulting illumination pattern allows for uniform across track illumination.

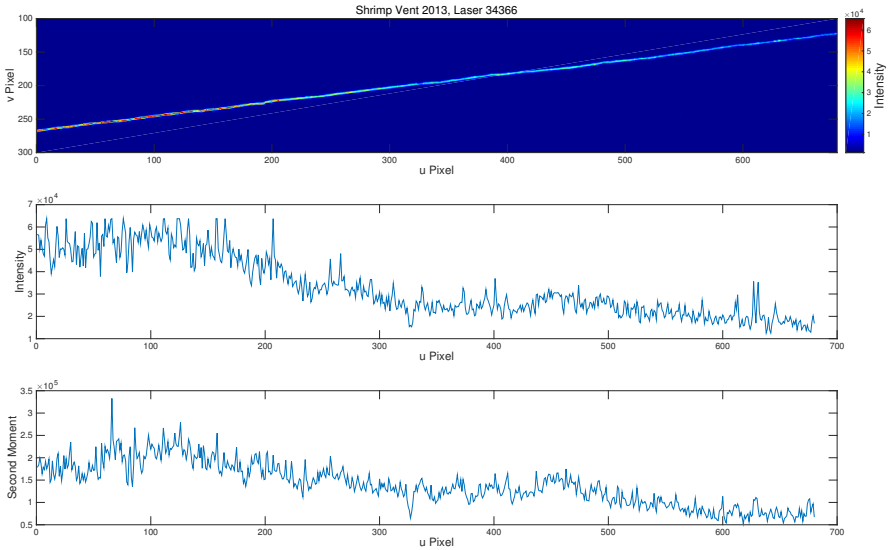

(a)

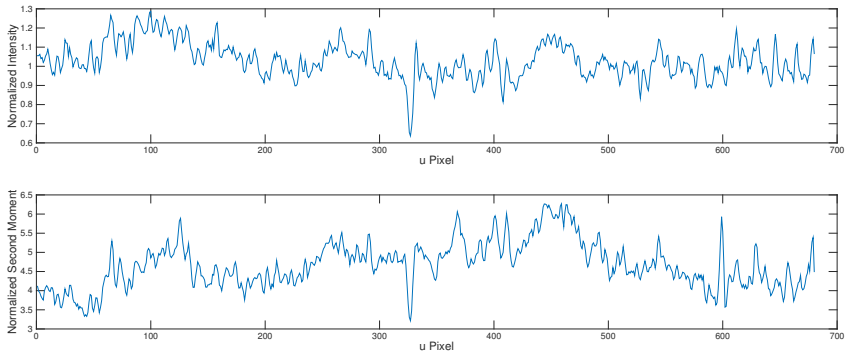

(b)

Figure 1.7: Illustrating the need to account for range, a single laser line imaged while on a slope of plain seafloor where the depth differential across the laser line is approximately 1m. (a) The left of the laser line is closer to the camera and therefore the intensity and spread of the laser line is greater, which translates to increased second moment values, that distort vent detection processes. (b) Following range normalization the resulting intensity and second moment values are more uniform without a bias due to range.

The final intensity values which are associated with sea floor characteristics and biological activity and passed to the weighted second moment computation are not influenced by changes to exposure, seafloor bathymetry or inconsistent lighting patterns.

An example of the results of intensity normalization are shown in Figure 1.8. The presented data was collected on a hillside on the Mid-Cayman rise, Figure 1.8(a). Without normalization, the second moment computation is affected by changes in range and laser line non-uniformity, as indicated by the across track artifacts, Figure 1.8(b). Following normalization these artifacts are either nonexistent or have been significantly reduced, Figure 1.8(c). Reduction, not necessarily elimination, of such artifacts is essential before passing a data set through a classification algrothim. Additionally, the outlined intensity normalization procedures scale results such that multiple surveys can be compared.

1.3.2 Support Vector Machine Implementation

Given the image coordinates and intensity values for each laser line pixel, it is possible to implement a robust multi-class support vector classification process to differentiate between plain seafloor, bacteria or other biological activity and active hydrothermal venting.

A support vector machine (SVM) is a supervised learning method for classification. Labeled training data, support vectors, are used to determine a hyper-plane dividing two classes while also maximizing a margin, the distance between the hyper-plane and data points [30]. This non-probabilistic linear classifier is typically applied to binary data, however, the three class structure desired by this problem can be decomposed into multiple "one-vs-all" binary class problems. The output binary classification function with the highest score then determines the class. For instance, a pixel showing *plain seafloor* will receive a high score from the 'seafloor vs not seafloor' classifier and low scores from 'biology vs not biology' and 'venting vs not venting' classifiers resulting in a *seafloor* class label. A trained support vector machine will provide boundaries for automatic classification of between seafloor, biology and venting based on input feature

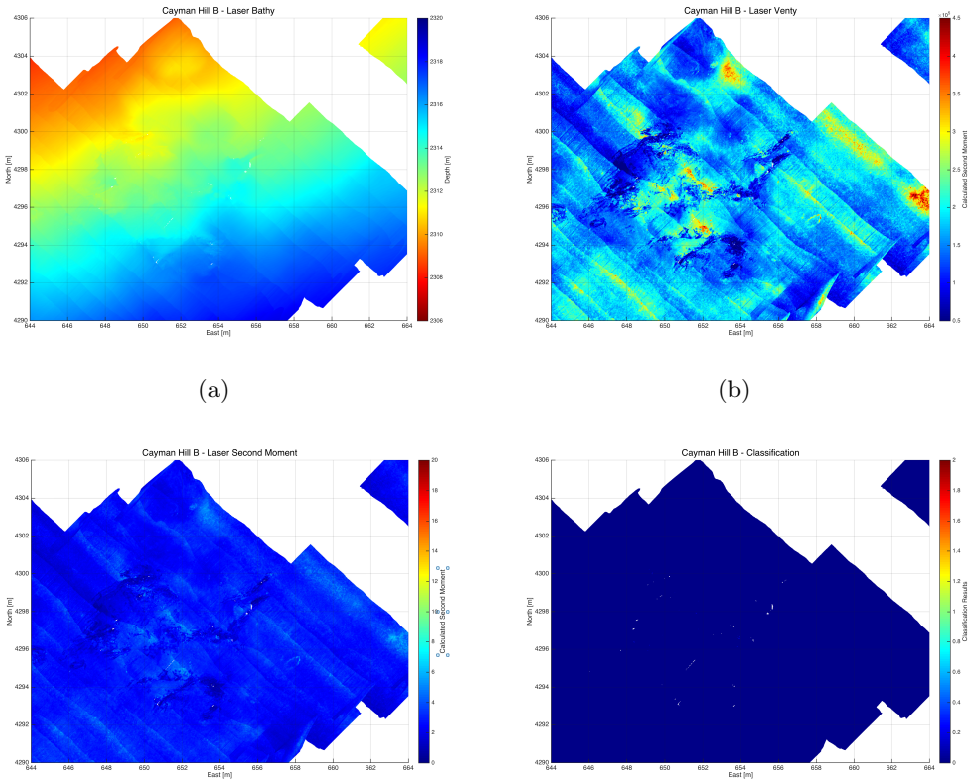

(a) (b)

(c) (d)

Figure 1.8: A section of a survey completed on a hillside at the Mid Cayman Rise shows the benefits of implementing normalization and classification routines. (a) The laser bathymetric map showing a 10m change in depth over the 15m x 15m area. (b) The initial vent detection method relying only on the second moment computation. Changes in second moment values due to range and laser uniformity are visible, which can create false positives when considering the pretense of active venting. (c) The laser second moment computation following the implementation of the normalization routines. While some artifacts are slightly apparent, the magnitude of these artifacts is significantly lower. (d) Following the SVM classification routine the entire area is classified as plain seafloor, which is accurate.

vectors corresponding to metrics associated with the intensity and spread of the laser line.

Training data for this classification routine were hand selected and classified from three different data sets. The first data set was collected in 2015 at the Iguanas Vent Field in the Galapagos, Ecuador and contains three distinct areas of focused flow within vent structures, diffuse flow, and bacteria biological activity in an area of pillow basalt. Approximately 1500 points were selected by hand and classified as either venting, bacteria or seafloor. Classification of traning data was based on the second moment computation in conjunction with the intensity values and included selecting specific pixels. High definition video, stereo imagery and cruise data was used to verify these classifications. The second data set, collected at a cold seep near Kick'em Jenny Volcano, Lesser Antilles, shows an intricate spider web-like pattern of bacteria and biological activity, Figure 1.5. As no active venting was discovered at site, the selected 2200 points consisted of bacteria and seafloor. The bacteria at this site varied in color and uniformity, resulting in a range of intensity values. The third data set from which training data were selected was a survey completed in 2013 at the Mid-Cayman rise. This data set was collected at an altitude of 2.5m on a rocky slope with a single active vent. Bacteria is not present at this location, the only observed biology were tiny shrimp at the vent orifice. This comprised the smallest training set with 540 points. In total, the complete training set consisted of 4340 points with 1930 labeled as seafloor, 1773 representing bacteria and 637 labeled venting. Values have been assigned to each class with *0* representing plain seafloor, *1* corresponding to biology and *2* venting. Further discussion of the training data is presented in Section 1.5.3. Visual representation of the classification data will also utilize this numbering system.

Training feature vectors containing metrics associated with the normalized intensity and spread of the laser line resulted in the development of a successful SVM. Somewhat unsurprisingly, the features corresponding to the most successful SVM were laser line intensity of v^*, and the intensity weighted second moment. The resulting classifier is shown in Figure 1.9(a) with three distinct regions designating plain seafloor (red), bac-

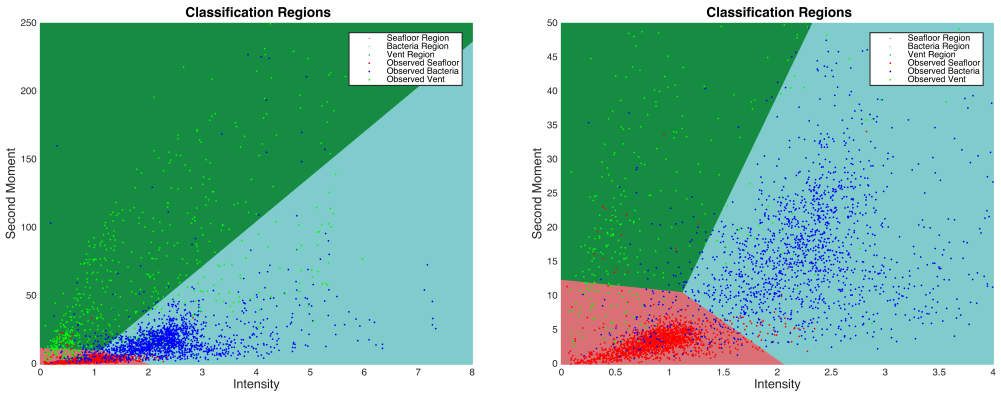

(a) (b)

Figure 1.9: Results from the support vector machine classification process based on the laser intensity values and the computed second moment. A point will be classified as seafloor (red area) if both intensity and second moment values are low, bacteria (blue area) if the intensity dominates and venting (green area) if second moment result is high. The classification training data is plotted as overlay points by color. (a) Depicts the SVM result for the entire classification space. (c) Focuses on the transition between the three regions.

teria (blue) and venting (green). Training data points are shown in correlating colors. The distribution of this classifier is logical as plain seafloor should have the lowest intensity and minimal laser line spread. The transition between bacteria and venting reflects the idea that not all light refracted by venting is returned to the camera and therefore this class has a lower overall intensity.

Laser lines collected during a survey over an area with hydrothermal venting can be processed and passed through the SVM classifier, Figure 1.13(a). The results can then be presented as waterfall of laser lines or be constrained by navigation and gridded to create a geospatial map.

SVM Metrics

Following the development of the SVM classification algorithm, metrics determining how well the training data fit the resulting model were computed. It is not possible to set decision boundaries with complete classification accuracy. A summary of these metrics are presented in Table 1.1. Data is presented for both the complete data set and for data from each site. The presented metrics and influence of training set data will be further discussed in Section 1.5.3.

	Total	Seafloor	Bacteria	Venting
Full Training Data Set				
Data Points	4340	1930	1773	637
Correctly Classified	89.8%	96.2%	87.9%	76.0%
Spider Seep				
Data Points	2303	1240	1063	0
Correctly Classified	96.0%	99.8%	91.4%	0
Cayman Vent				
Data Points	541	323	0	218
Correctly Classified	81.7%	87.3 %		73.4%
Iguanas Vent				
Data Points	1496	367	710	419
Correctly Classified	83.4%	91.8%	82.5%	77.3%

Table 1.1: Overivew of Support Vector Machine classification metrics.

1.3.3 Spatial and Temporal Averaging to Reduce Noise

The previously described classification process independently analyzes each pixel of the laser line, which captures less than 0.5cm^2 of seafloor. Classification at this resolution leads to spurious noise which decreases signal strength and the detection capability. In an effort to improve classification the intensity results were blurred both spatially, averaging adjacent pixels of the same laser line (across track), and temporally, considering data from the previous and subsequent laser lines (along track). The intensity weighted second moment is then computed using these values and passed through the SVM classifier. The impact of spatial and temporal averaging is shown in Figure 1.10. Spurious noise is visible and can likely be attributed to hydrothermal particulates in the water, Figure 1.10(a). Without noise reduction this raw image can provide insight into effusion of venting fluids, however, the resulting classification is cluttered, Figure 1.10(c). In comparison, the spatial and temporally averaged intensity and venting images in Figures 1.10(d) and 1.10(e) lead to the classification image Figure 1.10(f) which shows a distinct vent source.

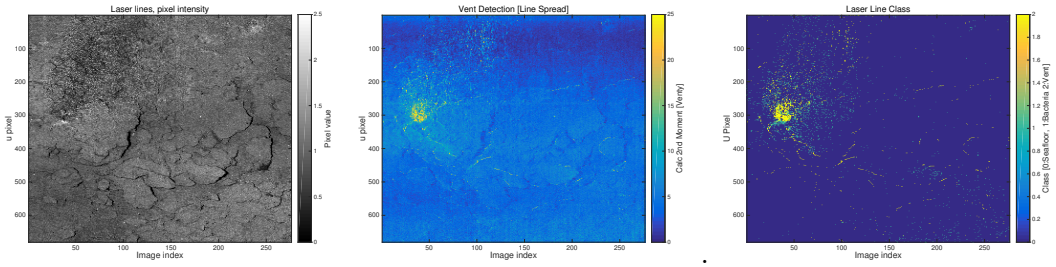

(a) Original Intensity (b) Original 2nd Moment (c) Original Classification

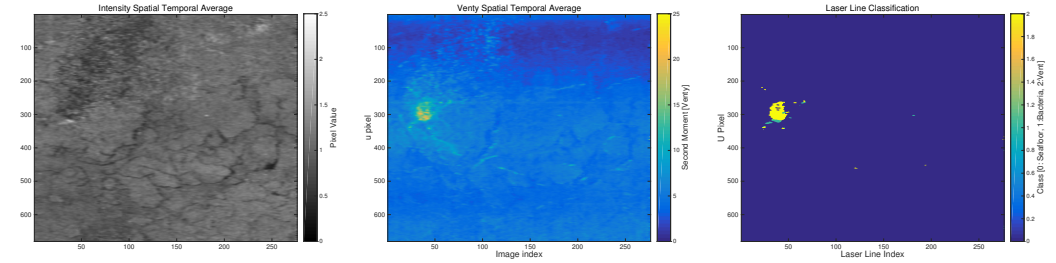

(d) Averaged Intensity (e) Averaged 2nd Moment (f) Averaged Classification

Figure 1.10: Spurious noise in the classification routine is reduced by spatially and temporally averaging the intensity and second moment results. (a -c) Represent the classification processes over an active vent without averaging where (a) show laser line intensity, (b) is the results of the second moment computation and (c) is the resulting classification. (d-f) Show spatially and temporally averaged intensity in (d), second moment computations (e) and classification (f), resulting in a more distinct area of active venting and fewer single points.

1.4 Results

Detection of diffuse hydrothermal venting at sites visited between 2010-2015 will highlight the diffuse seafloor venting algorithm advancements previously discussed. All data was collected by the high resolution imaging suite described in Section 1.2.1 which was mounted on *ROV Hercules* operated from *E/V Nautilus* (Ocean Exploration Trust). A brief overview of each study site will be provided before presenting the classification results, associated video observations, and sampling efforts.

1.4.1 Kick'em Jenny Diffuse Flow, an SVM classification example

High definition video footage, imaging data and temperature samples were collected in 2014 at a small hydrothermal vent site within the Kick'em Jenny Volcano crater near Grenada in the Lesser Antilles. The seafloor consists of flocculant rust-colored sediment, small mounds and structures including extinct iron oxide chimneys, areas of white bacterial mats, and small areas of diffuse flow [31]. Figure 1.11 shows HD captures of a vent orifice where isolated focused flow was detected and sampled. Bacteria is present around the edge of the vent orifice and the shimmer associated with active fluid flow is visible around the temperature probe in Figure 1.11(b). The color image shown in Figure 1.12(a) was captured by the imaging suite and shows no indication of active venting, illustrating the difficulty in locating diffuse seafloor flow remotely. A section of laser bathymetry is shown in Figure 1.12(b).

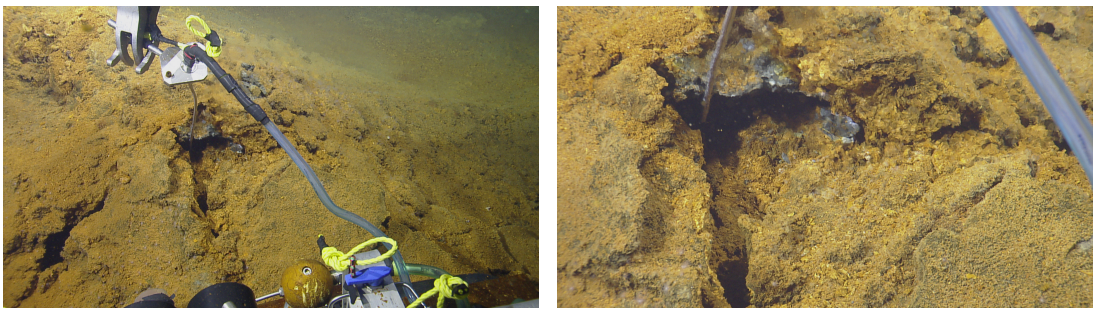

(a) (b)

Figure 1.11: Images of the small vent site within the Kick'em Jenny Crater taken while sampling fluid and temperature. The images were collected in 2014 using the high definition video camera on ROV *Hercules*.

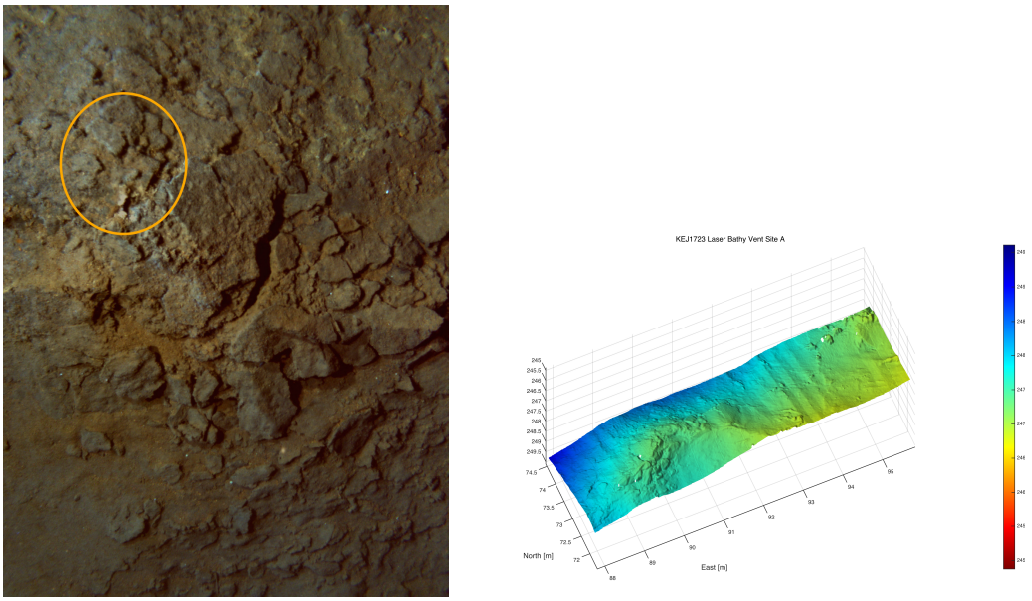

(a) (b)

Figure 1.12: Overview of the Kick'em Jenny 2014 diffuse flow site. a) Color photo taken at 3m of the area of active venting (circled). b) Laser bathymetry of the area of active venting.

A waterfall of a subset of the collected structured light data (276 laser line images each 680 pixels wide) is shown in Figure 1.10. Before each pixel is passed through the SVM classification routine these data are normalized and averaged. The classification space is displayed in Figure 1.13(a), note the dominance of red seafloor points, a fair number of green points representing venting and very few points classified as bacteria in blue. The resulting classification map is shown in Figure 1.13(b), where blue (labeled 1) is seafloor, green (labeled 2) is bacteria and venting is yellow (labeled 3). This result is consistent with the observed focused flow emanating from the vent orifice.

When this subset of data is placed in the context of the survey and gridded the area of venting is still distinctive (Figure 1.14). The range of intensity within the area is limited, which is expected as the seafloor is fairly uniform flocculant orange sediment (Figure 1.14(a)). The intensity weighted second moment, which previously served as a proxy for active venting indicates spreading of the laser line at the vent orifice located at the top right of Figure 1.14(b).

This survey was gridded to one centimeter which required down sampling and aver-

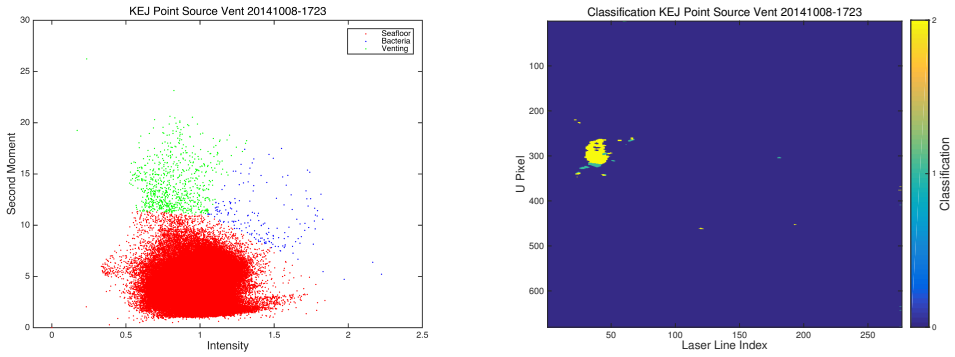

(a) (b)

Figure 1.13: Laser and SVM classification results from Kick'em Jenny 2014 diffuse vent site. a) The SVM classification space for the site. b) Resulting classification map of the vent site with 0 corresponding to seafloor, 1 is bacteria and 2 is venting.

aging the data. Laser data is collected with a density of 3-5 pixels per centimeter across track and 1-2 pixels per centimeter along track. As a result, the classification values have been averaged and range between 0-2, the result is shown in Figure 1.14(c). This effectively provides a confidence level of a detected class based on surrounding pixels. For example, within the averaged classification image the center of the vent orifice is red (strongly classified as venting) while the outer edge transitions to orange, indicating a decrease spatially in the detection of the venting. However, if only distinct class values are desired the gridded data is rounded and the resulting downsampled class data is shown in Figure 1.14(d) where blue (*0*) corresponds to seafloor, green (*1*) represents areas of bacteria and venting is colored yellow (*2*). The large area of bacteria in the center of the figure has been confirmed and represents a dark, reflective bacteria found within the sediment along the north side of the slope.

These detection results align with the observations and sampling during efforts conducted during the ROV dive. The temperature probe recorded an ambient temperature of 13.6°C, a temperature of 21.1°C within the vent orifice and 19°C above the seafloor within the flow. The secondary vent site, located approximately 7m to the south east consists of diffuse flow emanating from cracks within the seafloor. Temperature probe readings were also taken at this site and recorded as 14.1°C ambient 86.4°C within the

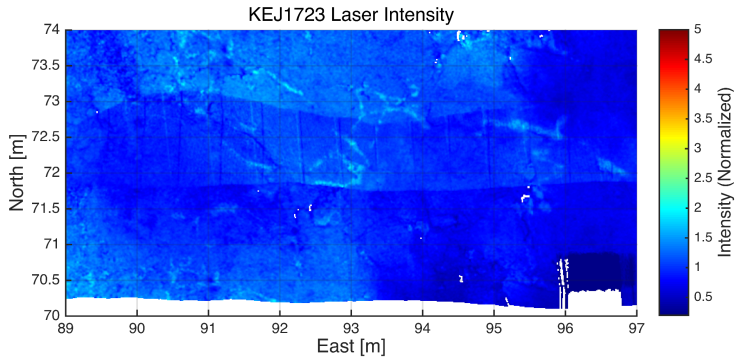

(a) Laser Intensity

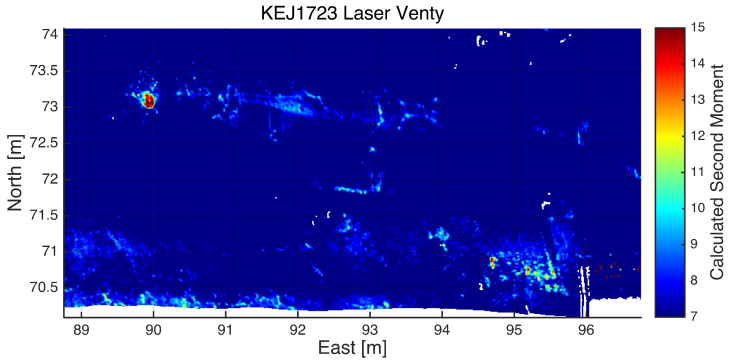

(b) Second Moment Computation

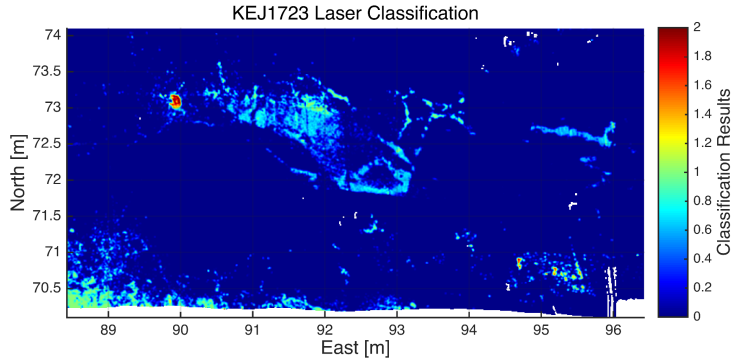

(c) SVM Classification

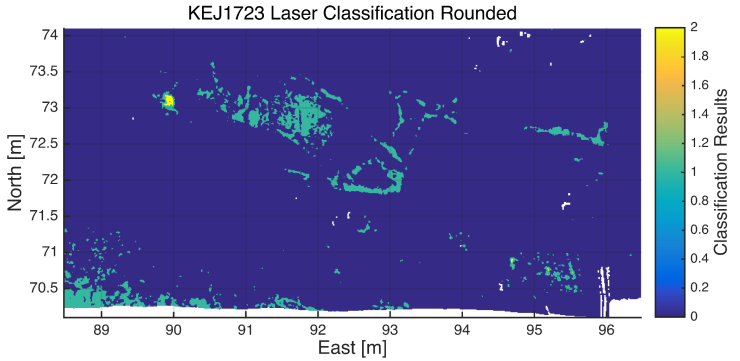

(d) Rounded SVM Classification

Figure 1.14: A survey subset showing the areas of active venting. (a) Normalized intensity over the site, which is mostly seafloor with areas of bacteria. (b) The second moment computation shows areas of likely venting. (c) Gridded SVM classification result based on intensity and second moment data (seafloor = 0, bacteria = 1, venting = 2). (d) Gridded classification data rounded to one of the three classification labels.

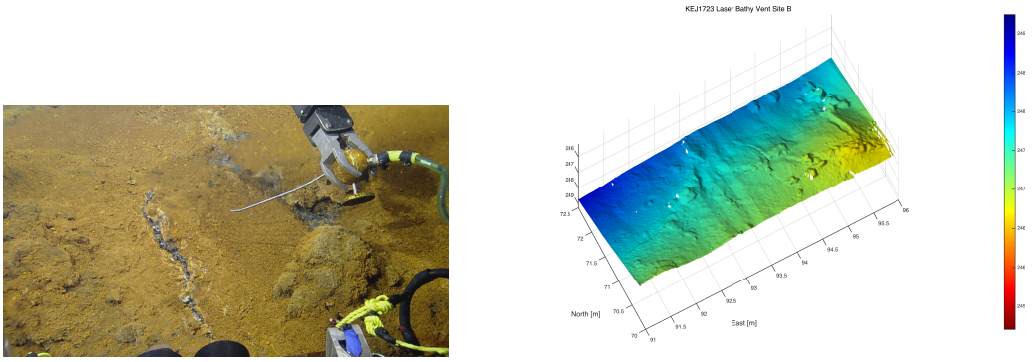

(a) (b)

Figure 1.15: Overview of the second site of observed venting at Kick'em Jenny. (a) HD capture of the second site of active flow during temperature measurements, shimmer indicative of density anomaly associated with active venting is apparent in the center of the frame. (b) Laser bathy at second vent site

fissure and 22°C in the diffuse flow.

1.4.2 Palinuro

Active hydrothermal venting sustains tube worm-dominated biological communities at Palinuro Seamount, Tyrrhenian Sea, Italy. This site was mapped in 2011 and was a focus of the initial laser vent detection study published in 2013 [1]. However, additional venting has been confirmed using the SVM method and areas of flow have been differentiated from areas of dense biological activity.

The primary vent site, and the location of a tubeworm colony is shown in the capture from *Hercules's* HD camera, Figure 1.16(a), and the photomosaic, Figure 1.16(b). This area is relatively flat with two rocky mounds colonized by tubeworms and surrounded by bacteria. Imagery obtained using the high definition video camera observed vigorous flow within both colonies where temperature probe data was collected. Venting at the northern feature had a maximum temperature of 60.4°C while the southern mound of active venting had a maximum temperature of 71.1°C, ambient was 13.5°C.

Highly reflective soft bacteria causes the laser line to appear brighter and bloom due to internal scattering. This effect causes a blurred laser line to be falsely labeled as active venting, not bacteria. An example of this is evident when comparing Figures 1.17(b) and 1.17(a), where it is apparent the high intensity bacteria within the southern

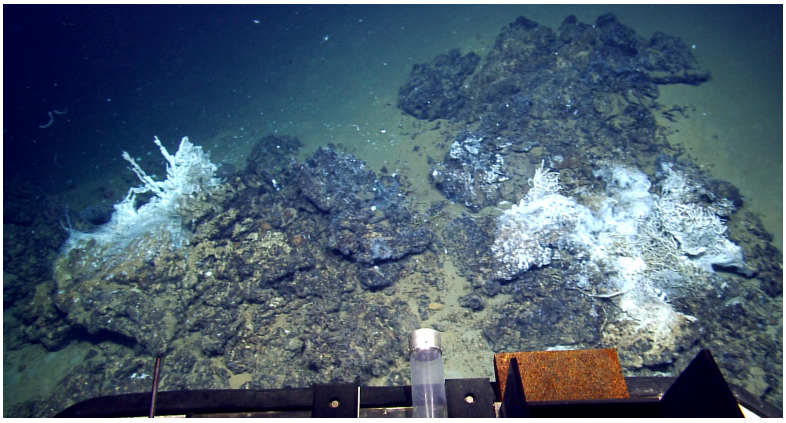

(a)

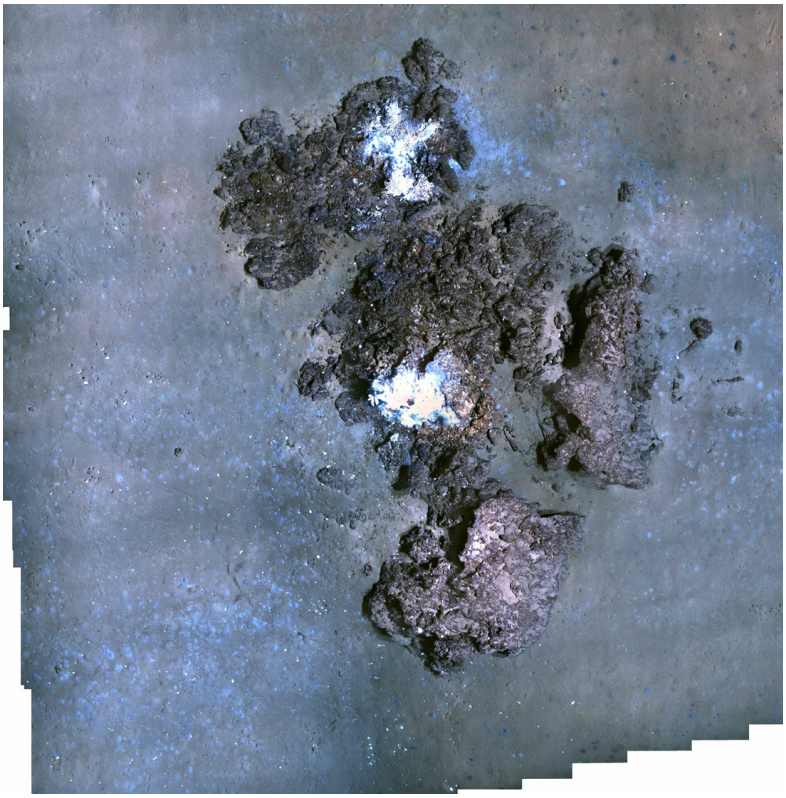

(b)

Figure 1.16: Overview of the Palinuro vent sites. (a) HD capture of the two main areas of active venting within tube worm colonies living on rocky substrate. (b) 2D photomosaic of the area.

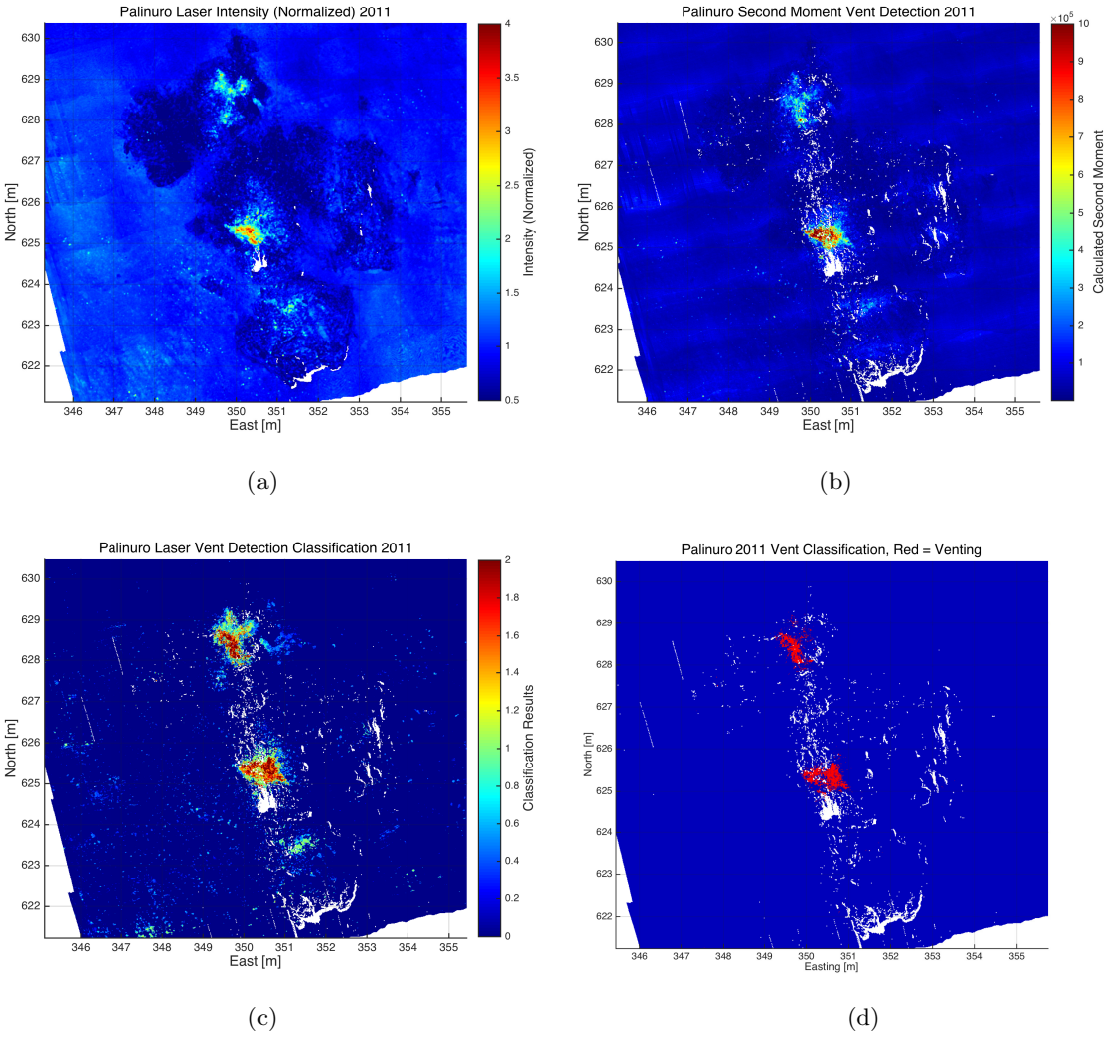

Figure 1.17: Comparison between detection results at the Palinuro Vent Site. (a) Shows a normalized laser intensity map of the area. (b) Shows the vent detection results using the previous algorithm which determined venting based an un-normalized second moment computation. This image is very similar to the normalized intensity image and distinctly identifies venting at only one of the tube worm colonies. (c) Vent detection using the normalized SVM approach. This data is gridded and classification values are averaged between 0-2, where 0 is seafloor, 1 is bacteria and 2 is venting. Distinct areas of active venting appear, correctly, at both tubeworm colonies. (d) Shows the same data as (c) however, only areas indicating active venting are shown in red.

colony dominates the vent detection algorithm. The SVM classification routine independently considers the intensity value and computed second moment values. This allows for differentiation between the increased intensity values associated with bacteria and tube worms, and the effects of fluid anomalies on the laser line. The gridded SVM result for this site is displayed in Figure 1.17(c), which indicates distinct fluid activity on both mounds surrounded by bacteria. Only the venting class is shown in Figure 1.17(d) revealing two distinct areas of fluid flow which correlate with the results from visual survey. The result suggests the SVM classification technique is robust to seafloor characteristics and is able to isolate diffuse flow independent of biological activity. Additionally, this example illustrates the improved sensitivity of the algorithm.

1.4.3 Shrimp Vent

Shrimp Vent is one one of the most dominant areas of venting within the active Kick'em Jenny crater, Grenada which *E/V Nautilus* visited in 2013 and 2014. Areas of diffuse fluid flow, and bubbling seeps, are situated on a steep hill alongside large areas of bacteria and shrimp, Figure 1.18. Multiple areas of active venting were located, imaged and sampled including the presented data which was collected in 2013.

A 90m^2 subset of full Kick'em Jenny crater survey containing the majority of the active Shirmp Vent area is presented in Figure 1.19. This area is along the south western edge of the crater and has a nearly 10m bathymetric differential along the 15m north-south survey extent. The two dimensional photo mosaic, Figure 1.19(a), illustrates the seafloor characteristics including the extensive bacterial mat coverage. Implementation of the original vent detection method at a site with these bathymetric and seafloor characteristics would return mostly false positives making precise detection of active venting difficult.

However, bathymetric bias is not apparent after implementing the previously discussed range and exposure normalization algorithms and bacteria is differentiated from active venting by the SVM classification algorithm. Gridded classification results shown in Figure 1.19(b) once again indicate areas of bacteria alongside multiple small areas

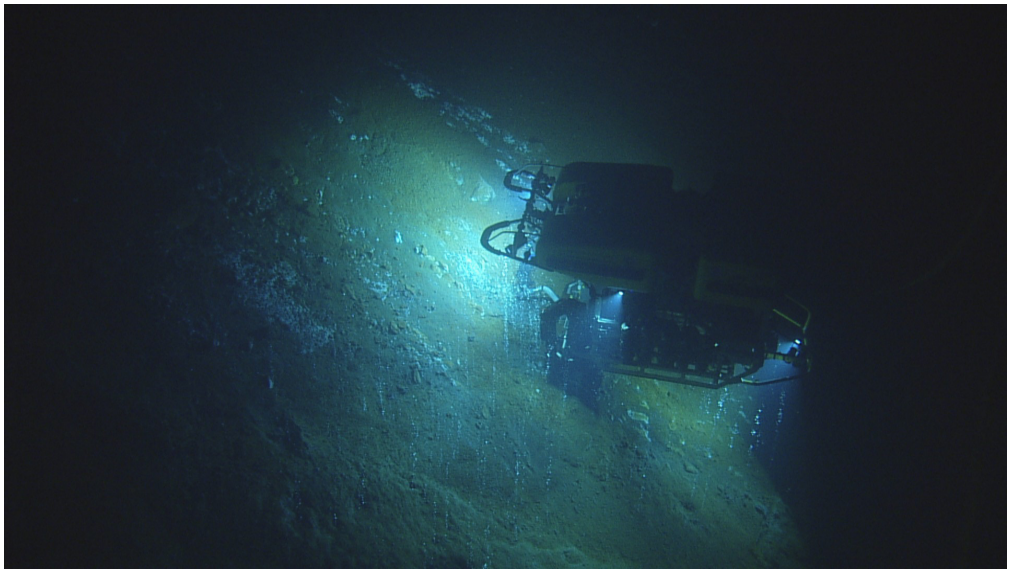

(a)

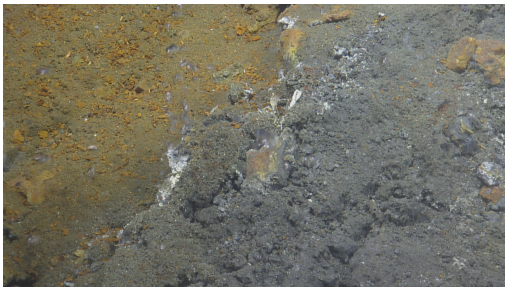

(b)

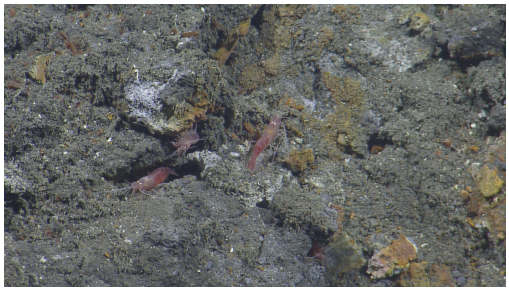

(c)

Figure 1.18: Captures providing an overview of Shrimp Vent including bathymetric and biologic activity. (a) HD capture from ROV *Argus* showing *Hercules* working at the shrimp vent site alongside the south west side of the crater. Boulders and bacterial mats can be aligned with the photomosaic. (b) Active venting and bacteria at Shrimp Vent. (c) Shrimp living under rocks and within cracks near the vent fluids.

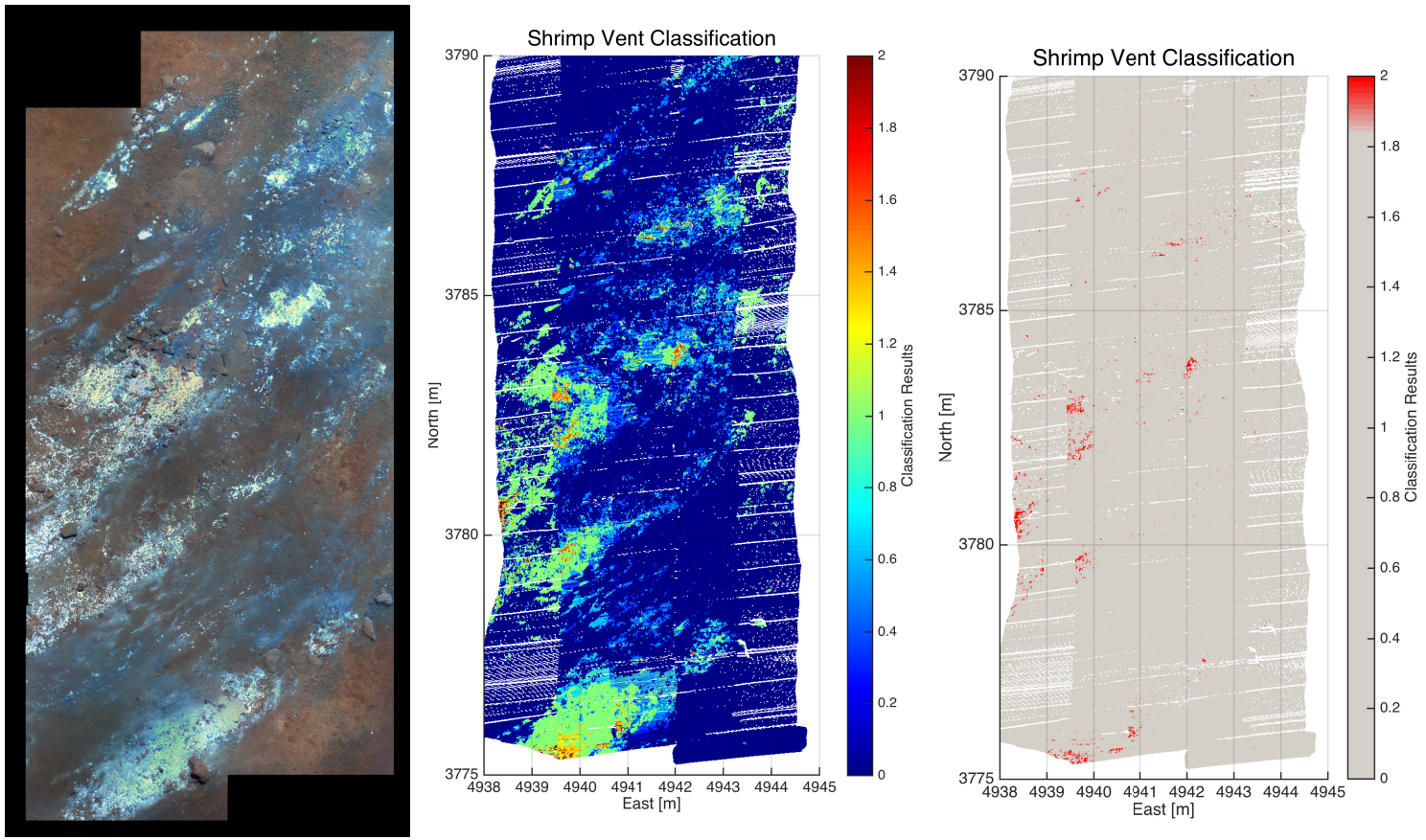

(a) (b) (c)

Figure 1.19: Results of the updated vent detection algorithm. (a) 2D photomosaic of the Shrimp Vent area. (b) Gridded results of the SVM classification method showing seafloor (blue), bacteria (green) and active venting (red). (c) Classification algorithm results showing only areas of active venting in red. The main area of sampling is located at 4942m East and 3784m North.

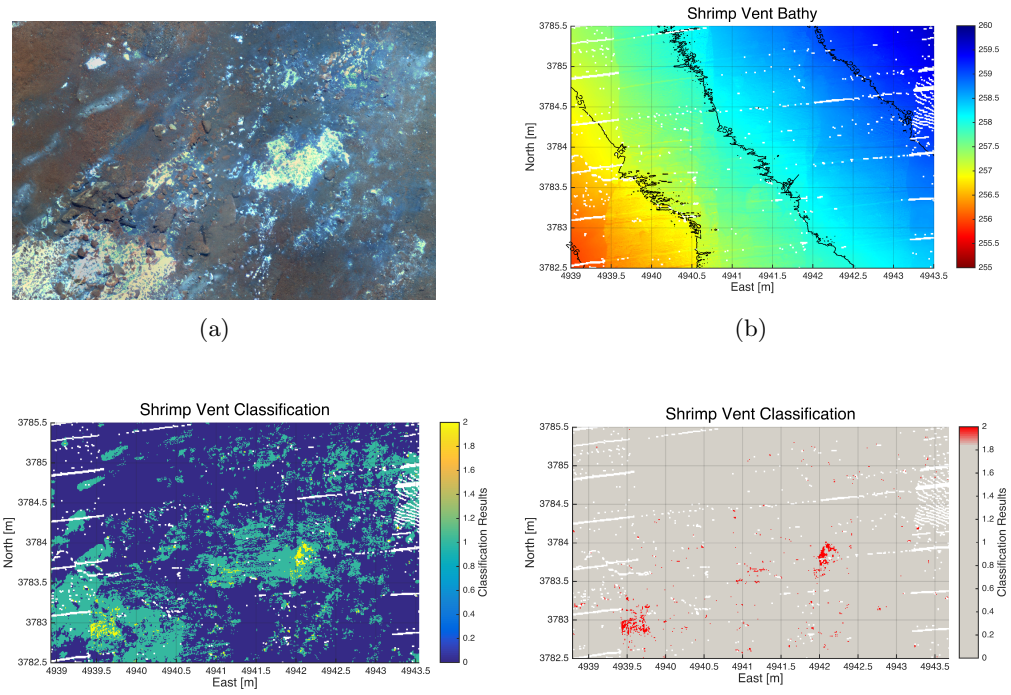

(a) (b)

(c) (d)

Figure 1.20: Shrimp vent maps focused about the primary sampling vent site. (a) Photomosaic shows distribution of bacterial mats within the area. (b) Contoured laser bathymetric map showing the 45° slope along the side of the crater. (c) Classification results which have been gridded and rounded to discrete classification values between 0-2 representing seafloor (0, blue), bacteria (1, green) and active venting (2, yellow). (d) Classification results showing only the areas of active venting in red indicating the spatial distribution of active venting.

of diffuse flow. Comparison between the mosaic and this classification result illustrates successful differentiation between seafloor (blue) and bacteria (green), independent of terrain and image acquisition settings. The spatial distribution of small areas of diffuse flow is apparent when viewing only the areas of determined to be part of the active vent class which are shown in red in Figure 1.19(c). The lack of coherence within these areas indicates low rate diffuse flow, likely seeping around rocks and through cracks, as opposed to point source venting as observed at the other previously discussed sites studied within the Kick'em Jenny crater.

Extensive imaging and sampling was completed within this area, and while low flux diffuse venting was prevalent it was usually located while closely examining the shrimp. The main sampling area, Figure 1.18(a) is depicted in Figure 1.20, right of center. The obvious slope within the HD image is depicted by the contoured bathymetric map in Figure 1.20(b) which indicates a 45° grade. The complete classification results, Figure 1.20(c), can be compared to the mosaic. At the active vent site (coordinates 4942, 3784 in Figure 1.20) biological samples, water samples and temperature samples were collected. The maximum recorded temperature was 113.9°C within this vent, while the ambient temperature was 14.8°C. This reading was the highest with other flow in the area registering temperatures closer to 35°C.

1.5 Discussion

1.5.1 Scientific benefits and implications

Systematic remote detection of diffuse seafloor venting will increase comprehensive understanding of the distribution of low flux hydrothermal flow and improve estimates for thermal and chemical ocean budget computations. The ability to generate a comprehensive map of active venting with a remote survey method is far more efficient than the classic approach of locating shimmering water through detailed inspection. The ability to detect bacteria and associated biological communities which thrive in the presence of hydrothermal or cold seep activity holds additional scientific merit.

1.5.2 High Resolution Mapping

Viewing Data

Laser line classification results can be viewed in two ways, geo-spatially or temporally. Accurate geo-spatial maps created by combining laser and navigation data requires down sampling of the laser data through averaging. Although this approach creates a smooth map, fills holes, averages outliers and masks discontinuities, vent activity smaller than $20cm^2$ and represented by very few pixels may be lost to averaging. Therefore, vent sites discussed in this paper were gridded on a fine scale to increase the depiction of vent detection at the expense of a clean map.

Detailed analysis of each laser line pixel is possible when data is viewed temporally, or as a waterfall image, as in Figure 1.10. Although navigation data is unaccounted for, the laser line image index can be cross referenced with vehicle time, navigation, sampling data and stereo images for vent confirmation.

Navigation

Impacts of navigation error within a survey were minimized by incorporating ground truth data. Navigation sensors on *ROV Hercules* include a doppler velocity log (DVL) and a ultra short baseline (USBL) transponder system. The DVL documents current position with respect to the previous position and can accumulate error resulting in navigation drift, causing misalignment over large surveys. The acoustic USBL system operates between the ship and the vehicle on the seafloor and becomes less accurate in the presence of unknown density stratification due to mixing and while the vehicle is operating near a vertical surface, like a crater wall. Both these scenarios were present while working within the Kick'em Jenny Volcano Crater resulting in USBL navigation errors up to 10m. Ground truth data including images of *ROV Hercules* and key geologic features captured by *ROV Argus's* HD camera, bathymetric maps and 2D mosaics were critical in determining sample and vent locations.

Structured Light Laser Calibration

Calibration of the structured light laser system impacts range normalization, the quality of gridded data and automated registration between imaging data products. Detailed in [18] this calibration processes is complex and an active area of research. During intensity range normalization the actual range value (Equation 1.2) requires an accurate calibration to establish the distance between the camera and seafloor. Although intensity errors within a given field season will be systematic and slight given a range error on the order of centimeters, range values should be verified using vehicle navigation when comparing data from multiple field seasons. Within gridded data, calibration error is most noticeable as bathymetric discontinuities between adjacent survey lines and becomes more apparent when data is gridded on a fine scale. Additionally, a precise laser calibration will allow for automated correlation between sampled laser pixels and stereo images. This registration will allow for texture and color information associated with the stereo images to be an additional feature in seafloor classification algorithms.

1.5.3 SVM Classification Algorithm

Training Data and Site Specific SVM Development

The presented classifier was created using data from three distinct sites and has been applied to multiple vent fields with a range of environmental and vent characteristics. Seafloor points were selected over various types of substrate including flocculant sediment, hard substrate, rocky outcrops and pillow basalt. The SVM component corresponding to seafloor classification will set the lower limits on intensity and second moment values for bacteria and vent classification, effectively determining the vent detection sensitivity of the classifier. Therefore, without *a prioi* knowledge of the seafloor type within a target vent field, a classifier composed of many types of seafloor data is important.

Similarly, the classifier must have been trained on the type of venting to be detected. For example, an SVM classifier was trained using the seafloor and bacteria data collected at the Spider Seep site and points collected over pillow basalt seafloor, bacteria and venting data from the Iguanas Vent Field, Galapagos which included relatively high flux,

high temperature point source venting emanating from chimney-like structures. Using hand-tagged data collected at a small low temperature focused flow vent on the Mid-Cayman rise as test data for this SVM resulted in approximately 57% of the vent data being misclassified, details are presented in Table 1.2 and Figure 1.21(a). Conversely, when classifying the same data was using an SVM classifier developed with that same Cayman data and the Spider Seep data 76% of vent data is classified correctly (Table 1.2. While using the same data for testing as training should produce the best results, in this case, the upper bound of the seafloor classification region is significantly lower which increases sensitivity to low flux venting. This example illustrates the importance of using training data collected at vents with characteristics similar to those to be detected, Figure 1.21(b). The ability of a classifier to detect both high and low flux active venting is the result of being trained using data from multiple vent sites and should be applied when detection of a venting with various or unknown characteristics is desired.

However, given *a prioi* knowledge of the area with potential vent sites, the SVM classifier can be optimized based on the type of seafloor and anticipated venting. In practice, once on site, data gathered during small survey, on the order of 15m by 15m, can be used as training data. Ideally, this site would include active venting, seafloor and bacteria, however, it is not required. Training an SVM using plentiful site specific seafloor data and previously gathered classification points from a vent site with desired characteristics will result in an accurate classification. If the sample survey does not include bacteria previously obtained points may also be used.

Hand labeling SVM training data requires gathering features from well understood surveys with varying seafloor, biological and venting characteristics. The process of hand selecting a specific pixel indicative venting, bacteria or seafloor is prone to error, especially in areas where active flow is surrounded by bacteria. Without direct correlation between ground truth data for each pixel, this error is unavoidable. However, the size and diversity of the training data set will minimize the impact of mislabeled training data. While an ideal training data set would include an equal number of samples from each class, seafloor is very prevalent, bacteria less so and confirmed venting is rare.

	Total	Seafloor	Bacteria	Venting
Cayman Vent Classification with Iguanas & Spider SVM				
Data Points	541	323	0	218
Correctly Classified	72.6%	82.7 %	0	57.8%
Misclassified Data Points				
Total	148	56	0	92
as Seafloor		N/A	0	76
as Bacteria		56	N/A	16
as Venting		0	0	N/A
Cayman Vent Classification with Cayman & Spider SVM				
Data Points	541	323	0	218
Correctly Classified	89.3%	97.8 %	0	76.6%
Misclassified Data Points				
Total	58	7	0	51
as Seafloor		N/A	0	20
as Bacteria		5	N/A	31
as Venting		2	0	N/A
Cayman Vent Classification with Original SVM				
Data Points	541	323	0	218
Correctly Classified	81.7%	87.3 %	0	73.4%

Table 1.2: Support vector machine metrics testing the Cayman Vent data as a data set on an SVM classifier developed using Iguanas Vent and Spider Seep data. Because type of venting present at Cayman was not used in the classification routine only 57.8% of the vent data is correclty classified.

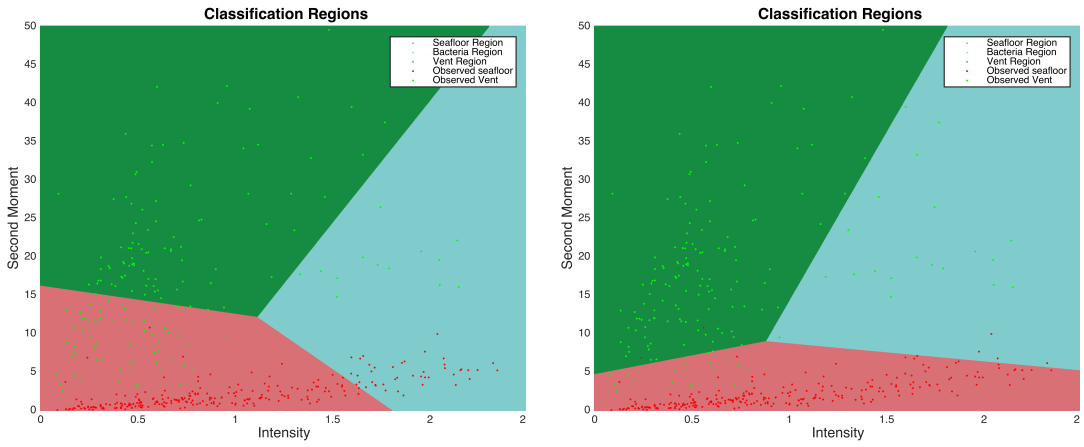

(a) (b)

Figure 1.21: Hand labeled data collected at the Mid-Cayman Rise Vent site used as a test data set plotted over the SVM classification space. (a) The SVM developed using data from the Iguanus Vent Site and Spider Seep causes misclassificaiton of percentage of vent data points as similar venting was not used during training. (b) Conversely an SVM developed using Cayman and Spider Seep training data is much more accurate.

Detection Limitations

Turbulence and flux appear to have more affect on successful detection than temperature. For instance, the temperature of the vent successfully detected within Kick'em Jenny (Section 1.4.1) was only 7.5°C above ambient. However, the clearly observable focused flow indicated substantial flow and turbulence. In comparison, at the Mid-Cayman Rise in 2013 small pools of venting fluid were discovered next to rocky substrate. Their recorded temperature was approximately 4°C above ambient with hardly any discernible flow rate. Venting was not detected within the survey using the presented SVM. The calculated second moment was slightly higher than the seafloor within the immediate vicinity, but still below SVM vent classification limits. The low temperature differential between these two sites implies successful detection relies on turbulent flow of fluid density anomalies.

Classification Error

Due to the natural variability in the environments surveyed perfect classification will not be possible. Seafloor characteristics define the lower vent detection boundary for laser line spread, which faint diffuse flow and quickly diffusing plumes may not exceed. This scenario is outlined by the example in Table 1.2. Additionally, in the presence of active venting the laser light scatters, effectively decreasing the recorded intensity values while increasing the spread of the laser line. Unfortunately, active venting occurring over bacteria may return high intensity values and be classified as bacteria. There is still value in this result as bacteria is typically an indication of active hydrothermal activity.

The presented algorithm successfully detects active diffuse flow within an undisturbed environment. However, external disturbances, such as stirred up sediment and man-made objects can alter the laser line and be identified as either bacteria or venting. For example, fine sediment stirred up by fish or can cause scattering of the laser line effectively increasing the width. This error can be manually identified by checking the associated stereo images for a dust cloud. The vehicle flies at a constant altitude meters above the seafloor and rarely disturbs sediment during a survey. Man -made objects

including reflective metal, trash and scientific markers are not prevalent enough to be accounted for in the classification process and are generally classified as bacteria due to highly reflective nature and can quickly be identified within the stereo images.

1.6 Conclusions

Diffuse hydrothermal venting was successfully detected by applying an improved SVM classification algorithm to data collected systematically and remotely by the structured light laser system. Intensity normalization of the raw laser data eliminated errors due to exposure settings, non-uniformity of the laser line and seafloor bathymetry. The SVM method was developed to classify this normalized data as plain seafloor, biologic activity, or active venting. Successful detection has been established across multiple surveys collected within various environments over multiple years.

List of References

[1] C. J. Smart, C. Roman, and S. N. Carey, "Detection of diffuse seafloor venting using structured light imaging," *Geochemistry, Geophysics, Geosystems*, vol. 14, no. 11, pp. 4743–4757, 2013. [Online]. Available: http://dx.doi.org/10.1002/ggge.20280

[2] A. Schultz, J. R. Delaney, and R. E. McDuff, "On the Partitioning of Heat Flux Between Diffuse and Point Source Seafloor Venting," *Journal of Geophysical Research*, vol. 97, no. B9, pp. 12 299–12 314, 1992.

[3] J. B. Corliss, J. Dymond, L. I. Gordon, J. M. Edmond, R. P. von Herzen, R. D. Ballard, K. Green, D. Williams, A. Bainbridge, K. Crane, and T. H. van Andel, "Submarine thermal springs on the galapagos rift," *Science*, vol. 203, pp. 1073–1083, 1979.

[4] M. D. Hannington, C. D. J. de Ronde, and S. Petersen, "Sea-floor tectonics and submarine hydrothermal systems," *Economic Geology*, vol. 100th Anniversary, pp. 111–141, 2005.

[5] C. R. German, D. R. Yoerger, M. Jakuba, T. M. Shank, C. H. Langmuir, and K. Nakamura, "Hydrothermal exploration with the autonomous benthic explorer," *Deep-Sea Research Part I: Oceanographic Research Papers*, vol. 55, no. 2, pp. 203–219, 2008.

[6] H. Singh, F. Weyer, J. Howland, A. Duester, D. Yoerger, and A. Bradley, "Quantitative stereo imaging from the autonomous benthic explorer (abe)," in *OCEANS '99 MTS/IEEE. Riding the Crest into the 21st Century*, vol. 1, 1999, pp. 52–57 vol.1.

[7] T. Shank, D. Fornari, D. Yoerger, S. Humphris, and A. Bradley, "Deep Submergence Synergy: Alvin and ABE Explore the Galapagos Rift at 86 W," *EOS Transactions of the AGU*, vol. 84, no. 41, pp. 425–440, October 2003.

[8] D. S. Scheirer, T. M. Shank, and D. J. Fornari, "Temperature variations at diffuse and focused flow hydrothermal vent sites along the northern east pacific rise," *Geochemistry Geophysics Geosystems (G3)*, vol. 7, no. 3, pp. 1525–2027, 2006.

[9] P. Rona, "Sonar images hydrothermal vents in seafloor observatory," *EOS Transactions of the AGU*, vol. 92, no. 20, pp. 169–170, May 2011.

[10] R. Light, V. Miller, P. Rona, and K. Bemis. "Acoustic instrumentation for imaging and quantifying hydrothermal flow in the neptune canada regional cabled observatory at main endeavour field." PDF. 2012. [Online]. Available: http://www.apl.washington.edu/project/projects/covis/pdfs/COVIS_concept_operation.pdf

[11] K. C. Bell, P. Nomikou, S. Carey, E. Stathopoulou, P. Polymenakou, A. Godelitsas, C. Roman, and M. Parks, "Continued exploration of the santorini volcanic field and cretan basin aegean sea," *Oceanography*, vol. 25(1), no. supplement, 2012.

[12] R. C. Millard and G. Seaver, "An index of refraction algorithm for seawater over temperature, pressure, salinity, density, and wavelength," *Deep-Sea Research Part A*, vol. 37, no. 12, pp. 1909–1926, December 1990.

[13] H. Richard and M. Raffel, "Principle and applications of the background oriented schlieren (bos) method," *Measurement Science and Technology*, vol. 12, pp. 1576–1585, 2001.

[14] S. B. Dalziel, G. O. Hughes, and B. R. Sutherland, "Whole-field density measurements by 'synthetic schlieren'," *Experiments in Fluids*, vol. 28, pp. 322–335, 2000.

[15] P. Rona, D. R. Jackson, T. Wen, C. Jones, K. Mitsuzawa, K. G. Bemis, and J. G. Dworski, "Acoustic mapping of diffuse flow at a seafloor hydrothermal site: Monolith vent, juan de fuca ridge," *GRL*, vol. 24, no. 19, pp. 2351–2354, 1997.

[16] D. R. Jackson and J. G. Dworski, "An acoustic backscatter thermometer for remotely mapping seafloor water temperature," *Journal of Geophysical Research: Oceans*, vol. 97(C1), pp. 761–767, 1992.

[17] C. Roman, G. Inglis, and J. Rutter, "Application of structured light imaging for high resolution mapping of underwater archaeological sites," in *IEEE Oceans, 2010. Proceedings on*, 2010.

[18] G. Inglis, C. Smart, J. Vaughn, and C. Roman, "A pipeline for structured light bathymetric mapping," in *Intelligent Robots and Systems, Proceedings. October 7-12, IEEE/RSJ International Conference on*, 2012.

[19] K. D. Moore, J. S. Jaffe, and B. L. Ochoa, "Development of a new underwater bathymetric laser imaging system: L-Bath," *J. Atmos. Oceanic Technol.*, vol. 17, no. 8, pp. 1106–1117, 2000.

[20] K. Moore and J. Jaffe, "Time-evolution of high-resolution topographic measurements of the sea floor using a 3-d laser line scan mapping system," *Oceanic Engineering, IEEE Journal of*, vol. 27, no. 3, pp. 525 – 545, Jul 2002.

[21] F. Bruno, G. Bianco, M. Muzzupappa, S. Barone, and A. Razionale, "Experimentation of structured light and stereo vision for underwater 3D reconstruction," *ISPRS Journal of Photogrammetry and Remote Sensing*, vol. 66, no. 4, pp. 508 – 518, 2011.

[22] S. Tetlow and J. Spours, "Three-dimensional measurement of underwater work sites using structured laser light," *Measurement Science and Technology*, vol. 10, no. 12, pp. 1162–1167, Dec. 1999.

[23] C. Roman, G. Inglis, J. I. Vaughn, C. Smart, B. Douillard, and S. Williams, "The development of high-resolution seafloor mapping techniques," *Oceanography*, vol. 25(1), no. supplement, 2012.

[24] "New frontiers in ocean exploration: The e/v nautilus and noaa ship okeanos explorer 2015 field season," *Oceanography*, vol. 29, no. 1, p. 84, Supplement 2016.

[25] J. C. Kinsey and L. L. Whitcomb, "Preliminary field experience with the dvlnav integrated navigation system for oceanographic submersibles," *Control Engineering Practice*, vol. 12, pp. 1541–1549, 2004.

[26] U. G. I. Thormahlen, J. Straub, "Refractive index of water and its dependence on wavelength, temperature and density," *Journal of Physical Chemistry*, vol. 14, pp. 933–945, 1985.

[27] C. D. Mobley, *Light and Water Radiative Transfer in Natural Waters*. Academic Press, 1994.

[28] N. Otsu, "A threshold selection method from gray-level histograms," *IEEE Transactions on Systems, Man, and Cybernetics*, vol. 9, no. 1, pp. 62–66, Jan 1979.

[29] B. Luzum, M. Starek, and K. C. Slatton., "Normalizing alsm intensities," Geosensing Engineering and Mapping (GEM) Civil and Coastal Engineering Department, University of Florida, USA., GEM Center Report No. Rep 2004-07-001., 2004.

[30] B. E. Boser, I. M. Guyon, and V. N. Vapnik, "A training algorithm for optimal margin classifiers," in *Proceedings of the Fifth Annual Workshop on Computational Learning Theory*, ser. COLT '92. New York, NY, USA: ACM, 1992, pp. 144–152. [Online]. Available: http://doi.acm.org/10.1145/130385.130401

[31] S. Carey, R. Ballard, K. L. Bell, R. J. Bell, P. Connally, F. Dondin, S. Fuller, J. Gobin, P. Miloslavich, B. Phillips, C. Roman, B. Seibel, N. Siu, and C. Smart, "Cold seeps associated with a submarine debris avalanche deposit at kick'em jenny volcano, grenada (lesser antilles)," *Deep Sea Research Part I: Oceanographic Research Papers*, vol. 93, pp. 156–160, November 2014.

MANUSCRIPT 2

Implications of Range on Detection of Diffuse Venting using the Structured Light Laser Sensor

by

Clara J. Smart [1], Chris N. Roman[2]

In preparation for submission to Geochemistry, Geophysics, Geosystems (G^3)

[1]Ph.D. Candidate, Department of Ocean Engineering, The University of Rhode Island, Narragansett RI 02882. Email: csmart@my.uri.com

[2]Asst. Prof of Oceanography, Graduate School of Oceanography/Department of Ocean Engineering, The University of Rhode Island, Narragansett RI 02882. Email: cnr@gso.uri.edu

Abstract

Algorithms for detection of diffuse hydrothermal venting using the structured light laser sensor have proven to be successful. However, potential limitations of survey parameters, including altitude and vehicle heading, have not been explored. To determine the implications of these survey parameters data from twelve surveys conducted over a single hydrothermal vent at three different altitudes and four different headings are analyzed. Survey altitude variations will impact the resolution and intensity of the laser images, therefore processing considerations to maintain signal quality are presented. Detection sensitivity resulting from differing survey altitude and vehicle heading will also be presented. Analysis of these configurations suggest successful detection from survey altitudes greater than 6m. The affect of range, resolution and direction are important for future applications of this sensor which may include surveying from higher, faster flying autonomous underwater vehicles (AUV).

2.1 Introduction

2.1.1 Justification for Study

Algorithms for detecting diffuse hydrothermal flow using a structured light laser sensor have been previously developed [1]. Distortion in a projected laser line due to interaction with fluid density anomalies can be detected using image processing techniques. The resulting data allow for the creation of maps indicating the spatial distribution of areas of active venting. A typical vehicle survey altitude for optical imaging is 3m, and while slight variations in range on the order of a meter occur within and between surveys, the implications of surveying at higher altitudes have not been considered. The impacts of increasing range and increasing light attenuation on signal quality, and vent detection limitations are the premise of this study.

Currently, the structured light laser sensor is a component of a high resolution remotely operated vehicle (ROV) imaging system which also includes stereo cameras and a multibeam sonar, Figure 2.1. Using the ROV's closed loop control system and suite of navigation sensors it is possible to survey at a consistent altitude between 2-5m, traveling approximately 0.2m/s in an organized pattern. Future intentions for the structured light

laser sensor include integration into higher, faster flying autonomous underwater vehicles (AUV). Bathymetric mapping surveys completed by AUVs at hydrothermal vent sites are typically flown at altitudes of 8-15m [2, 3]. Therefore establishing the laser vent detection limitations will inform future design considerations and scientific applications.

2.1.2 Structured Light Laser Sensor

The structured light laser sensor consists of a 12-bit 1360 x 1024 pixel mono Prosilica GC1380 camera which images a verged 100mW, 532nm Coherent Powerline sheet laser projected on the seafloor. The vertical position of the laser line within each image capture is proportional to range and can be converted to a single bathymetric profile, analogous to a single ping of range data from a multibeam sonar [5]. Additionally, the combination of the intensity and spread of the laser line allow for the detection of diffuse hydrothermal venting (Chapter 1.6) [1]. The laser line is imaged at approximately 20Hz, creating a survey resolution better than one laser line per centimeter along track and 2-4 points (pixels) per centimeter across track, with an associated range resolution of 0.5cm per camera pixel at an altitude of 3m. During a complete mapping survey strobe lit stereo images are simultaneously acquired every 3 seconds and interlaced with the laser frames while the multibeam operates at 5-15Hz.

2.1.3 Laser Line Extraction

Raw images which capture the laser line incident with the seafloor are standard 12-bit black and white photos from which the position and intensity of the laser line is determined. Figure 2.2(a) is an example of a raw laser line image, displayed on a log intensity scale. Using Otsu's thresholding method [6] a binary mask of the image is created, effectively isolating the laser line. Each column within the image is then processed and viewed as an independent 1D signal containing the laser line cross-section. The location of the laser line is determined by the pixel with the the maximum intensity value, v^*. An extracted laser line is displayed in Figure 2.2(b). Batch processing algorithms for isolating the laser line are further detailed in [5].

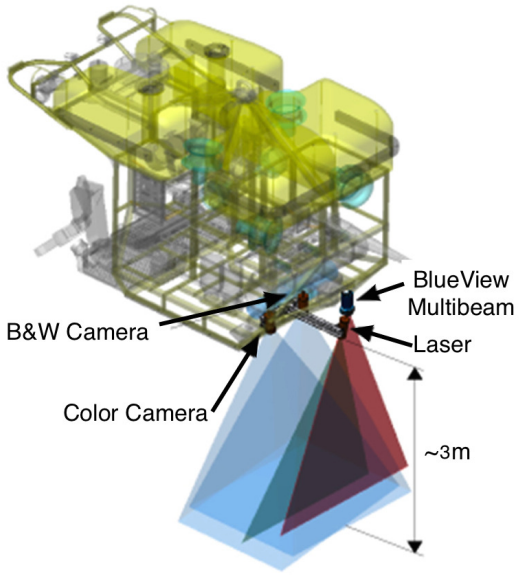

Figure 2.1: A computer rendering of ROV *Hercules* showing the stereo camera pair, structured light laser and 1350kHz multibeam sonar.

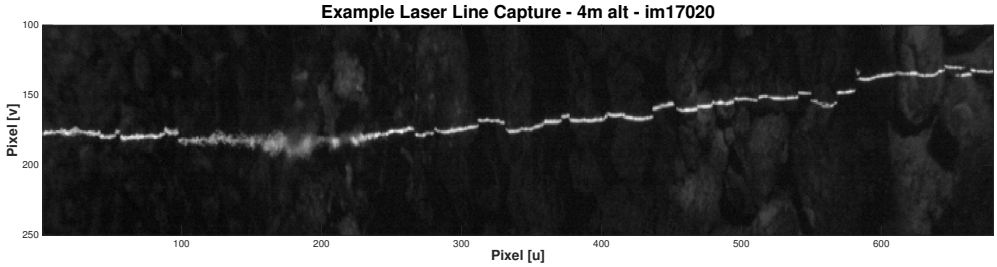

(a)

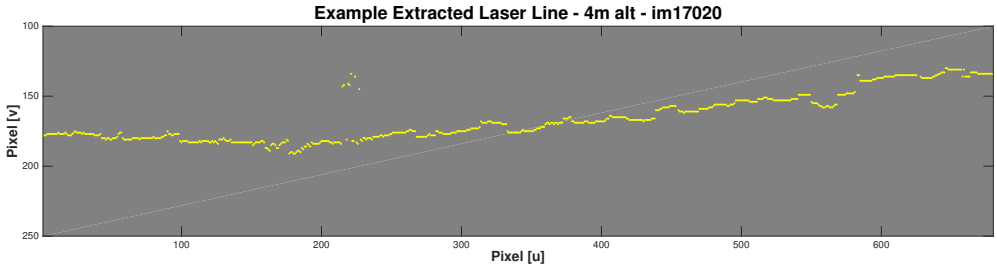

(b)

Figure 2.2: Laser line acquisition and extraction example. (a) A raw laser line image displayed on a log intensity scale. The laser is crisp on the right half of the frame and active venting occurs just left of center, pixels 150-200, where the laser line becomes blurred. (b) The extracted laser line corresponding to the peak columnwise intensity.

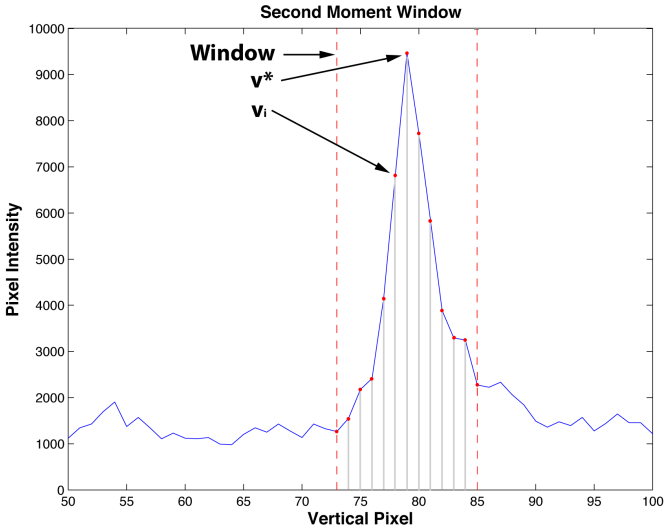

Figure 2.3: Cross section of the laser line annotated to define the variables considered for computation of the weighted second moment about the centroid of the line, Equation 2.1.

Interaction with Density Anomalies

As the structured light sensor passes over active hydrothermal fluids the associated turbulent density anomalies cause the laser light to scatter along the optical path and appear blurred instead of crisp within the captured image [1]. This blurring is visible in Figure 2.2(a) on a section of the laser line, to the left of center, which appears less crisp than the laser line displayed right of center.

An insightful computation for establishing the spread of the laser line, which serves as a proxy for active venting, is the unitless intensity weighted second moment about the peak intensity value of the laser line. This is computed for each image column by

$$\sum_{i=v^*-\frac{w}{2}}^{v^*+\frac{w}{2}} r_i(v_i - v^*)^2, \tag{2.1}$$

where v_i and r_i are the comparison pixel location and intensity respectively, w is the size of the widow about the laser line peak, v^*. Figure 2.3 shows a cross section of the laser line identifying these parameters.

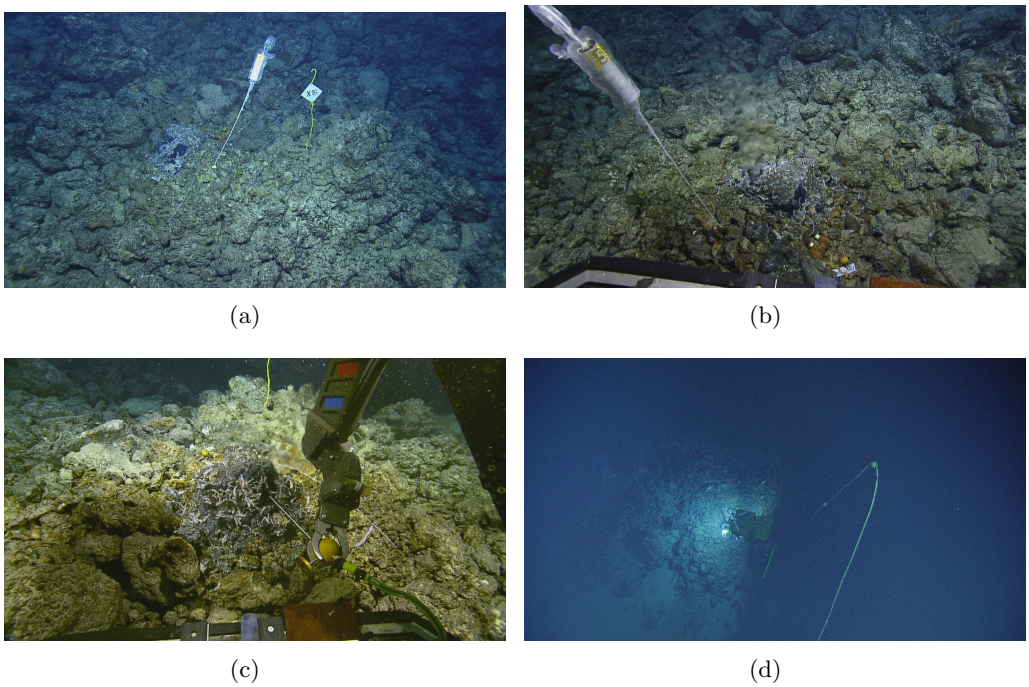

(a) (b)

(c) (d)

Figure 2.4: Images of the vent site acquired with the ROV mounted HD video cameras. (a) Focused flow surrounded by rocky seafloor and both markers are visible. (b) The blur in the center of the photo indicates actively venting fluid from the vent orifice. (c) Temperature data were collected at the vent site. Shrimp are visible around the orifice. (d) ROV *Hercules* conducting the high resolution survey, the green laser line is visible below the vehicle.

2.2 Site Overview and Data Acquisition

The approximately 110km long Mid-Cayman Spreading Center is located within the Cayman Trough of the Caribbean Sea and is one of the worlds deepest ultra slow spreading centers. Multiple discrete hydrothermal vent sites have been located, including the Von Damm Vent at a depth of 2300m along the upper slopes of the Mount Dent Oceanic Core Complex [7]. The isolated small hydrothermal vent presented in this study is located within this vent field. This site was previously visited during the 2012 OASES Research Cruise using the ROV *Jason* and by the deep submergence vehicle (DSV) *Shinkai 6500* during the YK13-05 cruise in 2013. Scientific markers, floating a meter above the seafloor, were left at the site during both explorations [8]. A metal diamond shaped marker labeled 'X-16' was placed meters from the vent while a second white tube-like marker labeled '154' was placed next to the vent orifice. Both markers are visible in Figure 2.4(a).

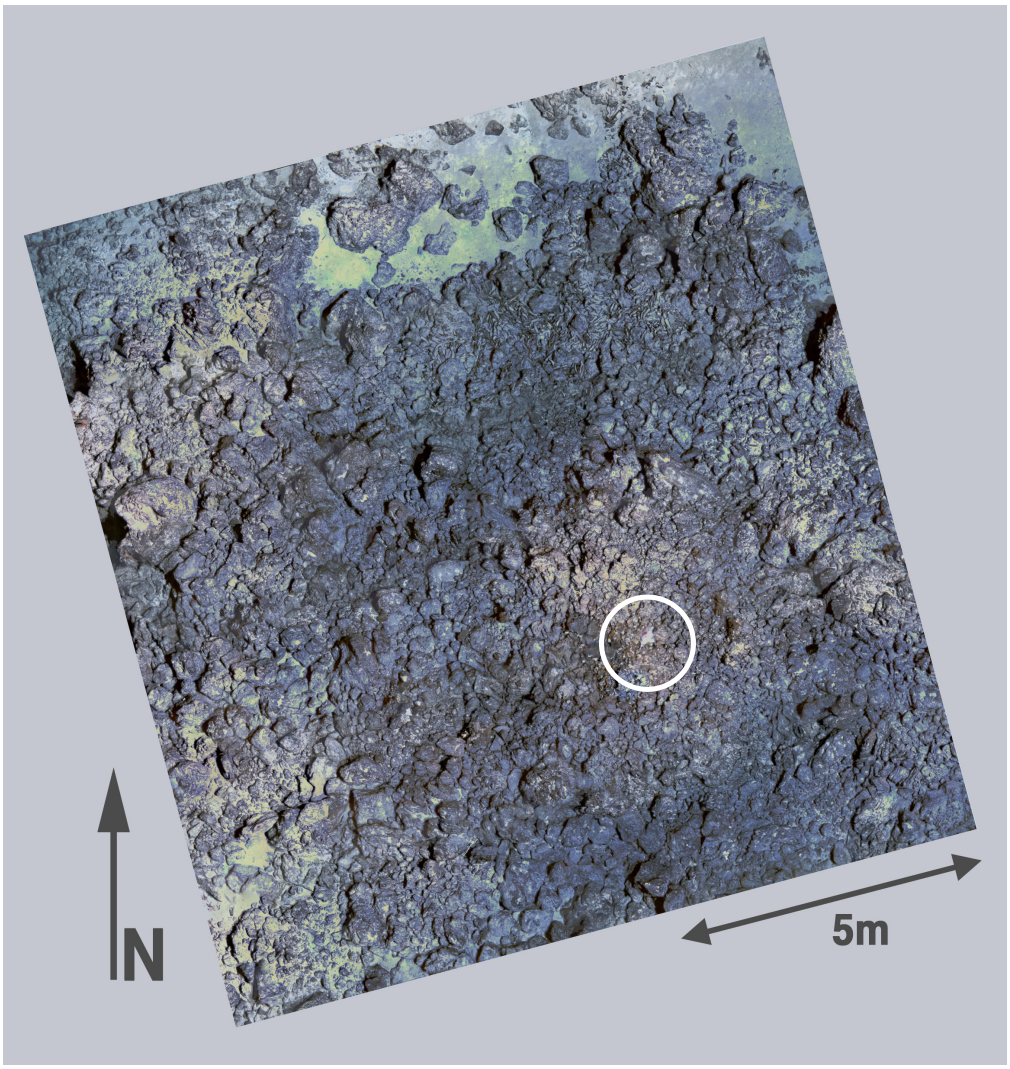

Figure 2.5: Mosaic of the survey area containing a single small hydrothermal vent, circled in white, it is barely distinguishable within this image as blur. The area is rocky with mussel shells, minimal biology near the vent orifice and scientific markers from previous expeditions. This image was assembled using images collected from an altitude of 4m.

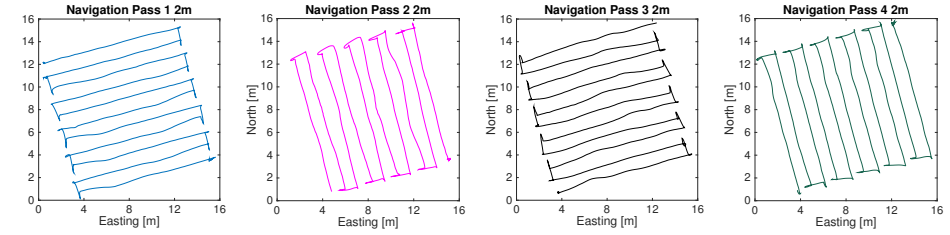

(a)

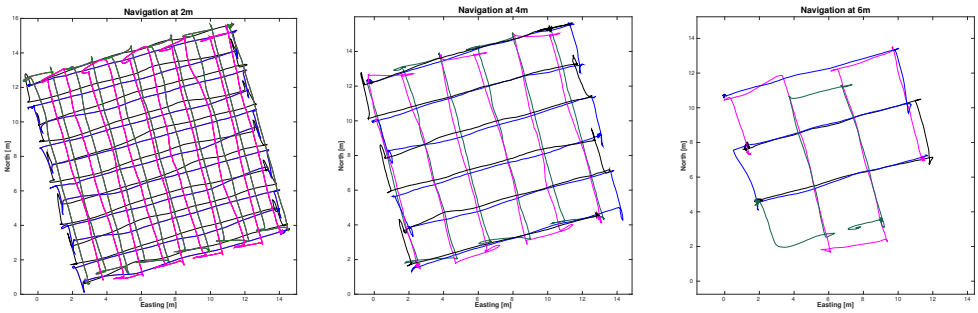

(b) (c) (d)

Figure 2.6: Navigation corresponding to three surveys at nominal altitudes of 2.7m, 4.2m, and 6.2m. The area was surveyed with four different headings at each altitude. (a) Navigation corresponding to the four surveys completed at an altitude of 2.7m with the vehicle headings set to (from left to right) 75 deg, 165 deg, 255 deg and 345 deg. (b) All four 2.7m surveys. (c) The four surveys completed at 4.2m. (d) Navigation for the 6.2m surveys.

Exploration of the vent site on August 21, 2013 using the *ROV Hercules*, operating from *E/V Nautilus*, included collecting high definition video footage and temperature data. A small but visible rising plume was observed a meter above the rocky seafloor and is visible as blur in the center of Figure 2.4(b). Clear, low level focused flow emanated from an approximately 10cm wide vent orifice around which small shrimp are present, Figure 2.4(c). Collected temperature data indicated ambient seawater was 4.25°C and the maximum temperature of the venting fluids was 29.52°C. The rocky nature of the site is apparent in Figure 2.4(d) and the green laser line is visible below the ROV. The surrounding area contained minimal bacterial mat coverage, a few shrimp, many dead mussel shells and scientific markers.

2.2.1 Survey methodology

To determine how vent detection results potentially vary with altitude and sheet laser direction a series of survey grids with varying altitudes and vehicle headings were

completed over an approximately 15m x 15m area around the single hydrothermal vent, Figure 2.5. The three resulting survey altitudes were 2.7m, 4.2m, and 6.2m above the seafloor. This paper will refer to the surveys as the 2m, 4m, and 6m surveys respectively. The vent orifice was passed over at four different vehicle headings at each altitude, $75°, 165°, 255°$ and $345°$, resulting in twelve individual surveys of the area. The resulting navigation for each altitude is shown in Figure 2.6. The entire survey was completed within 2.5 hours. Simultaneous data are collected by the stereo camera system and multibeam sonar.

ROV *Hercules* is closed loop controlled and capable of executing tracklines at prescribed velocities, altitudes and depths. The navigation sensor suite includes a 600kHz RDI Doppler Velocity Log (DVL), IXSEA OCTANS fiber-optic gyroscope and a Paroscientific depth sensor [9]. These data are collected using the DVLNAV software package [10].

2.3 Impact of Range on Geometry

The structured light laser system is mounted on a rigid frame and calibrated. No adjustments are made to the laser angle or system geometry for changes in survey altitude. Specifically, the sheet laser has a 30° x 40° field of view and is mounted at an 11.7° angle. This intersects the center of the field of view of the mono 1024 x 1360 pixel camera from an altitude of 3m. In an effort to reduce bandwidth to maximize laser frame rate during acquisition, the laser images are horizontally down-sampled to 680 pixels and cropped vertically. The laser line field of view and projection distance (the distance between the laser and seafloor) will increase with range while resolution will decrease. Table 2.1 summarizes resolution and geometric changes based on altitude. Projection distance is defined as the distance between the laser source and seafloor and is slightly greater than vehicle altitude as the laser is verged.

2.4 Impact of Range on Detection

Given changes in both resolution and the optical path length it is expected that the characteristics of the imaged laser line will also be altered as a function of range.

Altitude	**Field of View**		**Pixels per cm**		**Projection**
Meter (m)	Vert. (m)	Horiz. (m)	Full Frame	Decimated Horiz.	Dist. (m)
2.0	1.07	1.46	9.34	4.67	2.04
2.5	1.34	1.82	7.47	3.74	2.55
3.0	1.61	2.18	6.23	3.11	3.06
3.5	1.88	2.55	5.34	2.67	3.57
4.0	2.14	2.91	4.67	2.34	4.08
4.5	2.41	3.28	4.15	2.08	4.60
5.0	2.68	3.64	3.74	1.87	5.11
5.5	2.95	4.00	3.40	1.70	5.62
6.0	3.22	4.37	3.11	1.56	6.13

Table 2.1: Geometric and resolution values corresponding to survey altitudes between 2m and 6m.

2.4.1 Attenuation in Seawater

Attenuation of light in seawater is dependent on range and absorption. Range is determined by the vehicle altitude and includes both the ray path from the laser to the seafloor and the return path to the camera, making the attenuation distance roughly twice the survey altitude. The attenuation coefficient is dependent on the wavelength of the laser as well as on the water chemistry and particulates within the water column. As true scattering values are unknown for this site, the diffuse attenuation coefficient for 'irradiance of clearest ocean waters' of 0.0519m^{-1} for pure seawater at a wavelength of $\lambda = 530\text{nm}$ given in [11] will be used. The total loss due to attenuation can be calculated using Beer-Lambert's Law

$$I_r = I_i * e^{-kr}, \tag{2.2}$$

where I_i is the initial intensity of the light, $k = 0.0519\text{m}^{-1}$ is the attenuation coefficient, r is range, and I_r represents the resulting intensity. Initial computations indicate that at a survey altitude of 2.7m $I_r = I_i * 0.75$ while at 6.2m $I_r = I_i * 0.53$. The diffuse attenuation coefficient for pure seawater is a low estimate for this field site and the actual losses are likely higher.

2.4.2 Intensity Variations

As expected the intensity of the imaged laser line and range are inversely proportional. Figure 2.7(a) shows the mean of 680 aligned laser line cross sections captured over an area with no venting. Due to increased attenuation the 6m peak intensity is approximately 55% lower than the 2m data. This difference is greater than the theoretical 30% decrease in intensity between the two survey altitudes, likely because the theoretical values are computed in ideal seawater.

Intensity normalization computations which include range compensation can compensate for the intensity difference by multiplying the measured intensity by the ratio between the measured and desired range. The adjusted intensity results are very similar, Figure 2.7(b), and effectively represent data collected from a single known altitude. This computation allows for direct comparison of intensity values between data collected from various altitudes.

2.4.3 Signal to Noise Ratio

Within a range normalized image the desired signal is the laser line while noise is defined as the surrounding seafloor, which is primarily black. Despite the reduction in image intensity with increased range, the signal to noise ratio does not significantly degrade. This is illustrated by Figure 2.7(c) in which the mean of normalized background values, located on either the laser line peak, show little deviation between the two altitudes. Further examples are shown in Figure 2.8 which compares all 680 aligned laser line cross sections from within a single image without venting. The comparison between the normalized data surrounding the laser line within the 2m and 6m data is shown in Figures 2.8(b) and 2.8(d). While noise levels increase with range the noise floor in both cases is less than 3% of the maximum of the normalized intensity. Therefore, the signal to noise ratio does not degrade notably up to a survey altitude of 6.2m.

2.5 Processing Considerations

Detection of diffuse hydrothermal venting using the structured light laser sensor utilizes an intensity weighted second moment to capture the blur associated with the

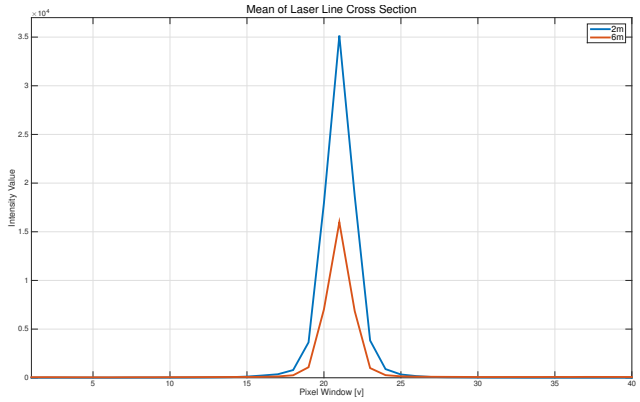

(a)

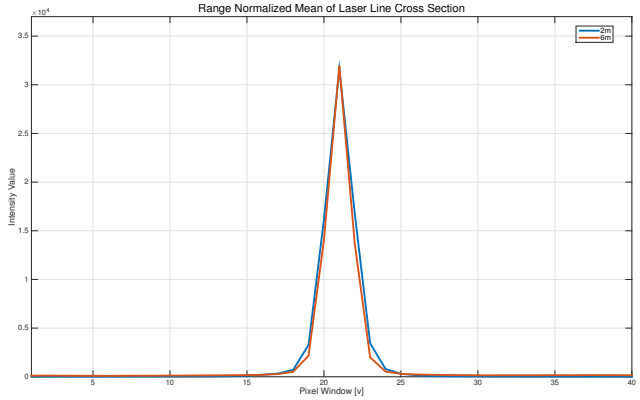

(b)

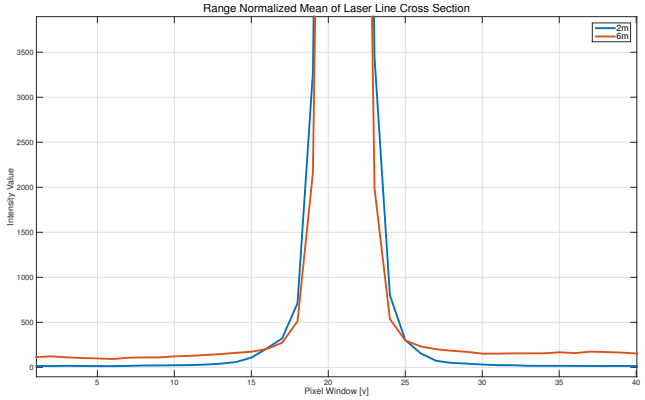

(c)

Figure 2.7: Mean of 680 laser line cross sections. (a) Without range normalization the 6m laser line has a lower intensity. (b) Range normalized intensities show 2m and 6m values are nearly equivalent. (c) Comparing the mean of the surrounding pixels indicates that the 6m data has a noise floor which is only slightly higher than 2m.

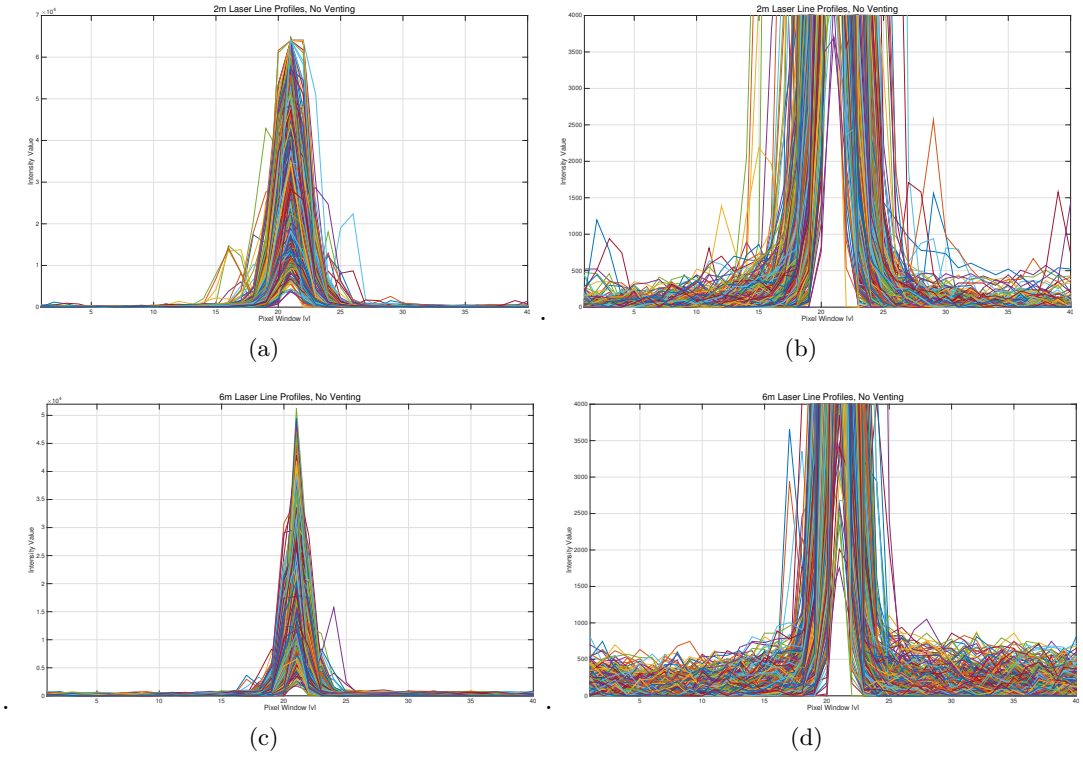

Figure 2.8: Aligned normalized laser line cross sections from within a single 2m and 6m image collected over the same area of non-venting seafloor. (a) Laser line profiles for 2m. (b) 2m data highlighting the intensity of the background (seafloor) pixels away from the laser peak. (c) Full laser line profiles from the 6m capture. (d) 6m data focused on the noise floor shown on the same scale as (b). The increase in noise floor intensity levels between 2m and 6m corresponds to an SNR increase of 0.5%. Therefore it is reasonable to say the SNR does not notably degrade up to an altitude of 6m.

fluid anomaly, Equation 2.1. This computation considers the intensity of each pixel falling within a specific window, w, about the peak of the laser line. To maintain a window with a constant distance on the seafloor from the laser line peak, the pixel size of the window must change with survey altitude. This is important for generating comparable vent detection results between surveys and is illustrated by the laser line cross sections presented in Figure 2.9. This image shows laser line cross sections for each altitude at the same non-venting and venting locations. Each cross section is comprised of 40 pixels indicated by red dots. The x-axis denotes distance from the center of the laser line in centimeters. Over plain seafloor it is notable that the width of the laser line is consistent, just under 0.5cm to either side of the laser line peak and is independent of range. Over active venting the width of the laser line varies more, for example, the laser line pixels in the 2m case will be mostly found within 1.25cm of the peak of the laser line while this distance increases to 2.5cm in the 6m case. However, over active venting the majority of the laser line blur is contained within approximately 1cm from the laser line peak, and defines the window in which the second moment should be considered. The number of pixels which make up this window varies with range, approximately 17 pixels at 2m, 11 pixels at 4m and 7 pixels at 6m. Implementing the second moment window dependent on distance from the laser line, instead of a fixed number of pixels, will produce vent detection results comparable between different survey altitudes.

The change in laser line width between areas with and without venting is also apparent when comparing laser line intensity values. One hundred aligned laser line intensity cross sections are shown in Figure 2.10. An undistorted crisp laser line covers approximately 3 pixels, independent of range, Figure 2.10(a-c). As the laser line passes over fluid density anomalies the overall intensity tends to decrease while the width of the laser line increases.

Establishing the correct window size will affect the second moment computation and vent detection results, which are presented as geo-spatial maps. As the window size decreases the computation becomes sensitive to variability in intensity within the data and increases the potential erroneously large moment values, creating false positives.

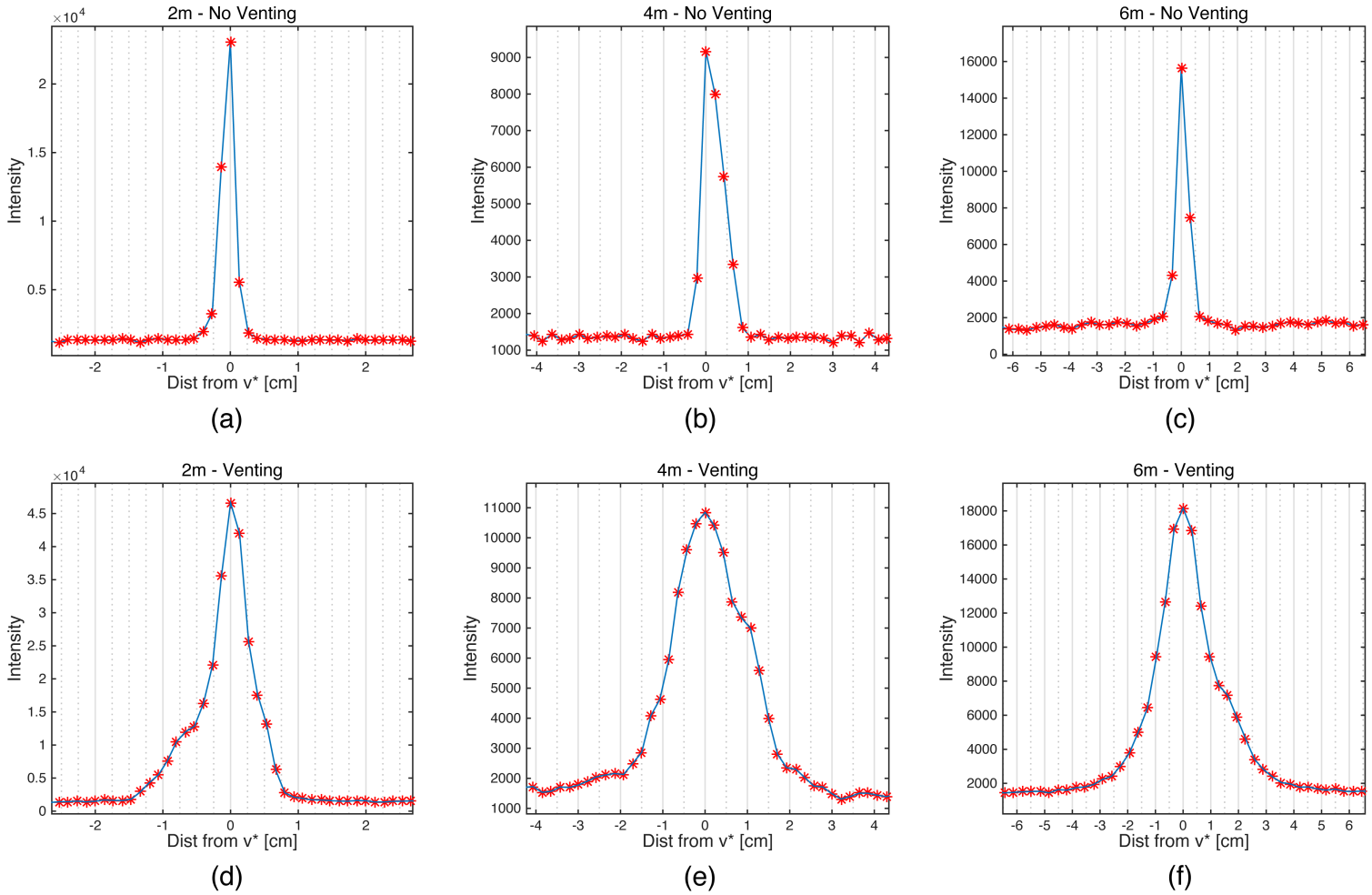

Figure 2.9: Comparison of laser line cross sections to illustrate the size of the second moment computation window w for each altitude. Each cross section is includes 20 pixels, represented by red dots, on each side of the peak intensity, v^*. The x-axis corresponds to the seafloor distance from the peak of the laser line in centimeters. Cross sections depicted in *a-c* correspond to data collected over an area without venting while the laser line in *d-f* are distorted due to active venting. (a& d) Correspond to 2m data with approximately 7.5pix/cm. (b& e) Correspond to 4m data with 4.7pix/cm. (c& f) Correspond to 6m data which has the lowest resolution with 3pix/cm.

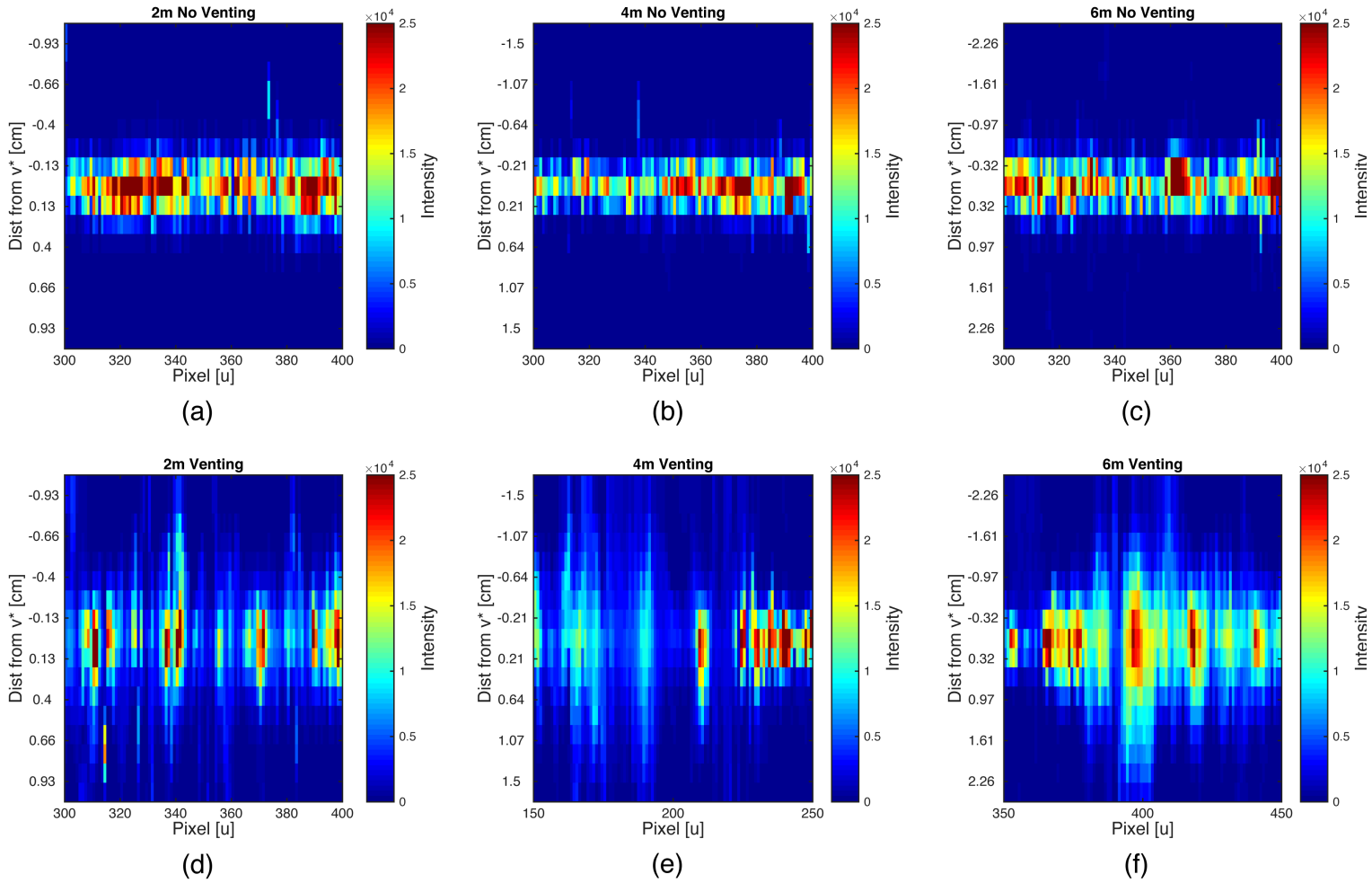

Figure 2.10: The pixels about the laser line illustrate the impact of range and the presense of venting on the laser intensity. Within each figure 20 pixels on each side of v^* are displayed, the 200 laser lines are aligned by v^*. (a-c) Correspond to images collected over areas without venting which show a crisp laser line consistently 3 pixels wide, independent of range. (d-f) Contain data collected over active vent sites where fluid interaction increases the laser line width.

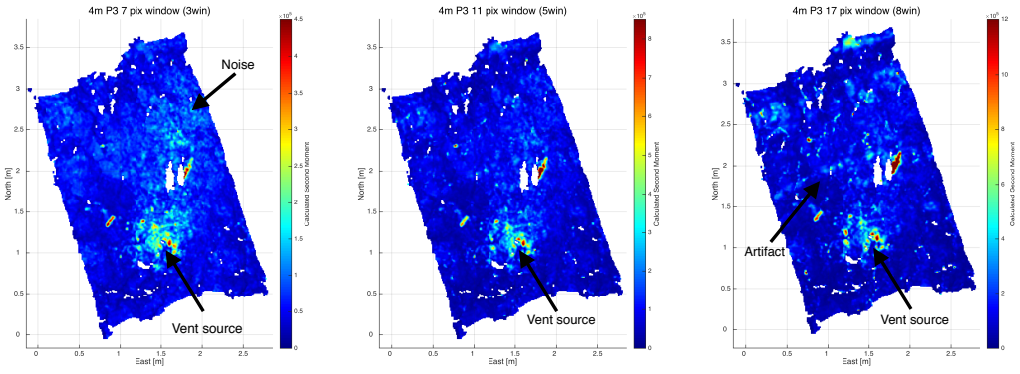

(a) (b) (c)

Figure 2.11: Gridded survey results comparing different windows for the second moment computation. (a) 1.2cm (7 pixel) window about v^* allows for slight anomalies to dominate, creating a noisy image. (b) 2cm (11 pixel) window allows for clear detection of the fluid anomaly. (c) 3.5cm (17 pixel) window is too large and allows background pixels to influence the computation.

Conversely, if a window is too large background pixels cause a lack of sensitivity resulting in a loss of detail. Figure 2.11 illustrates the impact of window size on the second moment computations, for data collected at an altitude of 4m. A 1.2cm (7 pixel) window about v^* is shown in Figure 2.11(a). This window is too small and is sensitive to slight fluctuations in the size of the laser line as indicated by the many bright spots within this image. Although this could be caused by fluid anomalies, the prevalence and distribution imply they are the result of changes in seafloor intensity or other scattering within the water column. Conversely, a 3.5cm (17 pixel) window shown in Figure 2.11(c) is large enough to include background seafloor not illuminated by the laser line. This can be further understood by looking at the 4m laser line cross sections shown in Figure 2.10. A window which is too large emphasizes seafloor characteristics, as observed by the detected spot along the northern edge of the survey and the horizontal artifact in the center of the survey. A balance between a window large enough to accommodate the increased laser line width in the presence of active venting but small enough to limit the role of non-illuminated background pixels is necessary. In this case a window 2cm wide (11 pixels) about v^*, Figure 2.11(b), meets this criteria. Fundamentally, as the pixel size increases with range each imaged laser pixel becomes less sensitive to small disturbances while covering a larger area of the seafloor.

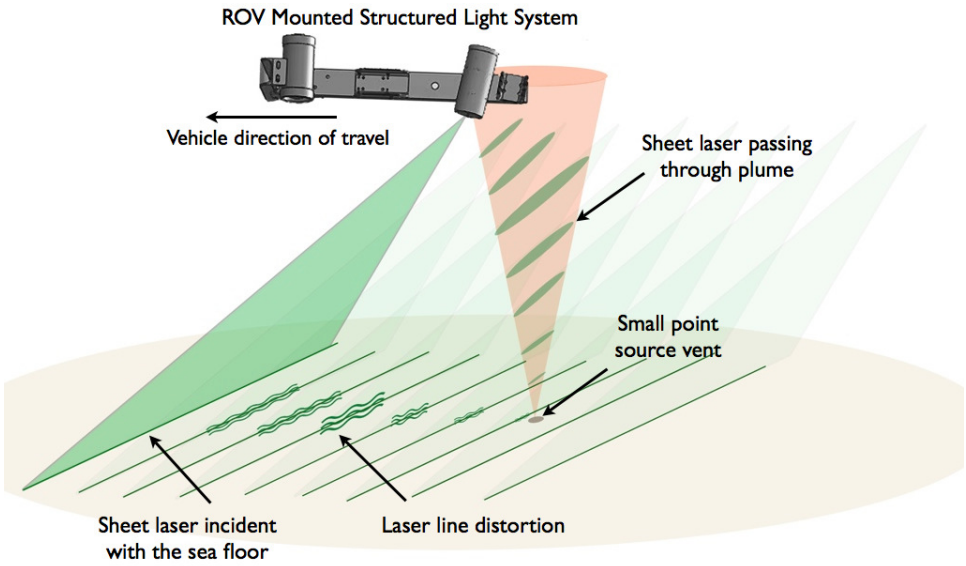

Figure 2.12: While surveying active vent sites the sheet laser passes through active turbulent flow of varying index of refraction values resulting in a blurred and distorted laser line projected on the seafloor.

2.6 Detection of Disturbances

The ability to detect fluid density anomalies using the structured light laser sensor at various altitudes is well established. However, when considering disturbances along the path of the sheet laser, which appear as laser line blur on the seafloor, more information can be gleaned regarding the structure of the active venting and associated plumes.

If the sheet laser interacts with the anomalous fluid meters above the seafloor the laser distortion will be projected beyond the vent, as a function of the laser sheet angle. As the vehicle travels past a vent the observed blur will continue until the fluid anomaly no longer intersects the laser plane, Figure 2.12. The along track distance the laser projects varies with altitude, as does the seafloor area under the sheet laser, Table 2.1. Practically, as these distances increase so does the potential for interaction with the laser sheet creating disturbances within the imaged laser line. Ideally, the geometry of the observed scattering could indicate the distribution and rise height of fluid flow.

Four passes labeled *Heading 1-4 (H1-4)*, at each altitude have been completed, Fig-

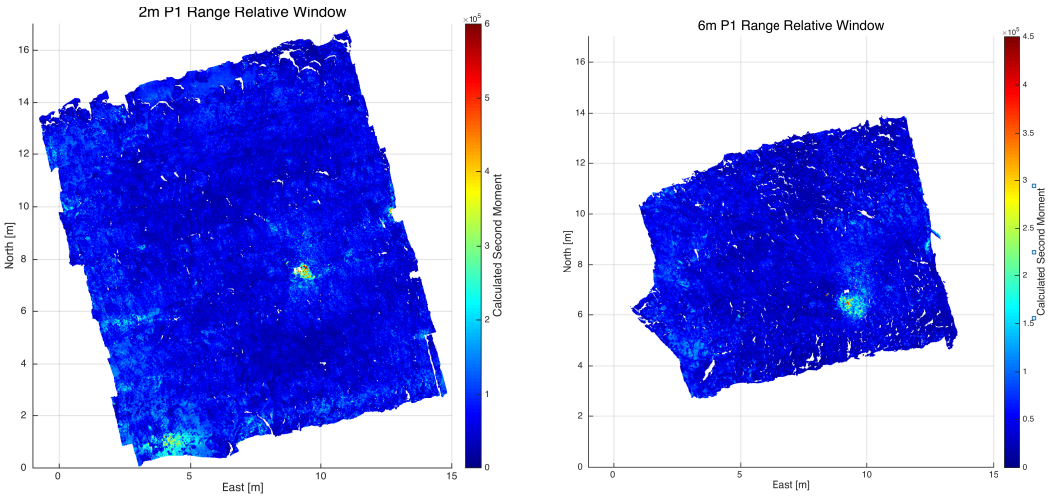

(a) (b)

Figure 2.13: An example of the gridded second moment results for the entire vent site. (a) Survey completed at 2m shows the area of active venting in the south east quadrant of the survey. (b) The survey completed at 6m requires fewer track lines and is lower resolution due to range, but the vent anomaly is visible in the same area.

ure 2.6, and will be used to compare differences in plume detection, sensitivity, resolution and shape. While vent detection results for the entire area surveyed at 2m and 6m are shown in Figure 2.13, further comparisons between surveys will be made based on segments of approximately 200 laser lines covering the area of active venting, Figure 2.16. Camera images acquired over the active vent site showing blur associated with fluid flow and the scientific markers are shown in Figure 2.14. Within the laser images occlusions due to these markers are visible as holes in the data. The occlusion is most notable in the data collected at 2m, as the percentage of the sheet laser blocked by the marker was highest. The association between laser line swath width and altitude is apparent as the survey patch width increases for higher altitudes.

2.6.1 Headings 1 and 3

Survey passes at *H1* and *H3* correspond to reciprocal laser line orientations over the vent and provide comparable illustrations of the laser line distortion. However, due to the forward angle of the projected laser sheet the majority of the distortion appears on the opposite side of the vent orifice.

Within the *H1* images the vent orifice appears as the strong increase in second

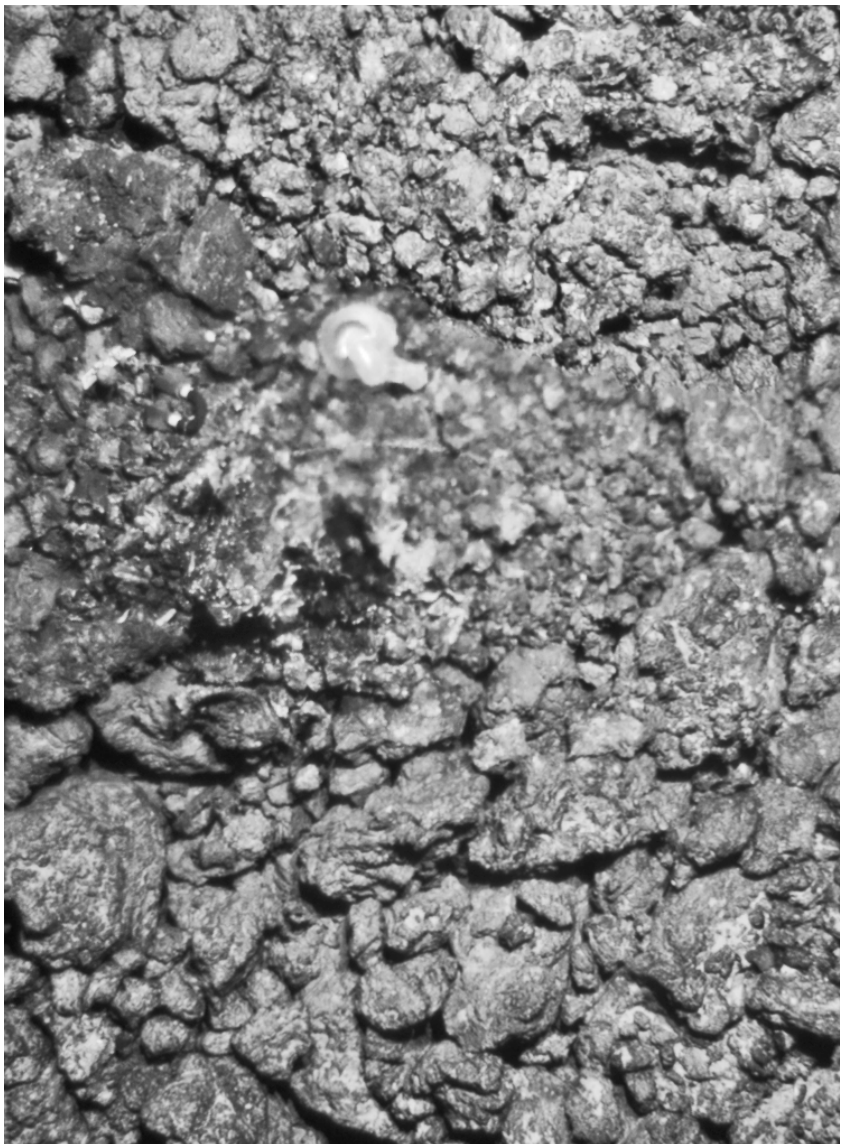

Figure 2.14: Merged images acquired by the mono camera during the 4m survey in which blur due to active venting of hydrothermal fluids and markers are present.

moment values located east of the marker occlusion in the 2m figure, slightly south in the 4m figure and nearly 0.5m south in the 6m case. Within the *H3* images the vent orifice is distinct and consistently located south of the marker occlusion.

While the across track width of the detected vent anomaly will be comparable for all *H1* and *H3* surveys, the length of the along track distortion will change as a function altitude. Within the presented results, this is generally true as the width of the distortion is between 0.75m and 1m, while the along track distortion length varies between 0.5m at the 2m altitude and 1m for 6m altitude. This distance represents the lateral distance where the rising vent fluid could intercept the laser plane. Once beyond the vent anomalous fluids no longer interact with the sheet laser and the captured laser line is crisp resulting in sharp border. This is apparent to the east of the anomaly in the 2m *H1* pass, Figure 2.15(a). The 2m and 4m surveys show experimental results which correlate to the projection distance shown in Table 2.1. However, the lateral distance under the sheet laser at a 6m altitude is 1.25m, which is significantly greater than the observed along track distortion length, implying the plume does not rise to 6m. Considering data from only this orientation, the fluid anomaly is either spreading 1m in the direction of vehicle travel or is rising a maximum of 4.5m and distorting the projected sheet laser. A combination of rise height and lateral effusion would explain the observed differences between survey altitudes.

2.6.2 Headings 2 and 4

Due to the vehicle heading, the shape of the detected laser blur is different in the perpendicular passes *H2* and *H4* and appears significantly wider across track and narrower along track. The observed distortion was split between adjacent overlapping survey lines in *H2* at 4m, (Figure 2.16(b)), and *H4* at 2m (Figure 2.16(d)) and 6m (Figure 2.16(f)). In these cases the marker occlusions are filled when the data from multiple passes are merged on a single plot.

Similar to the *H1* and *H3* case distortion is detected beyond the active vent depending on the direction of travel, south of the vent orifice in *H2* and north in *H4*. The

distance of this projection is consistently 0.5m along track and 1m across track. Additionally, the distortion pattern is fairly uniform in width and does not increase with distance from the orifice. This implies the density anomaly spreads at a fairly consistent altitude along the East-West direction, instead of rising directly into the water column. Considering the distortion is detected 0.5m from the vent orifice, the plume could be rising a maximum of 2.5m.

2.7 Discussion

This multi-altitude and multi-heading survey was acquired for the purpose of understanding the implications of survey altitude and heading on the detection of hydrothermal venting. While the key concepts are better understood, the impacts of survey altitude on signal quality, new questions have arisen.

2.7.1 Further Study

Given the robust laser line signal at the 6m altitude, signal limitations should be tested and established at higher survey altitudes. Eventually, due to attenuation and scattering, the laser will become too faint to detect. Additionally, the potential for non-vent related disturbances to the sheet laser due to water quality and biological activity to the will increase with range.

Survey limitations to consider at higher altitudes are the laser power and camera parameters. The current sensor suite is optimized to operate at an altitude of 3m, therefore the laser is low power (100mW) and a standard 12-bit computer vision camera is used. Increasing the power of the laser and using a camera better suited for low light applications will increase the laser line detection at increased survey altitudes. Additionally, increasing the resolution of the camera will allow for comparable resolution within the laser line captures.

The vent site studied within this paper included a relatively low flux, low temperature focused flow vent site with a plume which was not visibly detected more than a meter above the seafloor. Surveying a larger focused flow vent would provide additional insight into the possibility of determining rise height and the behavior of the plume us-

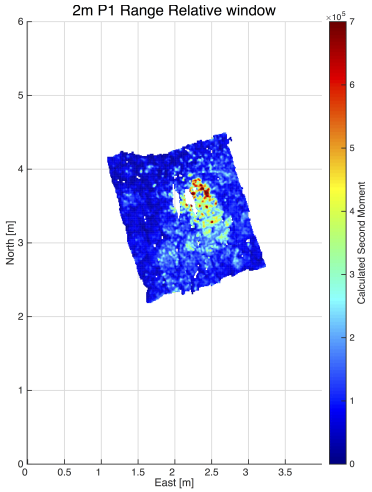

(a) 2m *H1*

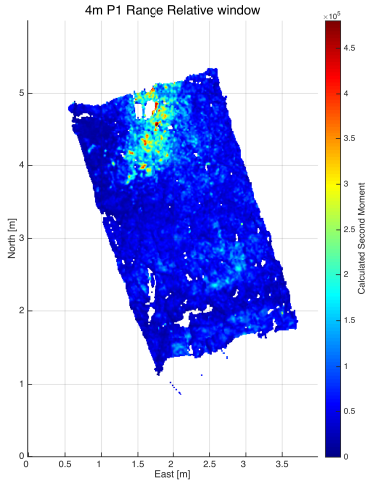

(b) 4m *H1*

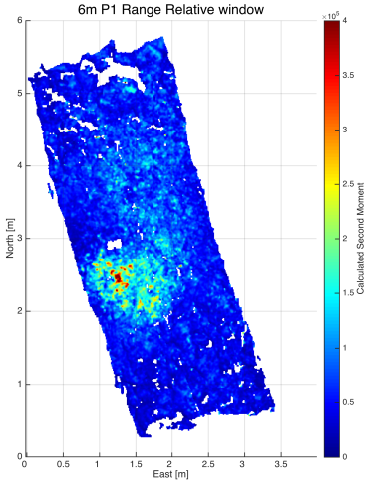

(c) 6m *H1*

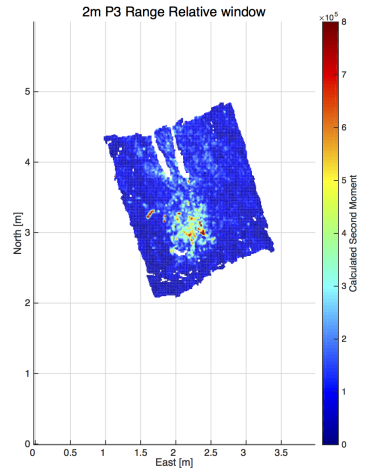

(d) 2m *H3*

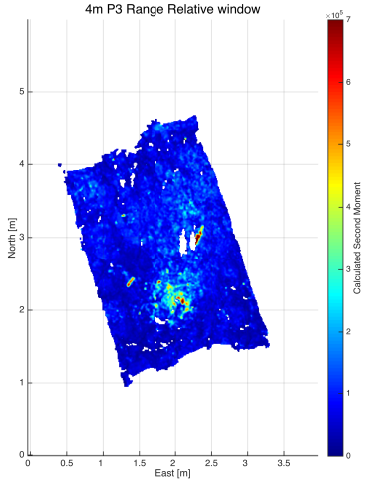

(e) 4m *H3*

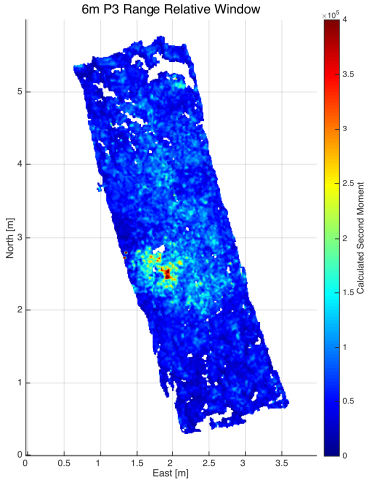

(f) 6m *H3*

Figure 2.15: Comparing survey results collected at reciprocal headings *Heading 1* and *Heading 3*. *Heading 1* is represented by (a-c), *Heading 3* is shown in (d-f).

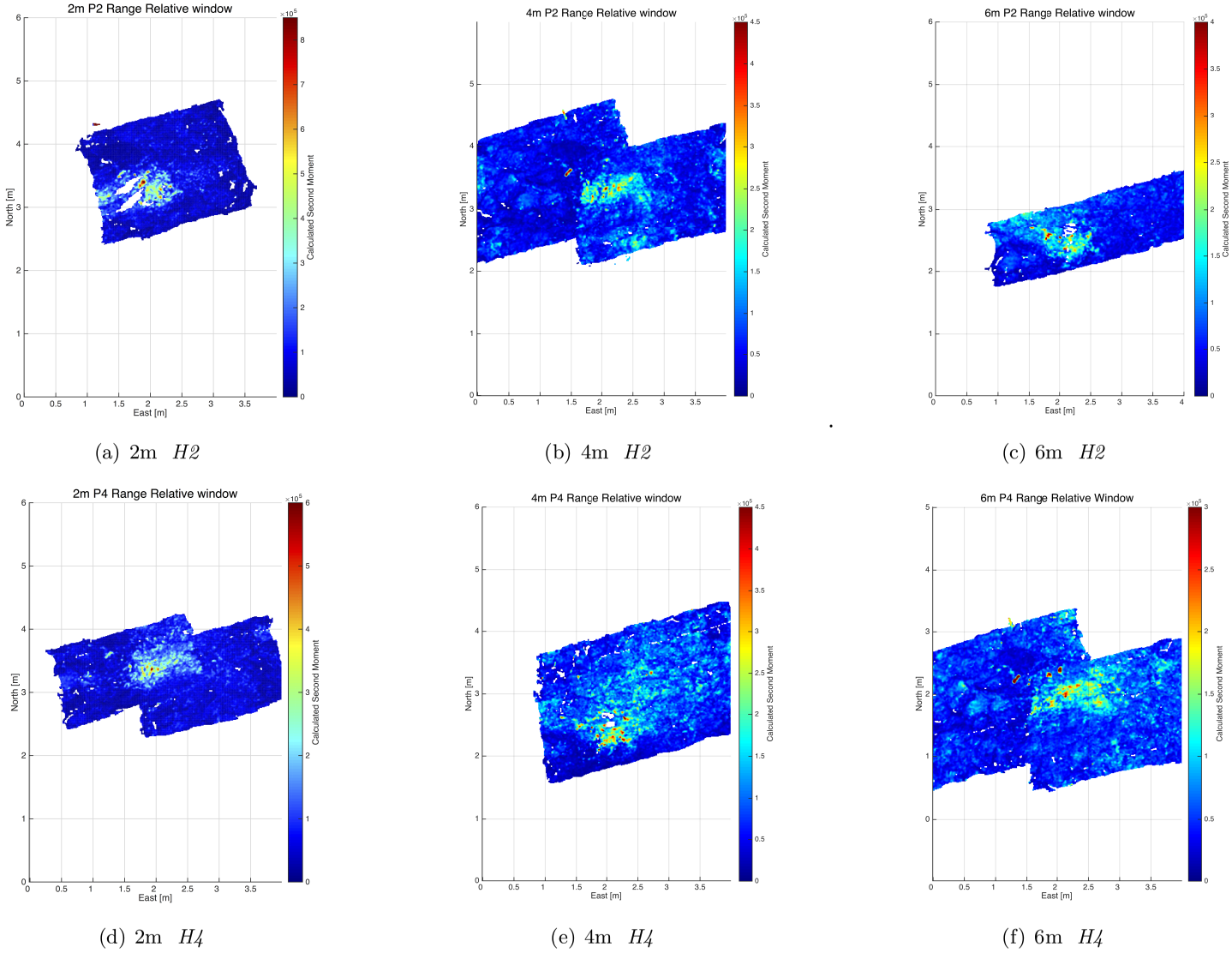

(a) 2m *H2* (b) 4m *H2* (c) 6m *H2*

(d) 2m *H4* (e) 4m *H4* (f) 6m *H4*

Figure 2.16: Comparing survey results collected at reciprocal headings *Heading 2* and *Heading 4*. *Heading 2* is represented by (a-c), *Heading 4* is shown in (d-f).

ing the pattern of the laser line on the seafloor as outlined in Section 3.1 and shown in Figure 2.12. Although slightly tedious, the multiple survey orientations and altitudes demonstrate that it is possible to glean information about the disturbance in the water column. This is encouraging, as it may lend itself to further quantification of volume or heat flux rates.

2.8 Conclusion

Varying survey altitudes alters the resolution and intensity of the imaged laser line but does not obscure detection of fluid anomalies if processing parameters are adjusted to account for changes in range. The direction of the sheet lasers projection can indicate properties of the associated hydrothermal plumes and distribution of fluid anomalies. The presented results are promising considering the aim of operating of this sensor at higher altitudes from an autonomous underwater vehicle as a part of general site mapping.

List of References

[1] C. J. Smart, C. Roman, and S. N. Carey, "Detection of diffuse seafloor venting using structured light imaging," *Geochemistry, Geophysics, Geosystems*, vol. 14, no. 11, pp. 4743–4757, 2013. [Online]. Available: http://dx.doi.org/10.1002/ggge.20280

[2] C. R. German, D. R. Yoerger, M. Jakuba, T. M. Shank, C. H. Langmuir, and K. Nakamura, "Hydrothermal exploration with the autonomous benthic explorer," *Deep-Sea Research Part I: Oceanographic Research Papers*, vol. 55, no. 2, pp. 203–219, 2008.

[3] D. R. Yoerger, A. M. Bradley, M. V. Jakuba, C. R. German, T. M. Shank, and M. A. Tivey, "Autonomous and remotely operated vehicle technology for hydrothermal vent discovery, exploration, and sampling," *Oceanography*, vol. 20, no. 1, pp. 152–161, 2007.

[4] C. Roman, G. Inglis, and J. Rutter, "Application of structured light imaging for high resolution mapping of underwater archaeological sites," in *IEEE Oceans, 2010. Proceedings on*, 2010.

[5] G. Inglis, C. Smart, J. Vaughn, and C. Roman, "A pipeline for structured light bathymetric mapping," in *Intelligent Robots and Systems, Proceedings. October 7-12, IEEE/RSJ International Conference on*, 2012.

[6] N. Otsu, "A threshold selection method from gray-level histograms," *IEEE Transactions on Systems, Man, and Cybernetics*, vol. 9, no. 1, pp. 62–66, Jan 1979.

[7] D. P. Connelly, J. T. Copley, B. J. Murton, K. Stansfield, P. A. Tyler, C. R. German, C. L. Van Dover, D. Amon, M. Furlong, N. Grindlay, N. Hayman, V. Huhnerbach, M. Judge, T. Le Bas, S. McPhail, A. Meier, K.-i. Nakamura, V. Nye, M. Pebody, R. B. Pedersen, S. Plouviez, C. Sands, R. C. Searle, P. Stevenson, S. Taws, and S. Wilcox, "Hydrothermal vent fields and chemosynthetic biota on the world's deepest seafloor spreading centre," *Nat Commun*, vol. 3, p. 620, 01 2012. [Online]. Available: http://dx.doi.org/10.1038/ncomms1636

[8] JAMSTEC, "R/v yokosuka & dsv shinkai 6500 cruise report yk13-05: Geochemical, geomicrobiological and biogeographical investigation of deep-sea hydrothermal activities in the mid cayman ridge, the caribbean," Japan Agency for Marine-Earth Science and Technology (JAMSTEC)," Cruise Report, 2013.

[9] "New frontiers in ocean exploration: The e/v nautilus and noaa ship okeanos explorer 2015 field season," *Oceanography*, vol. 29, no. 1, p. 84, Supplement 2016.

[10] J. C. Kinsey and L. L. Whitcomb, "Preliminary field experience with the dvlnav integrated navigation system for oceanographic submersibles," *Control Engineering Practice*, vol. 12, pp. 1541–1549, 2004.

[11] R. C. Smith and K. S. Baker, "Optical properties of the clearest natural waters (200–800 nm)," *Appl. Opt.*, vol. 20, no. 2, pp. 177–184, Jan 1981. [Online]. Available: http://ao.osa.org/abstract.cfm?URI=ao-20-2-177

MANUSCRIPT 3

Remote Detection of Density Anomalies Within Gulf of Mexico Brine Pools using a High Resolution Multibeam Sonar System

by

Clara J. Smart [1], Chris N. Roman[2], Anna Michel [3] Scott Wankel [4]

In preparation for submission to Deep-Sea Research Part I: Oceanographic Research Papers

[1]Ph.D. Candidate, Department of Ocean Engineering, The University of Rhode Island, Narragansett RI 02882. Email: csmart@my.uri.com

[2]Asst. Prof of Oceanography, Graduate School of Oceanography/Department of Ocean Engineering, The University of Rhode Island, Narragansett RI 02882. Email: cnr@gso.uri.edu

[3]Assistant Scientist, Applied Ocean Physics & Engineering, Woods Hole Oceanographic Institution, Woods Hole, MA 02543

[4]Associate Scientist, Marine Chemistry & Geochemistry, Woods Hole Oceanographic Institution, Woods Hole, MA 02543

Abstract

The ability to remotely map density anomalies, including stratification and rising bubbles within a brine pool contributes to a comprehensive understanding of the internal characteristics, leading to better informed sampling efforts. Remote and systematic surveys are completed using a high resolution ROV-mounted camera system and a 1350kHz multibeam sonar system. Acoustic water column data collected over the brine pool are then analyzed for multiple acoustic returns caused by internal density stratification and bubbling seeps. Density variations are confirmed by in-situ measurements collected using a reel-mounted conductivity, temperature, and depth (CTD) sensor. Compilation of these results allows for a depiction of the internal brine pool structure.

3.1 Introduction

Systematic bathymetric imaging of deep-sea geologic features using acoustic and optical sensors mounted on underwater vehicles is common [1–3]. Sampling and imaging efforts at brine pools traditionally focus on the surrounding biology, geologic features, and collect fluid samples, but do not systematically establish a spatial understanding of fluid characteristics within the brine pool. The presented study implements established high resolution mapping techniques to determine brine pool surface properties and internal density stratification. An improved understanding of brine pool structure will allow for better informed discrete sampling and provide insight into geologic and cold seep dynamics through temporal surveys.

The remainder of the introduction will cover the brine pool field sites and the high resolution mapping system. Section 3.2 will discuss the geologic background and outline previous sampling and imaging efforts. The mapping procedures will be introduced in Section 3.3 before presenting and interpreting the results in Sections 3.4 and 3.5.

3.1.1 Geologic Setting of Gulf of Mexico Brine Pools

Tectonic activity within the Louann Salt formation, which developed during the Jurassic period has created faults and salt diapir structures within the northern Gulf of Mexico [4]. Seeps associated with trapped hydrocarbon deposits rise to the seafloor where

expulsion of hydrocarbon gas can create craters and pockmarks that can become filled with hypersaline fluid, due to underlying salt deposits, creating brine pools and basins [5–9]. These features are apparent through the presence of active mud volcanoes and salt diapirs identified using sub-bottom acoustic mapping techniques [10–12]. Multiple types of basins and troughs likely to host hypersaline solutions are outlined in [9].

While hypersaline fluid within pockmarks and basins is thought to be common, few brine lakes, rivers, and pools are well studied [8, 13, 14]. Bubbles associated with active methane seeps, which can be detected acoustically in the water column, indicate gas seepage [15] which in combination with crater like structures signify potential brine pool locations [7]. Brine pools in the Gulf of Mexico can vary widely in size ranging from the small pools with surface areas on the order of $10m^2$ which were discovered near the brine river GB 903 [16] to the $400km^2$ and 200m deep Orca Basin [17, 18]. In some instances the brine interface is distinct enough to be detected by seismic or shipboard multibeam systems, while other sites have been located visually using remotely operated vehicle (ROV) systems [18].

GC233 and San Jac Brine Pools, Gulf of Mexico

Data resulting from the acoustic surveys at two Gulf of Mexico brine pools, GC233 and San Jac Brine Pool (SJBP) form the basis for this study. Located in Green Canyon 233 lease block the GC233 Brine Pool (also identified as Brine Pool NR1) was discovered in 1989 and has since been well studied [13]. This brine pool fills an approximately 12m by 20m crater located at depth of 650m in the northern Gulf of Mexico. ROV *Hercules* operated from E/V *Nautilus* visited GC233 in July 2014 (Cruise ID NA045). While collecting biological samples of the dense mussels beds surrounding the brine pool was the primary goal the science team took the opportunity to survey the stie.

Analysis of the acoustic mapping data acquired at GC233 led to the more detailed imaging and sampling work completed at San Jac Brine Pool (SJBP) which is at a depth of 1320m on the northwestern continental shelf of the Gulf of Mexico, Figure 3.1. It is located within the East Breaks region, north of San Jacinto Mound and south of Flawn

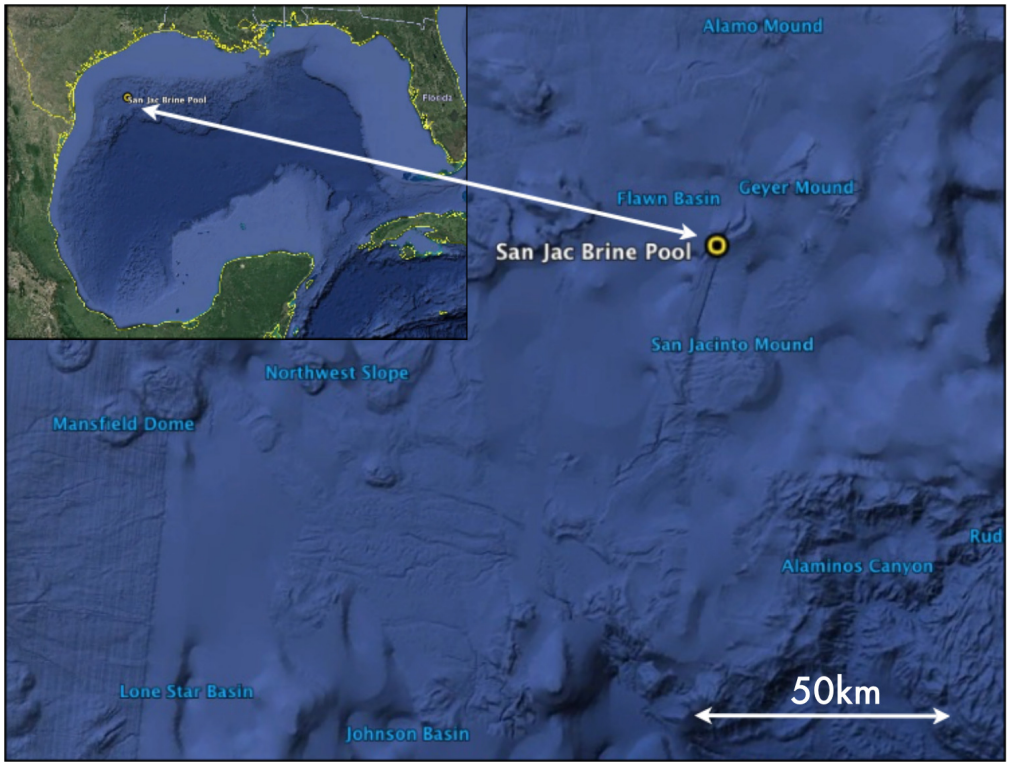

Figure 3.1: The San Jac Brine Pool is located on the Northwest continental shelf of Gulf of Mexico in the East Breaks, north of San Jacinto Mound and south of Flawn Basin.

Basin as defined by [14]. SJBP is within a 30m diameter circular crater which rises 3m above the surrounding seafloor, Figure 3.2(b). A vigorous stream of methane bubbles was detected using the Kongsberg EM302 hull-mounted multibeam sonar system on *E/V Nautilus* in 2013. A subsequent multibeam survey using the autonomous underwater vehicle (AUV) *Sentry* flying at an altitude of 30m reveled a distinct crater. The brine pool with methane bubbles emanating from the center was then confirmed by the ROV *Hercules* while conducting visual exploration using high definition cameras. Biological activity surrounds the edges (Figures 3.2(b) & 3.2(c)) and a cluster of smaller 'tide pools' are located along the northern edge (Figure 3.2(d)).

E/V *Nautilus* and ROV *Hercules* returned to San Jac Brine Pool May 16-18, 2015 for extensive high resolution mapping and sampling work (Cruise ID NA059). Objectives at the brine pool included collecting high resolution stereo and acoustic imaging data, conductivity temperature and depth (CTD) measurements, geochemical information using laser spectroscopy, water collection, and biological samples [16]. Correlation between this acoustic mapping and CTD data provides the basis for this paper.

3.1.2 High Resolution Mapping Suite

Data for sub-centimeter bathymetric and photographic maps are collected with a suite of high resolution imaging sensors mounted on the ROV *Hercules*, Figure 3.3 [19]. The primary sensor applied to this study is the 1350kHz BlueView Technologies MB1350-90 multibeam sonar system which has a 90° field of view and operates at altitudes between 2m - 15m. Optical imaging is completed using a stereo pair of 12-bit 1360 x 1024 pixel Prosilica GC1380 computer vision cameras, one color and one mono, each with a 30° x 40° field of view. Additionally, the imaging suite includes a structured light laser sensor comprised of a 12-bit mono Prosilica GC1380 camera and a verged Coherent Powerline 100mW, 532nm sheet laser. The structured light laser is used for collecting intensity and bathymetry data, and identifying fluid density anomalies near the seafloor [20, 21]. This imaging suite has been extensively used for high resolution mapping of geological, archaeological, and biological sites [19]. All imaging data are

(a)

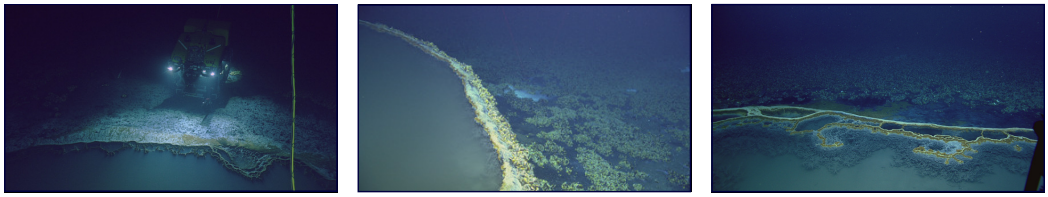

(b) (c) (d)

Figure 3.2: Images of the San Jac Brine Pool taken with the remotely operated vehicles. (a) ROV *Hercules* surveying the steep edge of the brine pool which rises 3m above the seafloor. (b) ROV *Hercules* illuminating the brine interface. (c) The thin edge of the brine pool with bacteria and mussels. (d) Small 'tide pools' at the northern edge of the brine pool.

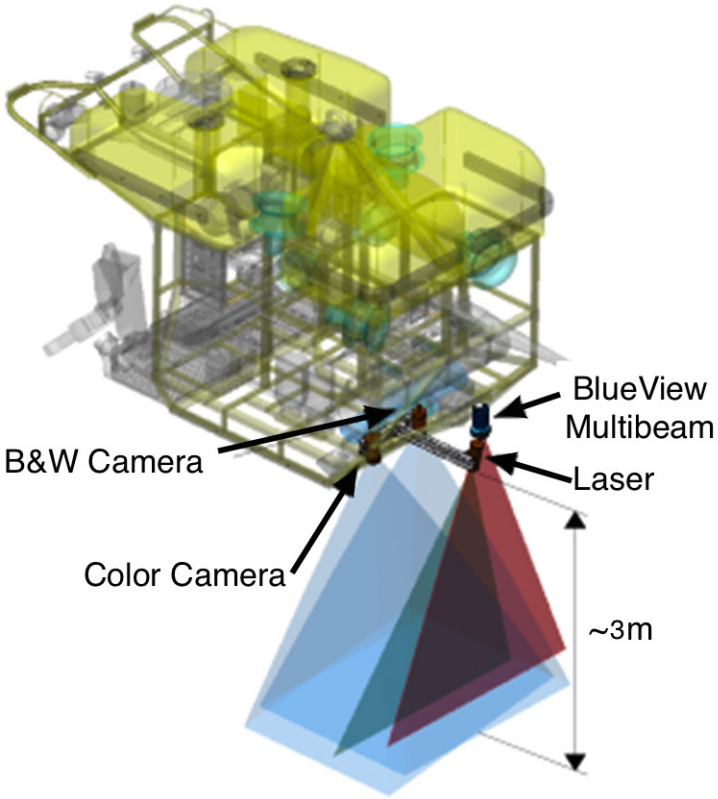

Figure 3.3: A CAD rendering of ROV *Hercules* with the standard imaging suite which includes a stereo camera pair, structured light laser sensor and 1350kHz multibeam sonar.

collected simultaneously and therefore co-registered. The closed loop controlled 4000m -rated *Hercules* ROV has an advanced navigation sensor suite which includes an RDI Doppler Velocity Log (DVL), IXSEA OCTANS fiber-optic gyroscope and a Paroscientific depth sensor [22].

3.2 Background

3.2.1 Brine Pool Discovery, Exploration and Sampling Techniques

Unlike the relatively massive and well studied brine pools of the Red Sea, such as the Atlantis II Deep which was discovered and analyzed through CTD and tow-yo casts [23, 24], those in the Gulf of Mexico are small, existing in troughs and craters in the seafloor [7]. Brine pool discoveries within the Gulf of Mexico have been made by analyzing detailed seismic survey data for anomalies and hyperbolic reflectors [13, 18] or

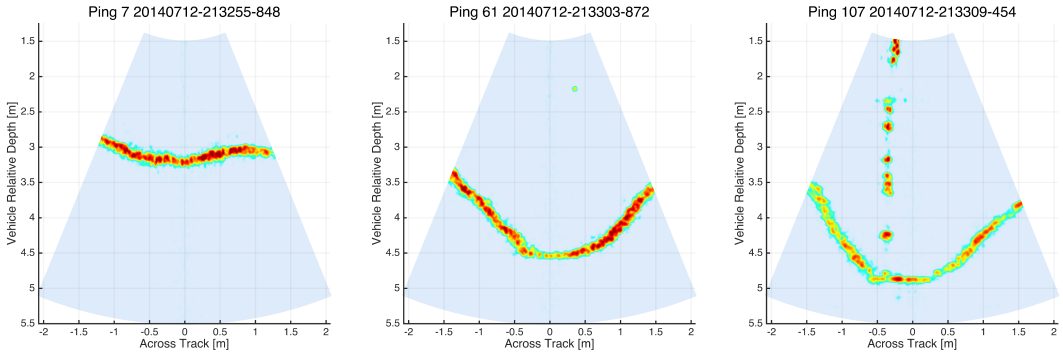

(a) (b) (c)

Figure 3.4: Sample multibeam water column data collected at GC233 in 2014 from 3m above the surface of the brine pool. (a) The acoustic reflection off the surface interface. (b) An example of the multibeam breaking through the surface and reflecting off either an internal density layer or the seafloor. (c) Bubbles detected within the brine pool, below the surface interface.

by detecting echo-free patches in sidescan data as demonstrated on the Mediterranean Ridge [25]. Verification of brine pools at these sites requires deploying a deep sea vehicle.

Imaging approaches, including ROV or human occupied vehicle (HOV) mounted video cameras, acoustic and optical sensors are used to create site maps to guide scientific sampling. In the case of the GC233 Brine Pool a 25kHz subbottom profile established the underlying mud volcano structure [13, 26]. A high resolution backscatter imaging survey was completed upon discovery in May 1989 using a laser line scanner mounted on the NR-1 submarine [27]. More recently photomosaics and multibeam maps with high resolution details have furthered understanding of structural characteristics and surrounding biologic activity [16].

Well studied brine pools in the Gulf of Mexico have been visited multiple times over the course of decades and have included biologic, hydrographic, and geochemical sampling efforts. For instance, discrete sampling using CTD casts and a 'brine-trapper' established the temporal stability of GC233 [8] while lead line casts helped determine the depth [26]. More technologically advanced sampling methods include conducting in-situ chemical analysis of the fluid by deploying a mass spectrometer and laser spectrometer [16, 28] These discrete data points are then interpolated in an effort to understand the characteristics of a brine pool.

3.2.2 2014 Mapping of Brine Pool GC233

During the 2014 acoustic survey of GC233 completed using ROV *Hercules* multiple and varying acoustic returns were observed within the multibeam water column data indicating non-uniformity in the acoustic impedance of the brine-seawater interface, Figure 3.4. While distinct acoustic returns from the surface at the southern end of the pool were observed (Figure 3.4(a)), the returns from the northern surface appeared to 'break through' without reflecting off the interface (Figure 3.4(b)). Additionally, rising bubbles were observed within the multibeam water column data as the vehicle surveyed the northern areas, Figure 3.4(c). High resolution multibeam bathymetry results from within the brine pool shown in Figure 3.5 indicate the dominate acoustic returns varied in depth, likely due to variations in acoustic impedance. With limited sensors, temperature data from three surface points was gathered to confirm a surface temperature differential. While the ambient seawater temperature was 7°C, the surface along the southern region of the brine pool recorded 8.06°C while surface temperatures at two distinct points within the northern region were 9.2°C and 8.83°C, Figure 3.5. A similar acoustic phenomenon due to density interfaces was briefly noted by McDonald in 1990 while analyzing 25kHz acoustic subbottom data collected at GC233 [26].

This 2013 mapping effort indicating detection of brine pool density anomalies using the high frequency multibeam provided the impetus to conduct mapping surveys with accompanying CTD and geochemical data at the San Jac Brine Pool in 2015, as outlined within this study.

3.2.3 Acoustic Mapping Techniques

Acoustic mapping systems are sensitive to differentials in acoustic impedance, the product of density and sound speed ($z = \rho c$). Typically the dominant acoustic reflection corresponds to a significant impedance differential between seawater and the seafloor. However, the density increase associated with the hypersaline surface of a brine pool can reflect, or partially reflect, the acoustic ping. For instance, at Orca Basin a high resolution 3-D sub-bottom system detected the brine pool surface and the underlying

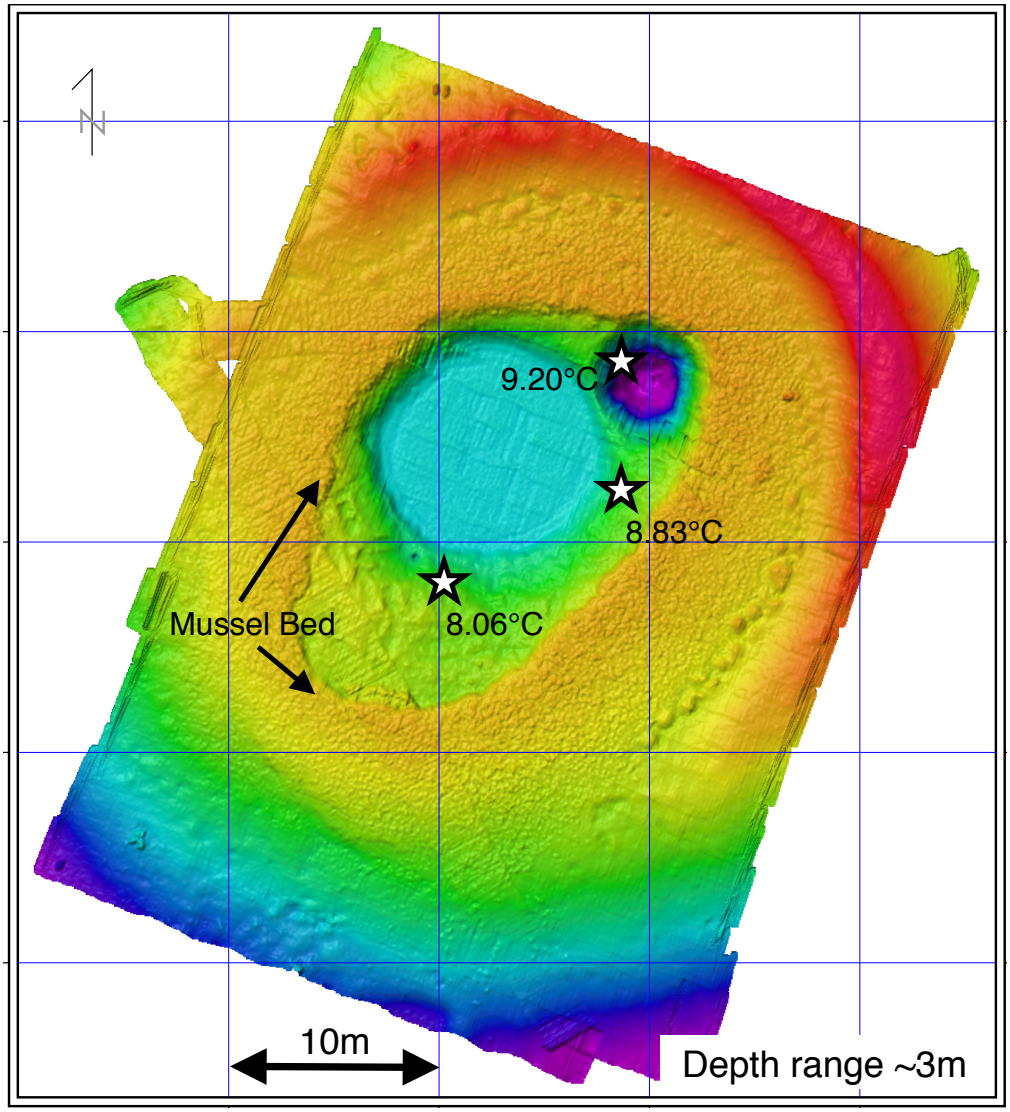

Figure 3.5: The resulting 2014 high resolution multibeam bathymetry map of the GC233 Brine Pool. The light orange areas are the mussels along the rim providing an indication of the boundary of the brine pool. The brine surface is flat, therefore blue, green and purple areas within the brine pool reveal changing acoustic impedance associated with reflections off of the seafloor or density stratified layers. The bathymetric depth range is approximately 3m. Surface temperatures at three specific locations are indicated, ambient seawater is 7°C.

seafloor allowing for volumetric estimates [18]. Similarly, acoustic pings propagating through the pool's surface may be reflected by a fluid density interface or the seafloor [29]. The high frequency (1350kHz) of the selected multibeam system makes it sensitive to relatively small acoustic impedance differentials. Gas filled bubbles rising from the seafloor can also be detected by a sonar system as the acoustic impedance for air is much less than the surrounding seawater [15].

3.2.4 Density Analysis at High Temperature and High Salinity

Thermodynamic equations of seawater introduced in 2010 [30] to compute seawater properties such as density and sound speed do not apply to hypersaline fluids. The practical salinity range is $2 < Sp < 42$ while the temperature range is $-6°\text{C} < t < 40°\text{C}$. By nature brine pools have salinity values which exceed these bounds, for example salinity values at GC233 reach 120PSU [8, 26]. Computations for salinity values up to 70g/kg and temperatures to 90°C are presented by [31]. Using values outside this range will impact the accuracy of computed salinity values from conductivity, density and sound speed for brine pools.

3.3 Methods

3.3.1 2015 Survey Methodology

High resolution imaging of the San Jac Brine Pool was completed in 2015 using the imaging suite outlined in Section 3.1.2. The stereo cameras, structured light laser sensor and multibeam sonar were operated simultaneously. The closed loop control system and 600kHz Doppler Velocity Log (DVL) sensor allowed the ROV to survey in a mowing the lawn pattern at a fixed depth, corresponding to an altitude of 3m above the surface of the brine pool, and a velocity of 0.18m/s. However, the DVL was unable to attain reliable readings over the entire surface of the brine pool due to the low differential in acoustic impedance. Therefore, during the survey ROV *Hercules* was flown manually for short sections causing occasional inconsistencies in the line spacing and overlap. The along track image overlap and across track sensor overlap was between $20 - 30\%$ and the multibeam ping rate was set to 10Hz.

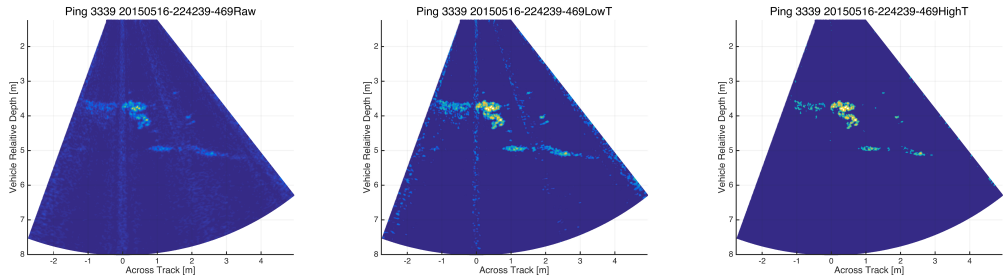

(a) Raw Image (b) Low Threshold (c) High Threshold

Figure 3.6: Processing of the multibeam data includes thresholding the logarithmically scaled water column image, the acoustic response from the mass of water below the sonar sensor, to remove associated noise without impacting the faint acoustic returns associated with the brine pool. (a) Raw multibeam water column image. (b) An image processed using a low threshold. (c) An image with higher threshold applied which although reduces noise can eliminate signal.

The time on site to accomplish all scientific and exploration objectives, including collecting the presented data, was limited to two ROV dives totaling 33 hours with a 12 hour turn around, allowing minimal time for on site data analysis. Additional sampling efforts are outlined in [16].

3.3.2 Analysis of Multibeam Data

Rather than analyze the multibeam seafloor bathymetry, derived from the dominant acoustic response, this study will focus on water column images which depict the interaction between the propagating acoustic ping and the brine fluid directly under the multibeam sensor, Figures 3.4 and 3.6. This analysis allows for the detection of multiple acoustic returns associated with several density anomalies within the brine pool.

Each multibeam ping must be converted into a single water column image, Figure 3.6(a). As significant sensor noise in the raw image makes differentiating faint acoustic returns difficult the image intensity is mapped to a logarithmic scale, normalized, and thresholded. A successful threshold eliminates sensor noise without negatively impacting the acoustic signals of interest. Examples of varying thresholds are shown in Figures 3.6(b) and 3.6(c). Multiple acoustic returns indicating density stratification and bubbles become apparent during examination of the resulting images. Faint returns from the surface interface likely were below the threshold and eliminated, for example no surface

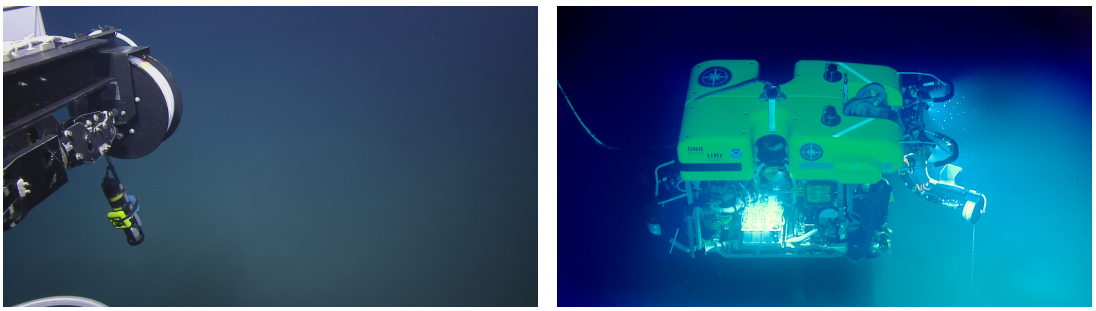

(a) (b)

Figure 3.7: A battery operated, internal logging RBRconcerto CTD calibrated for temperature and salinity levels associated with the brine pool. (a) The CTD was attached to a reel mechanism and secured to the manipulator arm of the ROV *Hercules*. (b) Lowering of the CTD into the San Jac Brine Pool while collecting data.

interface is visible in the water column images with bubbles.

During this survey the array corresponding to the left quarter of the sonar sector malfunctioned returning no data. The three additional arrays functioned properly, therefore the presented data covers a 67.5° field of view instead of the expected 90°. This narrow footprint was accounted for during the survey and precautions regarding across track overlap were taken.

3.3.3 Conductivity, Temperature and Depth Data Collection

In an effort to make conclusive statements about the multibeam results, temperature and salinity measurements at specific depths within the brine pool were gathered using an RBRconcerto CTD sensor. This battery operated sensor with on-board logging capabilities was connected to a reel mechanism and mounted on *ROV Hercules*, Figure 3.7. The sensor was non-buoyant and the reel line was marked at 1m increments to provide preliminary in-situ depth information. The design allowed the line to become slack when the CTD reached the seafloor. The CTD samples at 1Hz and includes an inductive conductivity sensor, a theromistor, and a piezo-resistive transducer with nickel based super alloy diaphragm for pressure measurements. Due to the anticipated high salinity and high temperature environment of the brine pool the CTD was calibrated for temperatures between -5 – 50°C, conductivity values between $0 - 145\text{m}S/\text{cm}$ and across a depth range of 10 – 2000m.

As the data were not accessible in real time it was not possible to know when a reading had achieved steady state. Therefore transitions between density layers can show significant overshoot and long settling times, particularly in the conductivity data which is translated to salinity as outlined in Section 3.2.4. Additionally this CTD uses an inductive conductivity sensor, which requires fluid to flow across the sensor, and may be impacted by suspended sediment within the brine pool.

Locations for each CTD cast were determined using the ROV-tracking ultra-short baseline system (USBL) which uses transponders mounted on the ROV and ship, and is not impacted by the acoustic anomalies associated with the brine pool.

3.4 Results

The high resolution imaging suite (Section 3.1.2) completed a 40m x 35m (1400m^2) survey of the San Jac Brine Pool and CTD casts were conducted at seven locations to provide ground truth data for acoustically observed density anomalies.

3.4.1 High Resolution Mapping of the Brine Pool

A comprehensive visual representation of the site is shown in the resulting photo-mosaic in Figure 3.8. This mosaic consists of approximately 2000 color images and was created using a variation of the software discussed in [32]. Within this image discoloration due to high salinity and biological activity is visible around the rim of the pool and on the northern slope. The small 'tide pool' like features, also shown in Figure 3.2(d), are visible on the northern side of the crater.

A gridded structured light laser intensity, or backscatter, map used to geo-reference CTD casts and multibeam pings is shown in Figure 3.11. The laser light does not reflect off the brine interface unlike the hard substrate which becomes well defined. Additionally, this image provides insight into the seafloor characteristics surrounding the brine pool as sediment types and biological material have varying albedo.

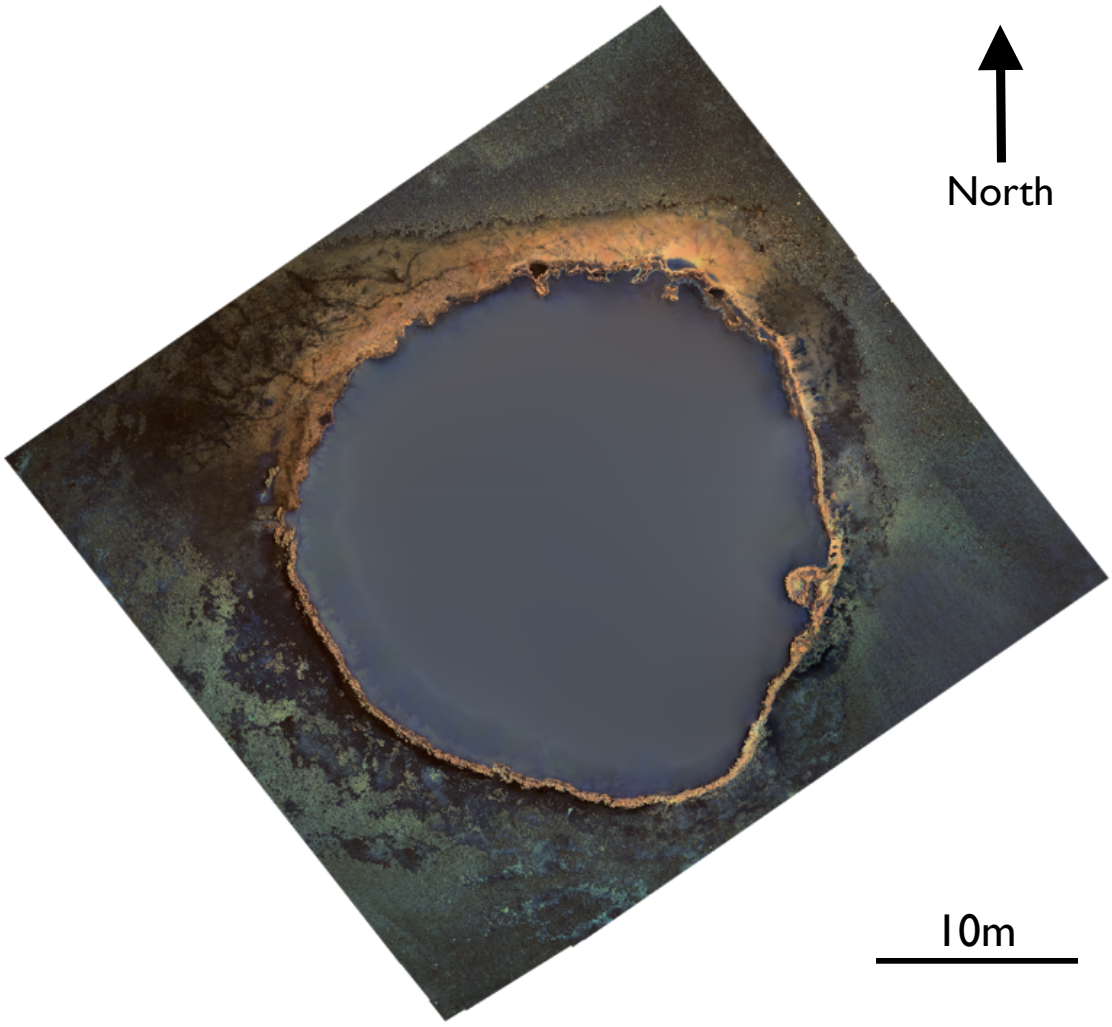

Figure 3.8: Photomosaic of the San Jac Brine Pool, Gulf of Mexico is comprised of approximately 2000 color images.

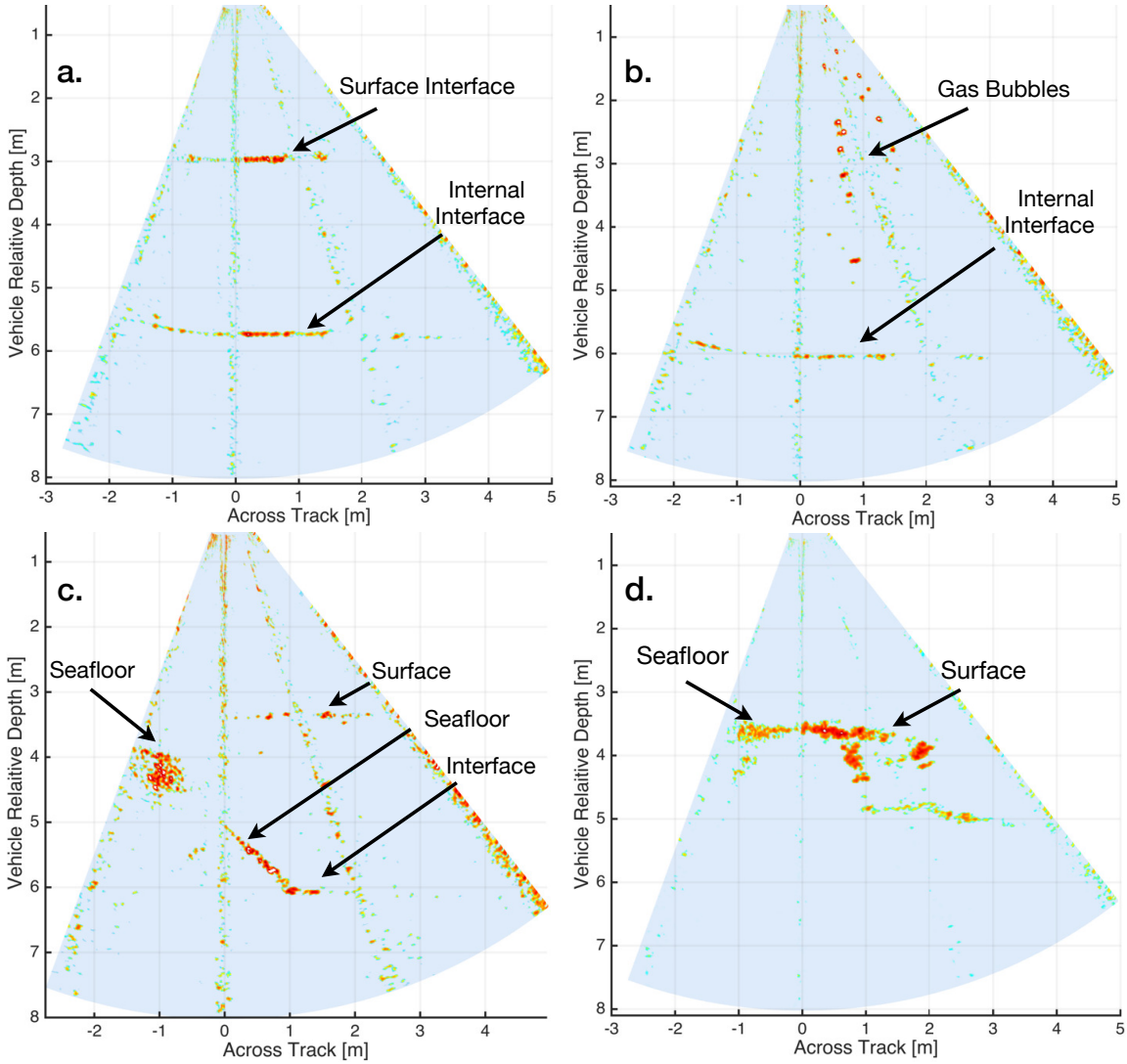

Figure 3.9: Examples of log intensity scale water column images from the 1350kHz multibeam sonar over the brine pool. (a) Acoustic returns from both the surface and internal interface. (b) Bubbles rising from within the brine pool. (c&d) The transition between the seafloor and the brine pool at the edge of the brine pool shows acoustic returns from the seafloor and brine surface interface.

3.4.2 Multibeam Sonar Results

Within the water column data collected while surveying the SJBP acoustic returns appeared consistently 3m and 6m below the sonar head (Figure 3.9a) and rising bubbles were observed (Figure 3.9b). As the survey was conducted 3m above the surface of the brine pool these returns are associated with the surface interface and an internal layer, which will be further discussed in conjunction with CTD analysis in Section 3.5. The transition from the seafloor to the steep edge of the brine pool and into the brine fluid is apparent in both Figures 3.9c & 3.9d.

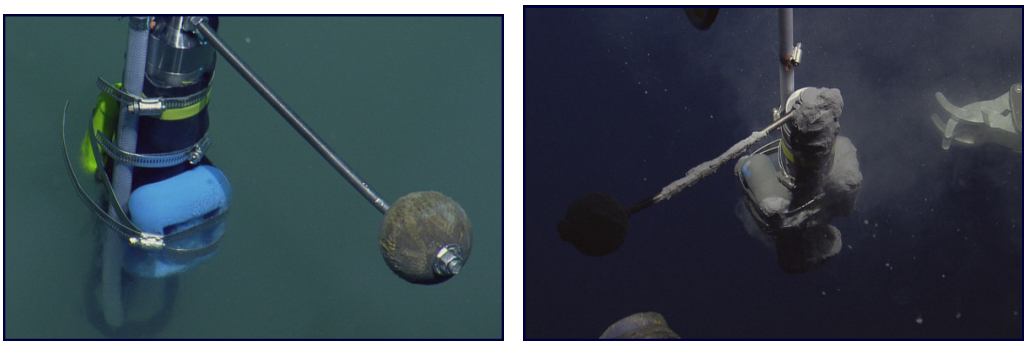

(a) (b)

Figure 3.10: Images of the CTD during brine pool sampling. (a) CTD partially submerged at the brine pool interface. (b) Fluidized mud, or suspended sediment, is present on the CTD following recovery.

3.4.3 Conductivity Temperature and Depth Measurements

The RBRconcerto CTD sensor described in Section 3.3.3 was lowered into the brine pool by spooling out the line from the ROV manipulator mounted reel. The brine pool surface interface was visually apparent as the CTD passed into the brine, Figure 3.10(a) and reel line depth makings allowed in-situ estimations of the sensor depth within the brine.

Seven casts ranging in depth, duration and location are indicated by orange dots, labeled Cx (where x is the cast number) in Figure 3.11. A hard bottom of the brine pool was not definitively reached using the 25m of hose available. Submerging the CTD more than 3m below the surface interface stirred up suspended sediment and upon recovery the sensor was covered with fine mud, indicating an internal layer, Figure 3.10(b).

Results from the CTD casts are outlined in Table 1. The data can be separated into three distinct horizontal layers; the ambient seawater, the upper brine layer, and a lower brine layer comprised of fluidized mud or suspended sediment. The brine pool surface interface is at a depth of 1320.5m with ambient water above. The internal interface which separates the upper and lower brine layers is documented in multiple casts to be consistently 3m below the surface interface.

Example temperature and salinity data from cast C1 (Table 1) is shown in Figure 3.12. This cast occurred at the center of the brine pool, marked *C1* in Figure 3.11, and the CTD sampled the brine surface interface for 30 minutes before being lowered at a

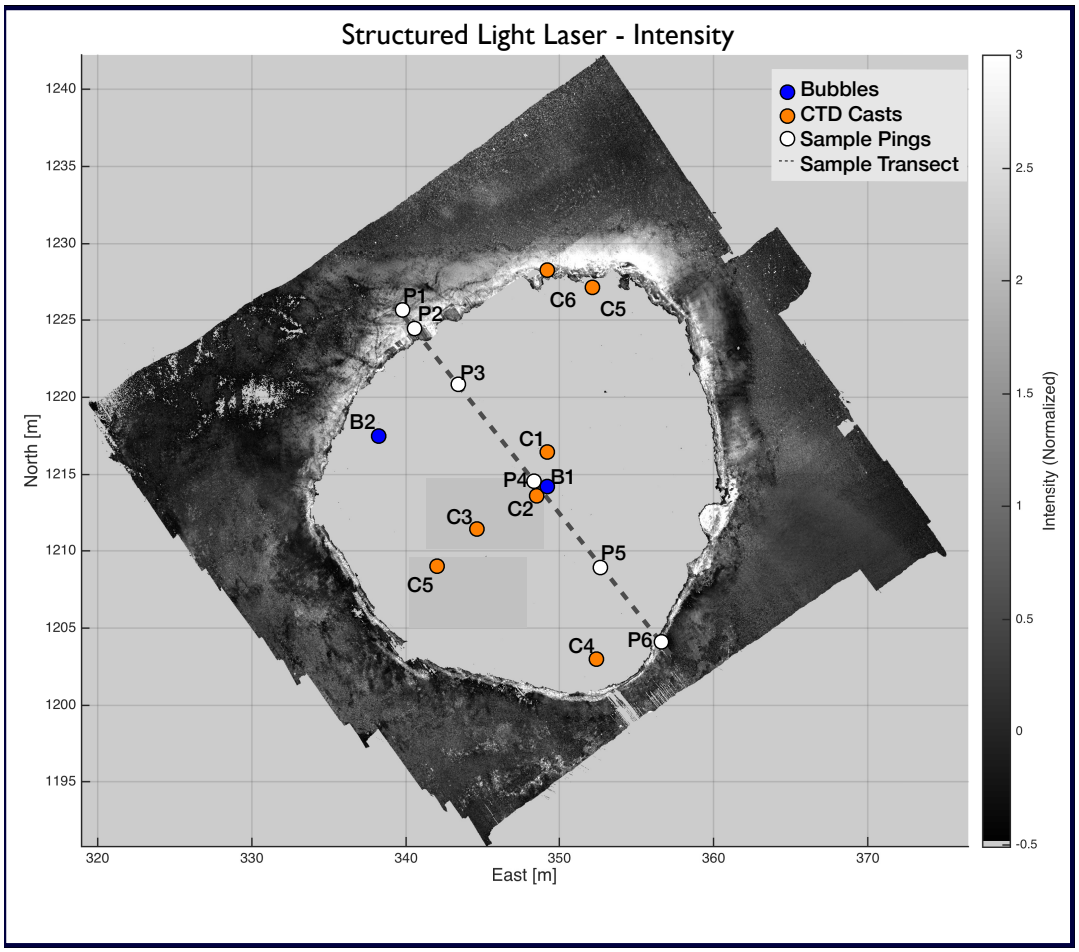

Figure 3.11: Structured light laser intensity (backscatter) map of the San Jac Brine Pool annotated with points of interest including including CTD cast locations *(Cx)*, detected bubbles *(Bx)* and a dashed line corresponding to the locations of the water column images within the conceptual cross section shown in Figure 3.13.

constant speed to approximately 17m and reeled back to the surface. Visual observations implying the sensor may have stopped descending were contradicted upon examining the CTD depth data which was linear with time. A hard substrate bottom to the brine pool was not found using the lowered sensor.

The three distinct layers are clear in both the temperature and salinity versus depth plots in Figure 3.12. This layering appeared consistent across the pool during multiple CTD casts, Table 1, and corresponds with the results from the multibeam water column images, Figure 3.9. The ambient seawater above the brine pool had a temperature of 4.5°C and a mean salinity of 40 PSU. The 3m upper brine layer existing between depths of 1320.5m and 1323.5m was consistently warmer by 3°C and significantly more saline with values ranging from 90-125 PSU. Below a depth of 1323.5m the layer containing suspended sediment showed a temperature increase to approximately 19°C but was less saline than the upper layer, with values in the range of 50-70 PSU. Additional analysis, sources of error, density computations and comparison to the multibeam images follows in Section 3.5.

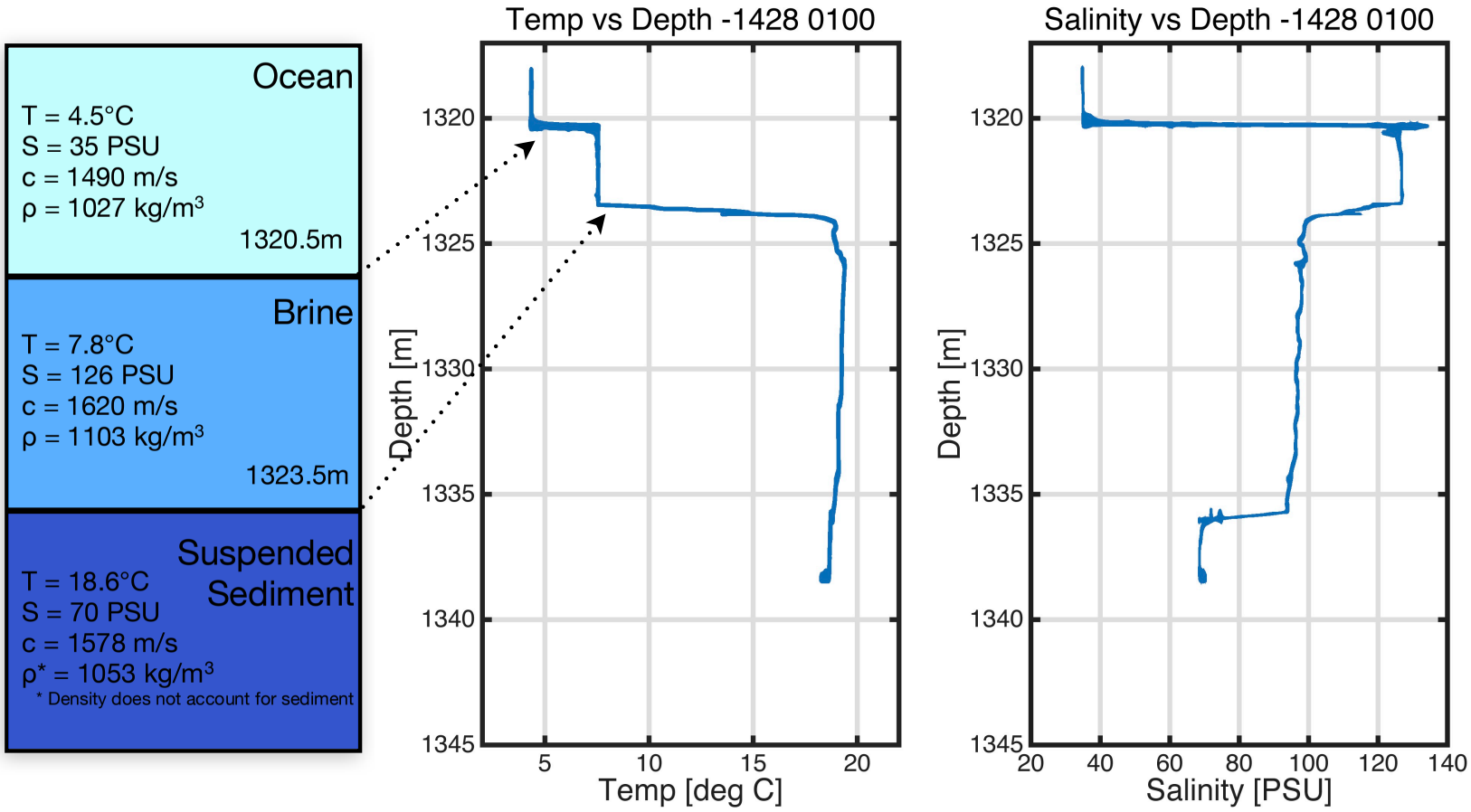

Figure 3.12: CTD results from cast *C1* located near the center of the San Jac Brine Pool, May 16, 2015 at 0100 GMT. The brine surface interface was sampled for 30 minutes before the sensor was lowered 17m at a constant speed over a peroid of 8 minutes. The surface interface, upper brine layer, internal density interface and lower layer consisting of suspended sediment are distinctly visible in both the temperature and salinity data. The diagram to the left provides corresponding temperature, salinity, sound speed and density values as computed by the RBR software.

3.5 Discussion

3.5.1 High Resolution Mapping

The remote systematic surveys completed at the San Jac Brine Pool provide a comprehensive spatial perspective which allow geological and biological analysis. For example, the 3m high crater wall is varied in structure as depicted by the mosaic and structured light laser intensity image. The contrast between the thin crater wall surrounding approximately two-thirds of the crater and the sloping northern side is apparent. The spatial extent and type of biological activity can also be quantified from the photomosaic as the 2-4 pixels per centimeter resolution makes it possible to distinguish and classify larger species such as mussels, squat lobsters and tube worms. Additionally, the tide pools are put in context within the larger brine pool and the delicate structures keeping them in place appear in detail. Based on the coloring of the surrounding seafloor, there appear to be two locations from which the brine flows over the crater wall. The first, larger area is along the northern edge which slopes to the seafloor. The second location is a much smaller waterfall like feature at the south eastern side which appears as a lack of data in the laser intensity image, Figure 3.11 and a lighter spot along the crater wall in the mosaic, Figure 3.8. The structured light intensity image, Figure 3.11, also indicates clear regions of altered seafloor due to brine and biological activity.

3.5.2 Analysis of Multibeam Water Column Data

Observed acoustic reflections within the brine pool crater correspond to seafloor substrate, bubbles and density interfaces as outlined in Section 3.4.2 and Figure 3.9. Multiple reflections within a single water column image correlate with the brine surface interface and an internal density layer. The intensity of these responses varied, with the return corresponding to the brine interface occasionally becoming weak or intermittent. While this may be an artifact of the multibeam sensor it is more likely due to varying surface density due to mixing, especially near the bubble plume.

The steady stream of bubbles rising from the center of the brine pool observed using the high definition ROV camera is marked *B1* in Figure 3.11. This bubble stream was likely detected in 2013 by the *E/V Nautilus's* EM302 shipboard multibeam system. Un-

Cast	Location	Time	Procedure	Seawater		Upper Brine Layer			Lower Brine Layer			Notes
				°C	PSU	Depth	°C	PSU	Depth	°C	PSU	
C1	Center of pool	May 16 0100UTC	30min at BP interface then continuous 20m, 8min cast	4.5	35	1320.5	7.8	126	1323.5	18.6	70	
C2	Center, near bubbles	May 18 1313UTC	Continuous 25m, 6min cast	4.5	35	1320.5	7.8	93	1323.5	19	65	
C3	East of center	May 17 2130UTC	7-30min samples, 0.5m increments	4.5	35	1320.5	7.8	127	1323.5	19	100	
C4	Southern edge	May 17 1000UTC	3-45min samples, 1m increments	4.5	43	1320.5	7.8	80	1323.5	N/A	N/A	
C5	10m SW of center	May 18 0230UTC	2-45min samples, 1.5m increments	4.4	45	1320.5	7.8	85	1323.5	N/A	N/A	
C6	Tide pools, North edge	May 18 0420UTC	1-45min measurement at interface	4.5	44	1320.4	4.4	64	N/A	N/A	N/A	Outside main pool
C7	North Edge of BP	May 18 0655UTC	1- 60min sample at interface	4.4	45	1320.5	6	80	N/A	N/A	N/A	ROV drift
Mean	—	—	—	4.5	40	1320.5	7.8	98.5	1323.5	18.9	78	Pool samples only

Table 3.1: Conductivity temperature and depth (CTD) sensor results at seven locations within the San Jac Brine Pool. The duration and depth of each cast varied as outlined under procedure. Only three casts passed below the internal interface and one cast was conducted within the tide pool, outside the main brine pool. Cast locations are shown in Figure 3.11.

surprisingly, this stream of bubbles is also visible in the high resolution ROV mounted multibeam. Notably, bubbles are detected below the surface interface, within the upper brine layer. Stationary multibeam data collection combined with image processing techniques have successfully isolated and determined the rise rates of similar bubble streams [19]. Additionally, a second smaller bubble stream near the northwest edge of the pool, not observed with the ROV video cameras during operations on site appears in the water column data and is marked *B2* in Figure 3.11.

Modeling Internal Structure of the Brine Pool

Visualization of the internal brine pool structure using remote imaging data is a powerful tool for the geologic community. A conceptual brine pool cross section can be developed using adjacent water column images. Twenty-one across track multibeam water column images represented by the dashed line in Figure 3.11 have been evaluated for acoustic returns caused by internal interfaces, bubbles and the seafloor. Combining these data reveals a cross section of the brine pool, Figure 3.13. Small '+' marks along the bottom of figure indicate center of each water column image, which have an overlap of 30-50%. Example water column images are shown below the transect and are labeled *P1-P6*, which correspond to similarly labeled locations on the dashed line in Figure 3.11 and along the bottom of Figure 3.13. This representation depicts the structure of the brine pool including the seafloor (visible in the water column image labeled *P1* in Figure 3.13), crater wall (*P2* and *P6* in Figure 3.13), internal layering (*P3* and *P5* in Figure 3.13), and rising bubbles (*P4* in Figure 3.13). Furthermore, a solid line within the diagram at the surface interface indicates a distinct acoustic return, as seen in Figure 3.9a, while a dashed line corresponds to a weaker intermittent return, observed in *P5* in Figure 3.13.

This cross section depiction of the brine pool created with a transect of water column data illustrates the consistency of layering and places the bubble stream (labeled *B1*) in context. As previously noted, intermittent acoustic returns from the surface interface near the bubble stream are likely indicative of mixing associated with the disturbance

of rising bubbles. The multibeam does not penetrate the second interface therefore it is not possible to determine the structure of the crater below 1323.5m using this system. Discontinuity within sonar returns at the brine pool edge indicate steep crater walls also observed by the ROV's cameras in Figure 3.2(c) and within the mosaic, Figure 3.8, and laser intensity map Figure 3.11.

3.5.3 CTD and Multibeam associations

The reel mounted CTD proved to be a key component for confirming the density stratification observed within multibeam data. As noted by Figure 3.12 the density differential at the brine interface was significant enough to reflect acoustic signals which is explained by the significant increase in salinity within the upper 3m brine layer. Significant overshoot is noticeable in the salinity data as the sensor passes through the surface interface in Figure 3.12. Fluidized mud comprises the layer below the internal interface detected by the multibeam, verified by CTD and made evident upon recovery by the sediment covering the sensor. Due to the design of the inductive conductivity sensor, which requires fluid to flow across the sensor, salinity readings acquired within the fluidized mud may not be accurate. According to sensor data, despite an elevated temperature and decreased salinity readings the layer of fluidized mud is stable below a cooler, higher saline upper brine layer, Table 3.1. Conversely temperature data is consistent between casts and appears to stabilize. Regardless of absolute values, stratification was consistent at each CTD sampling point within the brine pool and matched the results from the multibeam.

3.5.4 Geologic Implications

The ability to detect internal structure and gas seep activity below the surface of a brine pool will allow for discrete sampling, including the collection of water samples at specific areas of activity which will maximize the use of sample space and time. Additionally, the consistency of layering and stratification within the brine pool can indicate stability or mixing potential. Sequential surveys, which are systematic and efficient can indicate temporal changes with regard to seep activity as well as density

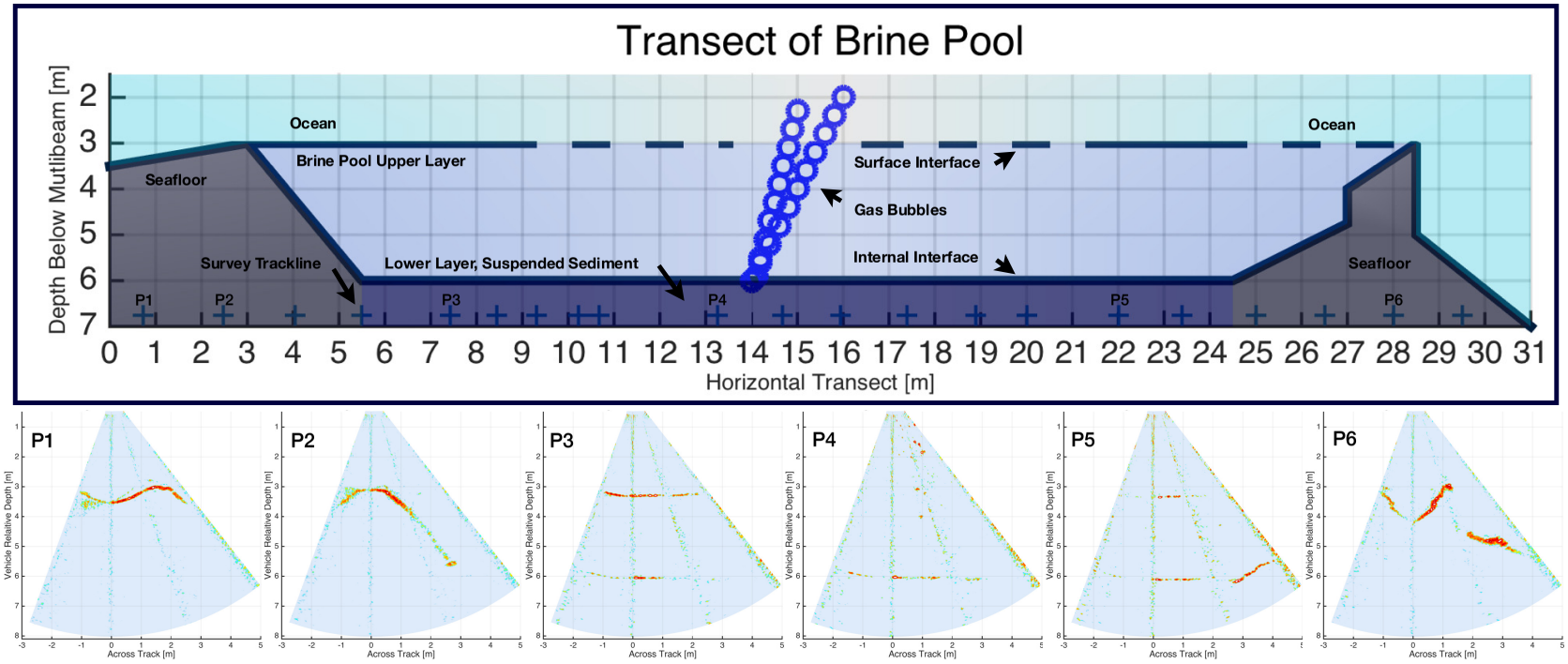

Figure 3.13: Twenty one across track water column images collected by the 1350kHz multibeam sonar are merged to create a conceptual cross section diagram of the brine pool. The center of each water column image (and survey trackline) is denoted by a '+' along the bottom of the diagram. Within the brine pool the location of these images is represented by the dashed line in Figure 3.11. Six selected example water column images depicting internal layering, bubbles and the crater wall are shown below the transect and are labeled *P1-P6* in this diagram and in Figure 3.11.

stability.

3.6 Conclusion

The high resolution 1350kHz multibeam sonar system has demonstrated the ability to detect density anamolies, stratification, and bubbles within a brine pool. Confirmation was provided by the reel mounted CTD sensor through multiple and varying sampling efforts. This capability has been observed at both the GC233 and San Jac Brine Pools within the Gulf of Mexico. Remote and systematic surveys allow for efficient creation of geo-referenced maps which improve sampling efforts and geologic understanding of brine pools.

List of References

[1] D. W. Caress, H. Thomas, W. J. Kirkwood, R. McEwen, R. Henthorn, D. A. Clague, C. K. Paull, and J. Paduan, "High-resolution multibeam, sidescan, and subbottom surveys using the mbari auv d. allan b." *Marine Habitat Mapping Technology for Alaska. Alaska Sea Grant College Program, University of Alaska, Fairbanks,*, pp. 47–69, 2008.

[2] V. Ferrini, M. Tivey, S. M. Carbotte, F. Martinez, and C. Roman, "Variable morphologic expression of volcanic, tectonic, and hydrothermal processes at six hydrothermal vent fields in the Lau back-arc basin," *Geochemistry Geophysics Geosystem*, July 2008.

[3] R. B. Wynn, V. A. I. Huvenne, T. P. Le Bas, B. J. Murton, D. P. Connelly, B. J. Bett, H. A. Ruhl, K. J. Morris, J. Peakall, D. R. Parsons, E. J. Sumner, S. E. Darby, R. M. Dorrell, and J. E. Hunt, "Autonomous underwater vehicles (auvs): Their past, present and future contributions to the advancement of marine geoscience," *Marine Geology*, vol. 352, pp. 451–468, 6 2014. [Online]. Available: http://www.sciencedirect.com/science/article/pii/S0025322714000747

[4] M. R. Hudec, M. P. A. Jackson, and F. J. Peel, "Influence of deep louann structure on the evolution of the northern gulf of mexico," *AAPG Bulletin*, vol. 97, no. 10, pp. 1711–1735, 2013. [Online]. Available: http://aapgbull.geoscienceworld.org/content/97/10/1711

[5] M. Hovland and A. Judd, *Seabed pockmarks and seepages: impact on geology, biology, and the marine environment*. Springer, 1988.

[6] R. K. Anderson, R. S. Scalan, P. L. Parker, and E. W. Behrens, "Seep oil and gas in Gulf of Mexico slope sediment," *Science*, vol. 222, no. 4624, pp. 619–621, 1983. [Online]. Available: http://science.sciencemag.org/content/222/4624/619

[7] J. M. Brooks, D. A. Wiesenburg, H. Roberts, R. S. Carney, I. R. MacDonald, C. R. Fisher, N. L. Guinasso, W. W. Sager, S. J. McDonald, R. A. Burke, P. Aharon, and T. J. Bright, "Salt, seeps and symbiosis in the Gulf of Mexico," *Eos, Transactions American Geophysical Union*, vol. 71, no. 45, pp. 1772–1773, 1990. [Online]. Available: http://dx.doi.org/10.1029/EO071i045p01772

[8] S. B. Joye, I. R. MacDonald, J. P. Montoya, and M. B. Peccini, "Geophysical and geochemical signatures of Gulf of Mexico seafloor brines," *Biogeosciences*, vol. 2, pp. 295–309, 2005.

[9] D. F. Williams and I. Lerche, "Salt domes, organic-rich source beds and reservoirs in the intraslope basins of the gulf coast region," in *Dynamical Geology of Salt and Related Structures*, I. Lerche and J. O'Brien, Eds. Academic Press, 1987, pp. 751 – 786. [Online]. Available: http://www.sciencedirect.com/science/article/pii/B9780124441705500245

[10] I. MacDonald, "Stability and change in Gulf of Mexico chemosynthetic communities. Volume II: Technical report. prepared by the Geochemical and Environmental

Research Group, Texas A&M University. U.S. Dept. of the Interior, Minerals Mgmt. Service, Gulf of Mexico OCS Region, New Orleans, LA," U.S. Department of the Interior Minerals Management Service, Tech. Rep., July 2002.

[11] T. W. Neurauter and W. R. Bryant, "Seismic expression of sedimentary volcanism on the continental slope, northern Gulf of Mexico," *Geo-Marine Letters*, vol. 10, no. 4, pp. 225–231, 1990. [Online]. Available: http://dx.doi.org/10.1007/BF02431069

[12] H. Roberts and R. Carney, "Evidence of episodic fluid, gas, and sediment venting on the northern Gulf of Mexico continental slope," *Economic Geology*, no. 92, pp. 863–978, 1997.

[13] I. R. MacDonald, J. F. R. II, J. Norman L. Guinasso, J. M. Brooks, R. S. Carney, W. A. Bryant, and T. J. Bright, "Chemosynthetic mussels at a brine-filled pockmark in the northern Gulf of Mexico," *Science*, vol. 248, no. 4959, pp. 1096–1099, June 1990.

[14] A. H. Bouma and W. R. Bryant, "Physiographic features on the northern Gulf of Mexico continental slope," *Geo-Marine Letters*, vol. 14, no. 4, pp. 252–263, 1994. [Online]. Available: http://dx.doi.org/10.1007/BF01274061

[15] R. Merewether, M. S. Olsson, and P. Lonsdale, "Acoustically detected hydrocarbon plumes rising from 2-km depths in guaymas basin, gulf of california," *Journal of Geophysical Research: Solid Earth*, vol. 90, no. B4, pp. 3075–3085, March 1985.

[16] E. E. Cordes, A. P. Michel, J. M. Petersen, S. D. Wankel, R. Ansorge, P. R. Girguis, N. Leisch, C. Smart, C. Roman, S. Wetzel, and C. Vidoudez, "Rov Hercules investigates brine lakes on the bottom of the ocean," *Oceanography*, vol. 29, no. 1, pp. 30–31, Supplement 2016.

[17] P. K. Trabant and B. J. Presley, *Orca Basin, anoxic depression on the continental slope, northwest Gulf of Mexico*, A. H. Bouma, G. T. Moore, and J. M. Coleman, Eds. AAPG, 1978, vol. Framework, facies, and oil-trapping characteristics of the upper continental margin: AAPG Studies in Geology 7.

[18] R. S. Pilcher and R. D. Blumstein, "Brine volume and salt dissolution rates in orca basin, northeast gulf of mexico," *AAPG Bulletin*, vol. 91, no. 6, pp. 823–833, 2007. [Online]. Available: http://aapgbull.geoscienceworld.org/content/91/6/823

[19] C. Roman, G. Inglis, J. I. Vaughn, C. Smart, B. Douillard, and S. Williams, "The development of high-resolution seafloor mapping techniques," *Oceanography*, vol. 25(1), no. supplement, 2012.

[20] G. Inglis, C. Smart, J. Vaughn, and C. Roman, "A pipeline for structured light bathymetric mapping," in *Intelligent Robots and Systems, Proceedings. October 7-12, IEEE/RSJ International Conference on*, 2012.

[21] C. J. Smart, C. Roman, and S. N. Carey, "Detection of diffuse seafloor venting using structured light imaging," *Geochemistry, Geophysics, Geosystems*, vol. 14, no. 11, pp. 4743–4757, 2013. [Online]. Available: http://dx.doi.org/10.1002/ggge.20280

[22] "New frontiers in ocean exploration: The e/v nautilus and noaa ship okeanos explorer 2015 field season," *Oceanography*, vol. 29, no. 1, p. 84, Supplement 2016.

[23] P. Anschutz, J. S. Turner, and G. Blanc, "The development of layering, fluxes through double-diffusive interfaces, and location of hydrothermal sources of brines in the Atlantis II Deep: Red Sea," *Journal of Geophysical Research: Oceans*, vol. 103, no. C12, pp. 27 809–27 819, 1998. [Online]. Available: http://dx.doi.org/10.1029/98JC02401

[24] S. A. Swift, A. S. Bower, and R. W. Schmitt, "Vertical, horizontal, and temporal changes in temperature in the Atlantis II and Discovery hot brine pools, Red Sea," *Deep Sea Research Part I: Oceanographic Research Papers*, vol. 64, pp. 118–128, 6 2012. [Online]. Available: http://www.sciencedirect.com/science/article/pii/S0967063712000568

[25] J. M. Woodside and A. V. Volgin, "Brine pools associated with Mediterranean Ridge mud diapirs: an interpretation of echo-free patches in deep tow sidescan sonar data," *Marine Geology*, vol. 132, no. 1–4, pp. 55 – 61, 1996, the Mediterranean Ridge Diapiric Belt. [Online]. Available: http://www.sciencedirect.com/science/article/pii/0025322795001530

[26] I. R. MacDonald and M. B. Peccini, "Distinct activity phases during the recent geologic history of a Gulf of Mexico mud volcano," *Marine and Petroleum Geology*, vol. 26, no. 9, pp. 1824–1830, 11 2009. [Online]. Available: http://www.sciencedirect.com/science/article/pii/S0264817208002110

[27] I. R. MacDonald, J. F. Reilly, J. S. Chu, and D. Olivier, "NR-1: Deep-ocean introduction of new laser line scanner," *Sea Technology*, vol. 38, no. 2, pp. 59–64, February 1997.

[28] S. D. Wankel, S. B. Joye, V. A. Samarkin, S. R. Shah, G. Friederich, J. Melas-Kyriazi, and P. R. Girguis, "New constraints on methane fluxes and rates of anaerobic methane oxidation in a Gulf of Mexico brine pool via in situ mass spectrometry,," *Deep Sea Research Part II: Topical Studies in Oceanography*, vol. 57, no. 21–23, pp. 2022–2029, November 2010. [Online]. Available: http://dx.doi.org/10.1016/j.dsr2.2010.05.009

[29] "Multibeam sonar theory of operation," L-3 Communications SeaBeam Instruments, Tech. Rep., 2000. [Online]. Available: https://www.ldeo.columbia.edu/res/pi/MB-System/sonarfunction/SeaBeamMultibeamTheoryOperation.pdf

[30] IOC, SCOR, and IAPSO, *The international thermodynamic equation of seawater – 2010: Calculation and use of thermodynamic properties* , manuals and guides 56 ed., Intergovernmental Oceanographic Commission, 2010.

[31] F. J. Millero and F. Huang, "The density of seawater as a function of salinity (5 to 70 g kg1) and temperature (273.15 to 363.15 k)," *Ocean Science*, vol. 5, pp. 91–100, 2009.

[32] O. Pizarro and H. Singh, "Toward large-area mosaicing for underwater scientific applications," *IEEE Journal of Oceanic Engineering*, vol. 28, no. 4, pp. 651–672, October 2003.

BIBLIOGRAPHY

"Multibeam sonar theory of operation," L-3 Communications SeaBeam Instruments, Tech. Rep., 2000. [Online]. Available: https://www.ldeo.columbia.edu/res/pi/MB-System/sonarfunction/SeaBeamMultibeamTheoryOperation.pdf

"New frontiers in ocean exploration: The e/v nautilus and noaa ship okeanos explorer 2015 field season," *Oceanography*, vol. 29, no. 1, p. 84, Supplement 2016.

Anderson, R. K., Scalan, R. S., Parker, P. L., and Behrens, E. W., "Seep oil and gas in Gulf of Mexico slope sediment," *Science*, vol. 222, no. 4624, pp. 619–621, 1983. [Online]. Available: http://science.sciencemag.org/content/222/4624/619

Anschutz, P., Turner, J. S., and Blanc, G., "The development of layering, fluxes through double-diffusive interfaces, and location of hydrothermal sources of brines in the Atlantis II Deep: Red Sea," *Journal of Geophysical Research: Oceans*, vol. 103, no. C12, pp. 27 809–27 819, 1998. [Online]. Available: http://dx.doi.org/10.1029/98JC02401

Bell, K. C., Nomikou, P., Carey, S., Stathopoulou, E., Polymenakou, P., Godelitsas, A., Roman, C., and Parks, M., "Continued exploration of the santorini volcanic field and cretan basin aegean sea," *Oceanography*, vol. 25(1), no. supplement, 2012.

Boser, B. E., Guyon, I. M., and Vapnik, V. N., "A training algorithm for optimal margin classifiers," in *Proceedings of the Fifth Annual Workshop on Computational Learning Theory*, ser. COLT '92. New York, NY, USA: ACM, 1992, pp. 144–152. [Online]. Available: http://doi.acm.org/10.1145/130385.130401

Bouguet, J.-Y., "Camera calibration toolbox for matlab," retrieved March 2008. [Online]. Available: http://www.vision.caltech.edu/bouguetj/calib_doc/

Bouma, A. H. and Bryant, W. R., "Physiographic features on the northern Gulf of Mexico continental slope," *Geo-Marine Letters*, vol. 14, no. 4, pp. 252–263, 1994. [Online]. Available: http://dx.doi.org/10.1007/BF01274061

Brooks, J. M., Wiesenburg, D. A., Roberts, H., Carney, R. S., MacDonald, I. R., Fisher, C. R., Guinasso, N. L., Sager, W. W., McDonald, S. J., Burke, R. A., Aharon, P., and Bright, T. J., "Salt, seeps and symbiosis in the Gulf of Mexico," *Eos, Transactions American Geophysical Union*, vol. 71, no. 45, pp. 1772–1773, 1990. [Online]. Available: http://dx.doi.org/10.1029/EO071i045p01772

Bruno, F., Bianco, G., Muzzupappa, M., Barone, S., and Razionale, A., "Experimentation of structured light and stereo vision for underwater 3D reconstruction," *ISPRS Journal of Photogrammetry and Remote Sensing*, vol. 66, no. 4, pp. 508 – 518, 2011.

Caress, D. W., Thomas, H., Kirkwood, W. J., McEwen, R., Henthorn, R., Clague, D. A., Paull, C. K., and Paduan, J., "High-resolution multibeam, sidescan, and subbottom surveys using the mbari auv d. allan b." *Marine Habitat Mapping Technology for*

Alaska. Alaska Sea Grant College Program, University of Alaska, Fairbanks,, pp. 47–69, 2008.

Carey, S. N., Bell, K. L. C., Rosi, M., Marani, M., Nomikou, P., Walker, S. L., Faure, K., and Kelly, J., "Submarine volcanoes of the aeolian arc, tyrrhenian sea," *Oceanography*, vol. 25(1), no. supplement, 2012.

Carey, S., Ballard, R., Bell, K. L., Bell, R. J., Connally, P., Dondin, F., Fuller, S., Gobin, J., Miloslavich, P., Phillips, B., Roman, C., Seibel, B., Siu, N., and Smart, C., "Cold seeps associated with a submarine debris avalanche deposit at kick'em jenny volcano, grenada (lesser antilles)," *Deep Sea Research Part I: Oceanographic Research Papers*, vol. 93, pp. 156–160, November 2014.

Connelly, D. P., Copley, J. T., Murton, B. J., Stansfield, K., Tyler, P. A., German, C. R., Van Dover, C. L., Amon, D., Furlong, M., Grindlay, N., Hayman, N., Huhnerbach, V., Judge, M., Le Bas, T., McPhail, S., Meier, A., Nakamura, K.-i., Nye, V., Pebody, M., Pedersen, R. B., Plouviez, S., Sands, C., Searle, R. C., Stevenson, P., Taws, S., and Wilcox, S., "Hydrothermal vent fields and chemosynthetic biota on the world's deepest seafloor spreading centre," *Nat Commun*, vol. 3, p. 620, 01 2012. [Online]. Available: http://dx.doi.org/10.1038/ncomms1636

Cordes, E. E., Michel, A. P., Petersen, J. M., Wankel, S. D., Ansorge, R., Girguis, P. R., Leisch, N., Smart, C., Roman, C., Wetzel, S., and Vidoudez, C., "Rov Hercules investigates brine lakes on the bottom of the ocean," *Oceanography*, vol. 29, no. 1, pp. 30–31, Supplement 2016.

Corliss, J. B., Dymond, J., Gordon, L. I., Edmond, J. M., von Herzen, R. P., Ballard, R. D., Green, K., Williams, D., Bainbridge, A., Crane, K., and van Andel, T. H., "Submarine thermal springs on the galapagos rift," *Science*, vol. 203, pp. 1073–1083, 1979.

Dalziel, S. B., Hughes, G. O., and Sutherland, B. R., "Whole-field density measurements by 'synthetic schlieren'," *Experiments in Fluids*, vol. 28, pp. 322–335, 2000.

Ferrini, V., Tivey, M., Carbotte, S. M., Martinez, F., and Roman, C., "Variable morphologic expression of volcanic, tectonic, and hydrothermal processes at six hydrothermal vent fields in the Lau back-arc basin," *Geochemistry Geophysics Geosystem*, July 2008.

German, C. R., Yoerger, D. R., Jakuba, M., Shank, T. M., Langmuir, C. H., and Nakamura, K., "Hydrothermal exploration with the autonomous benthic explorer," *Deep-Sea Research Part I: Oceanographic Research Papers*, vol. 55, no. 2, pp. 203–219, 2008.

Hannington, M. D., de Ronde, C. D. J., and Petersen, S., "Sea-floor tectonics and submarine hydrothermal systems," *Economic Geology*, vol. 100th Anniversary, pp. 111–141, 2005.

Hovland, M. and Judd, A., *Seabed pockmarks and seepages: impact on geology, biology, and the marine environment.* Springer, 1988.

Hudec, M. R., Jackson, M. P. A., and Peel, F. J., "Influence of deep louann structure on the evolution of the northern gulf of mexico," *AAPG Bulletin*, vol. 97, no. 10, pp. 1711–1735, 2013. [Online]. Available: http://aapgbull.geoscienceworld.org/content/97/10/1711

I. Thormahlen, J. Straub, U. G., "Refractive index of water and its dependence on wavelength, temperature and density," *Journal of Physical Chemistry*, vol. 14, pp. 933–945, 1985.

Inglis, G., Smart, C., Vaughn, J., and Roman, C., "A pipeline for structured light bathymetric mapping," in *Intelligent Robots and Systems, Proceedings. October 7-12, IEEE/RSJ International Conference on*, 2012.

IOC, SCOR, and IAPSO, *The international thermodynamic equation of seawater – 2010: Calculation and use of thermodynamic properties* , manuals and guides 56 ed., Intergovernmental Oceanographic Commission, 2010.

Jackson, D. R. and Dworski, J. G., "An acoustic backscatter thermometer for remotely mapping seafloor water temperature," *Journal of Geophysical Research: Oceans*, vol. 97(C1), pp. 761–767, 1992.

JAMSTEC, "R/v yokosuka & dsv shinkai 6500 cruise report yk13-05: Geochemical, geomicrobiological and biogeographical investigation of deep-sea hydrothermal activities in the mid cayman ridge, the caribbean," Japan Agency for Marine-Earth Science and Technology (JAMSTEC)," Cruise Report, 2013.

Joye, S. B., MacDonald, I. R., Montoya, J. P., and Peccini, M. B., "Geophysical and geochemical signatures of Gulf of Mexico seafloor brines," *Biogeosciences*, vol. 2, pp. 295–309, 2005.

Kinsey, J. C. and Whitcomb, L. L., "Preliminary field experience with the dvlnav integrated navigation system for oceanographic submersibles," *Control Engineering Practice*, vol. 12, pp. 1541–1549, 2004.

Light, R., Miller, V., Rona, P., and Bemis, K. "Acoustic instrumentation for imaging and quantifying hydrothermal flow in the neptune canada regional cabled observatory at main endeavour field." PDF. 2012. [Online]. Available: http://www.apl.washington.edu/project/projects/covis/pdfs/COVIS_concept_operation.pdf

Luzum, B., Starek, M., and Slatton., K. C., "Normalizing alsm intensities," Geosensing Engineering and Mapping (GEM) Civil and Coastal Engineering Department, University of Florida, USA., GEM Center Report No. Rep 2004-07-001., 2004.

MacDonald, I. R., II, J. F. R., Norman L. Guinasso, J., Brooks, J. M., Carney, R. S., Bryant, W. A., and Bright, T. J., "Chemosynthetic mussels at a brine-filled pockmark in the northern Gulf of Mexico," *Science*, vol. 248, no. 4959, pp. 1096–1099, June 1990.

MacDonald, I. R. and Peccini, M. B., "Distinct activity phases during the recent geologic history of a Gulf of Mexico mud volcano," *Marine and*

Petroleum Geology, vol. 26, no. 9, pp. 1824–1830, 11 2009. [Online]. Available: http://www.sciencedirect.com/science/article/pii/S0264817208002110

MacDonald, I. R., Reilly, J. F., Chu, J. S., and Olivier, D., "NR-1: Deep-ocean introduction of new laser line scanner," *Sea Technology*, vol. 38, no. 2, pp. 59–64, February 1997.

MacDonald, I., "Stability and change in Gulf of Mexico chemosynthetic communities. Volume II: Technical report. prepared by the Geochemical and Environmental Research Group, Texas A&M University. U.S. Dept. of the Interior, Minerals Mgmt. Service, Gulf of Mexico OCS Region, New Orleans, LA," U.S. Department of the Interior Minerals Management Service, Tech. Rep., July 2002.

Merewether, R., Olsson, M. S., and Lonsdale, P., "Acoustically detected hydrocarbon plumes rising from 2-km depths in guaymas basin, gulf of california," *Journal of Geophysical Research: Solid Earth*, vol. 90, no. B4, pp. 3075–3085, March 1985.

Millard, R. C. and Seaver, G., "An index of refraction algorithm for seawater over temperature, pressure, salinity, density, and wavelength," *Deep-Sea Research Part A*, vol. 37, no. 12, pp. 1909–1926, December 1990.

Millero, F. J. and Huang, F., "The density of seawater as a function of salinity (5 to 70 g kg1) and temperature (273.15 to 363.15 k)," *Ocean Science*, vol. 5, pp. 91–100, 2009.

Mobley, C. D., *Light and Water Radiative Transfer in Natural Waters*. Academic Press, 1994.

Moore, K. D., Jaffe, J. S., and Ochoa, B. L., "Development of a new underwater bathymetric laser imaging system: L-Bath," *J. Atmos. Oceanic Technol.*, vol. 17, no. 8, pp. 1106–1117, 2000.

Moore, K. and Jaffe, J., "Time-evolution of high-resolution topographic measurements of the sea floor using a 3-d laser line scan mapping system," *Oceanic Engineering, IEEE Journal of*, vol. 27, no. 3, pp. 525 – 545, Jul 2002.

Neurauter, T. W. and Bryant, W. R., "Seismic expression of sedimentary volcanism on the continental slope, northern Gulf of Mexico," *Geo-Marine Letters*, vol. 10, no. 4, pp. 225–231, 1990. [Online]. Available: http://dx.doi.org/10.1007/BF02431069

Otsu, N., "A threshold selection method from gray-level histograms," *IEEE Transactions on Systems, Man, and Cybernetics*, vol. 9, no. 1, pp. 62–66, Jan 1979.

Pelayo, A. M., Stein, S., and Stein, C. A., "Estimation of oceanic hydrothermal heat flux from heat flow and depths of midocean ridge seismicity and magma chambers," *GRL*, vol. 21, no. 8, pp. 713–716, 1994.

Pilcher, R. S. and Blumstein, R. D., "Brine volume and salt dissolution rates in orca basin, northeast gulf of mexico," *AAPG Bulletin*, vol. 91, no. 6, pp. 823–833, 2007. [Online]. Available: http://aapgbull.geoscienceworld.org/content/91/6/823

Pizarro, O. and Singh, H., "Toward large-area mosaicing for underwater scientific applications," *IEEE Journal of Oceanic Engineering*, vol. 28, no. 4, pp. 651–672, October 2003.

Richard, H. and Raffel, M., "Principle and applications of the background oriented schlieren (bos) method," *Measurement Science and Technology*, vol. 12, pp. 1576–1585, 2001.

Roberts, H. and Carney, R., "Evidence of episodic fluid, gas, and sediment venting on the northern Gulf of Mexico continental slope," *Economic Geology*, no. 92, pp. 863–978, 1997.

Roman, C., Inglis, G., and Rutter, J., "Application of structured light imaging for high resolution mapping of underwater archaeological sites," in *IEEE Oceans, 2010. Proceedings on*, 2010.

Roman, C., Inglis, G., Vaughn, J. I., Smart, C., Douillard, B., and Williams, S., "The development of high-resolution seafloor mapping techniques," *Oceanography*, vol. 25(1), no. supplement, 2012.

Roman, C. and Singh, H., "A Self-Consistent bathymetric mapping algorithm," *Journal of Field Robotics*, vol. 24, no. 1-2, pp. 23–50, 2007.

Rona, P., "Sonar images hydrothermal vents in seafloor observatory," *EOS Transactions of the AGU*, vol. 92, no. 20, pp. 169–170, May 2011.

Rona, P., Jackson, D. R., Wen, T., Jones, C., Mitsuzawa, K., Bemis, K. G., and Dworski, J. G., "Acoustic mapping of diffuse flow at a seafloor hydrothermal site: Monolith vent, juan de fuca ridge," *GRL*, vol. 24, no. 19, pp. 2351–2354, 1997.

Scheirer, D. S., Shank, T. M., and Fornari, D. J., "Temperature variations at diffuse and focused flow hydrothermal vent sites along the northern east pacific rise," *Geochemistry Geophysics Geosystems (G3)*, vol. 7, no. 3, pp. 1525–2027, 2006.

Schultz, A., Delaney, J. R., and McDuff, R. E., "On the Partitioning of Heat Flux Between Diffuse and Point Source Seafloor Venting," *Journal of Geophysical Research*, vol. 97, no. B9, pp. 12 299–12 314, 1992.

Shank, T., Fornari, D., Yoerger, D., Humphris, S., and Bradley, A., "Deep Submergence Synergy: Alvin and ABE Explore the Galapagos Rift at 86 W," *EOS Transactions of the AGU*, vol. 84, no. 41, pp. 425–440, October 2003.

Singh, H., Weyer, F., Howland, J., Duester, A., Yoerger, D., and Bradley, A., "Quantitative stereo imaging from the autonomous benthic explorer (abe)," in *OCEANS '99 MTS/IEEE. Riding the Crest into the 21st Century*, vol. 1, 1999, pp. 52–57 vol.1.

Smart, C. J., Roman, C., and Carey, S. N., "Detection of diffuse seafloor venting using structured light imaging," *Geochemistry, Geophysics, Geosystems*, vol. 14, no. 11, pp. 4743–4757, 2013. [Online]. Available: http://dx.doi.org/10.1002/ggge.20280

Smith, R. C. and Baker, K. S., "Optical properties of the clearest natural waters (200–800 nm)," *Appl. Opt.*, vol. 20, no. 2, pp. 177–184, Jan 1981. [Online]. Available: http://ao.osa.org/abstract.cfm?URI=ao-20-2-177

Swift, S. A., Bower, A. S., and Schmitt, R. W., "Vertical, horizontal, and temporal changes in temperature in the Atlantis II and Discovery hot brine pools, Red Sea," *Deep Sea Research Part I: Oceanographic Research Papers*, vol. 64, pp. 118–128, 6 2012. [Online]. Available: http://www.sciencedirect.com/science/article/pii/S0967063712000568

Tetlow, S. and Spours, J., "Three-dimensional measurement of underwater work sites using structured laser light," *Measurement Science and Technology*, vol. 10, no. 12, pp. 1162–1167, Dec. 1999.

Trabant, P. K. and Presley, B. J., *Orca Basin, anoxic depression on the continental slope, northwest Gulf of Mexico*, Bouma, A. H., Moore, G. T., and Coleman, J. M., Eds. AAPG, 1978, vol. Framework, facies, and oil-trapping characteristics of the upper continental margin: AAPG Studies in Geology 7.

Wankel, S. D., Joye, S. B., Samarkin, V. A., Shah, S. R., Friederich, G., Melas-Kyriazi, J., and Girguis, P. R., "New constraints on methane fluxes and rates of anaerobic methane oxidation in a Gulf of Mexico brine pool via in situ mass spectrometry,," *Deep Sea Research Part II: Topical Studies in Oceanography*, vol. 57, no. 21–23, pp. 2022–2029, November 2010. [Online]. Available: http://dx.doi.org/10.1016/j.dsr2.2010.05.009

Williams, D. F. and Lerche, I., "Salt domes, organic-rich source beds and reservoirs in the intraslope basins of the gulf coast region," in *Dynamical Geology of Salt and Related Structures*, Lerche, I. and O'Brien, J., Eds. Academic Press, 1987, pp. 751 – 786. [Online]. Available: http://www.sciencedirect.com/science/article/pii/B9780124441705500245

Woodside, J. M. and Volgin, A. V., "Brine pools associated with Mediterranean Ridge mud diapirs: an interpretation of echo-free patches in deep tow sidescan sonar data," *Marine Geology*, vol. 132, no. 1–4, pp. 55 – 61, 1996, the Mediterranean Ridge Diapiric Belt. [Online]. Available: http://www.sciencedirect.com/science/article/pii/0025322795001530

Wynn, R. B., Huvenne, V. A. I., Le Bas, T. P., Murton, B. J., Connelly, D. P., Bett, B. J., Ruhl, H. A., Morris, K. J., Peakall, J., Parsons, D. R., Sumner, E. J., Darby, S. E., Dorrell, R. M., and Hunt, J. E., "Autonomous underwater vehicles (auvs): Their past, present and future contributions to the advancement of marine geoscience," *Marine Geology*, vol. 352, pp. 451–468, 6 2014. [Online]. Available: http://www.sciencedirect.com/science/article/pii/S0025322714000747

Yoerger, D. R., Bradley, A. M., Jakuba, M. V., German, C. R., Shank, T. M., and Tivey, M. A., "Autonomous and remotely operated vehicle technology for hydrothermal vent discovery, exploration, and sampling," *Oceanography*, vol. 20, no. 1, pp. 152–161, 2007.